Reg Files

NUREG/CR-5530
ORNL/TM-11476

Analysis of H. B. Robinson PWR Vessel Fluence for Cycle 10 Utilizing Partial Length Shield Assemblies

50-261

Prepared by M. L. Williams, R. L. Childs, M. Asgari

Oak Ridge National Laboratory

Prepared for
U.S. Nuclear Regulatory Commission

AVAILABILITY NOTICE

Availability of Reference Materials Cited in NRC Publications

Most documents cited in NRC publications will be available from one of the following sources:

1. The NRC Public Document Room, 2120 L Street, NW, Lower Level, Washington, DC 20555
2. The Superintendent of Documents, U.S. Government Printing Office, P.O. Box 37082, Washington, DC 20013-7082
3. The National Technical Information Service, Springfield, VA 22161

Although the listing that follows represents the majority of documents cited in NRC publications, it is not intended to be exhaustive.

Referenced documents available for inspection and copying for a fee from the NRC Public Document Room include NRC correspondence and internal NRC memoranda; NRC Office of Inspection and Enforcement bulletins, circulars, information notices, inspection and investigation notices; Licensee Event Reports; vendor reports and correspondence; Commission papers; and applicant and licensee documents and correspondence.

The following documents in the NUREG series are available for purchase from the GPO Sales Program: formal NRC staff and contractor reports, NRC-sponsored conference proceedings, and NRC booklets and brochures. Also available are Regulatory Guides, NRC regulations in the *Code of Federal Regulations*, and *Nuclear Regulatory Commission Issuances*.

Documents available from the National Technical Information Service include NUREG series reports and technical reports prepared by other federal agencies and reports prepared by the Atomic Energy Commission, forerunner agency to the Nuclear Regulatory Commission.

Documents available from public and special technical libraries include all open literature items, such as books, journal and periodical articles, and transactions. *Federal Register* notices, federal and state legislation, and congressional reports can usually be obtained from these libraries.

Documents such as theses, dissertations, foreign reports and translations, and non-NRC conference proceedings are available for purchase from the organization sponsoring the publication cited.

Single copies of NRC draft reports are available free, to the extent of supply, upon written request to the Office of Information Resources Management, Distribution Section, U.S. Nuclear Regulatory Commission, Washington, DC 20555.

Copies of industry codes and standards used in a substantive manner in the NRC regulatory process are maintained at the NRC Library, 7920 Norfolk Avenue, Bethesda, Maryland, and are available there for reference use by the public. Codes and standards are usually copyrighted and may be purchased from the originating organization or, if they are American National Standards, from the American National Standards Institute, 1430 Broadway, New York, NY 10018.

NUREG/CR-5530
ORNL/TM-11476
RL

Analysis of H. B. Robinson PWR Vessel Fluence for Cycle 10 Utilizing Partial Length Shield Assemblies

Manuscript Completed: September 1989
Date Published: September 1990

Prepared by
M. L. Williams,* R. L. Childs, M. Asgari*

Oak Ridge National Laboratory
Operated by Martin Marietta Energy Systems, Inc.

Oak Ridge National Laboratory
Oak Ridge, TN 37831

Prepared for
Division of Engineering
Office of Nuclear Regulatory Research
U.S. Nuclear Regulatory Commission
Washington, DC 20555
NRC FIN B0415
Under Contract No. DE-AC05-84OR21400

*Louisiana State University Nuclear Science Center

ABSTRACT

Neutron transport calculations have been performed to determine the pressure vessel fluence and cavity dosimeter responses for cycle 10 of the H. B. Robinson pressurized water reactor. This cycle was the first to utilize "partial length shield assemblies" within the core to reduce the fluence rate at the critical weld location in the vessel. This work is part of the ongoing surveillance of the Robinson plant to insure that the projected fluence rates are reliable.

The flux calculations utilize a "two-channel" synthesis approximation and recently processed iron cross sections based on a new evaluation for the inelastic data above 3 MeV. The methodology used to calculate this highly asymmetrical configuration is discussed in detail, and a comparison of the calculated and measured cavity-dosimetry results is presented. Discrepancies are observed in the computed and measured results for the ^{237}Np dosimeter, and possible explanations are discussed. Calculated absolute neutron flux spectra, as well as radial, azimuthal, and axial variations in the fast flux and dpa within the pressure vessel, are given.

The effect of a least-squares consolidation of the measured and calculated results is studied.

CONTENTS

LIST OF FIGURES

LIST OF FIGURES (continued)

LIST OF TABLES

LIST OF TABLES (continued)

ACKNOWLEDGMENTS

The authors wish to thank Patricia Cleveland and Brenda Taylor of the ORNL Computing and Telecommunications Division for their hard work in preparing this manuscript. We are also grateful to Sam Grant and Kermit Cantrell from Carolina Power and Light Company, to Parvin Lippincott of Westinghouse, and to Richard Maerker in the ORNL Engineering Physics and Mathematics Division for their reviews of the report and for their useful comments. Frank Kam of the ORNL Computing and Telecommunications Division was the Program Manager for the project and provided guidance and suggestions throughout the study.

This work was performed by the Louisiana State University Nuclear Science Center under a subcontract with Martin Marietta Energy Systems, Inc.

1. OVERVIEW OF H. B. ROBINSON VESSEL FLUENCE REDUCTION PROGRAM

1.1 PRESSURE VESSEL EMBRITTLEMENT STUDIES

The H. B. Robinson (HBR) reactor is located in South Carolina and is owned and operated by Carolina Power and Light (CP&L). In 1982, this reactor was identified by the U.S. Nuclear Regulatory Commission (NRC) as one of several reactors in the United States that required remedial action to reduce the neutron fluence received by the reactor pressure vessel (RPV) so that the degree of radiation embrittlement would not exceed regulatory limits during the reactor's operating lifetime. Of particular concern, were two steel weldments in the RPV whose composition (i.e., nickel and copper content) raised concern that the nil-ductility transition temperature would exceed the screening criterion established for pressurized-thermal shock. During the period 1983-1984, a plan was developed by CP&L and subcontractors to significantly reduce the RPV fluence at the critical weld locations, and thus maintain the transition temperature below the required limit.[1]

The flux reduction program consisted of two components. First, a low-leakage fuel management program was begun during cycle 9. Burned fuel assemblies loaded on the core periphery were estimated to reduce the high energy flux incident on the RPV by about a factor of two. However, because the flux at the weld locations would still be excessive, a second reduction technique was also developed.

The second flux reduction method used specially designed fuel elements called "partial length shield assemblies" (PLSAs) to further reduce the flux levels around the axial elevations of the critical welds. Three PLSAs were to be placed on each flat of the core to lower the peak flux, which occurred near 0°. In the PLSAs, the fuel pellets in the bottom portion of the element were replaced by stainless steel, which removed the peripheral neutron source near the bottom of the core and also provided some shielding to prevent neutrons born within the core interior from reaching the vessel. The PLSAs were estimated to reduce the flux of the lower weld by about a factor of four. Near the top of the PLSAs, the normal fuel pellets were replaced by natural UO_2, which reduces the flux at the upper weld to an acceptable level so that it does not become limiting. The PLSA elements were first introduced into the HBR core beginning with cycle 10 (1985) and will remain a standard procedure for the remainder of the operating lifetime.

The HBR RPV fluence has been closely monitored by CP&L and the NRC to assure compliance with the predicted behavior. Both transport calculations and dosimetry measurements have been performed by Westinghouse for cycles nine,[2] ten,[3] and eleven.[4] Oak Ridge National Laboratory (ORNL) has also

previously analyzed the HBR RPV fluence for cycle nine,[5] using the LEPRICON code system.[6]

In this study, the ORNL analysis of the HBR vessel fluence, continues and will focus on cycle 10, which was the first to employ the PLSAs. These results will contribute to the NRC's goal of obtaining independent verification of the fluence accumulation rate in the HBR Unit 2 plant.

2. DESCRIPTION OF REACTOR AND EXPERIMENT CONFIGURATION

2.1 REACTOR DESCRIPTION

A plan view of the HBR Unit 2 reactor core and vessel internals is shown in Fig. 2.1. The reactor is a three-loop, Westinghouse pressurized water reactor (PWR) design that was first placed in operation in 1971. The core is approximately 365.8 cm (12 ft) in height and consists of 157 fuel assemblies, each containing a 15 by 15 array of fuel pins. The 12 shaded assemblies (three in each quadrant) on the core flats in Fig. 2.1 correspond to the PLSA elements. In these assemblies, the bottom 106.68 cm (42 in.) of the fuel pins contain stainless steel Type 304 (SS 304), and the top 30.48 cm (12 in.) consist of natural uranium. The portion of the PLSA between these top and bottom sections consists of typical UO_2 pellets, which were fresh fuel at the beginning of cycle 10.

At full power, the reactor produces 2300 MW(t), corresponding to a nominal coolant temperature during normal operation of about 288°C. [Note that cycle 9 was run at a somewhat cooler temperature.] Table 2.1 gives the monthly average fractional power production during January 1985-January 1986, the time period corresponding to cycle 10.

The RPV in the HBR plant has an inner radius of 197.49 cm (77.0 in.) and is 24.155 cm (9.4 in.) thick, including a 5.56 mm (0.22 in.) stainless steel liner on the inner surface. It contains three pairs of inlet/outlet penetrations, which are oriented as indicated in Fig. 2.1. The RPV design in HBR is typical of most light water reactor (LWR) vessels: three base steel plates are welded together longitudinally to form circular "shells," which are then welded circumferentially to form the vessel itself. Figure 2.2 illustrates the azimuthal location of the RPV longitudinal welds, as well as the axial position of the circumferential welds, relative to the active core height. The radiation exposure of the circumferential welds connecting the lower and intermediate shells ("lower circumferential weld") and the intermediate and nozzle shells ("upper circumferential weld"), respectively, was a primary concern in assessing the long-term integrity of the HBR RPV. The PLSA elements (shown in Fig. 2.2) were introduced beginning with cycle 10 in order to reduce the peak fluence received by these welds, when analysisindicated that they would experience excessive radiation embrittlement before the plant reached its nominal operation lifetime.

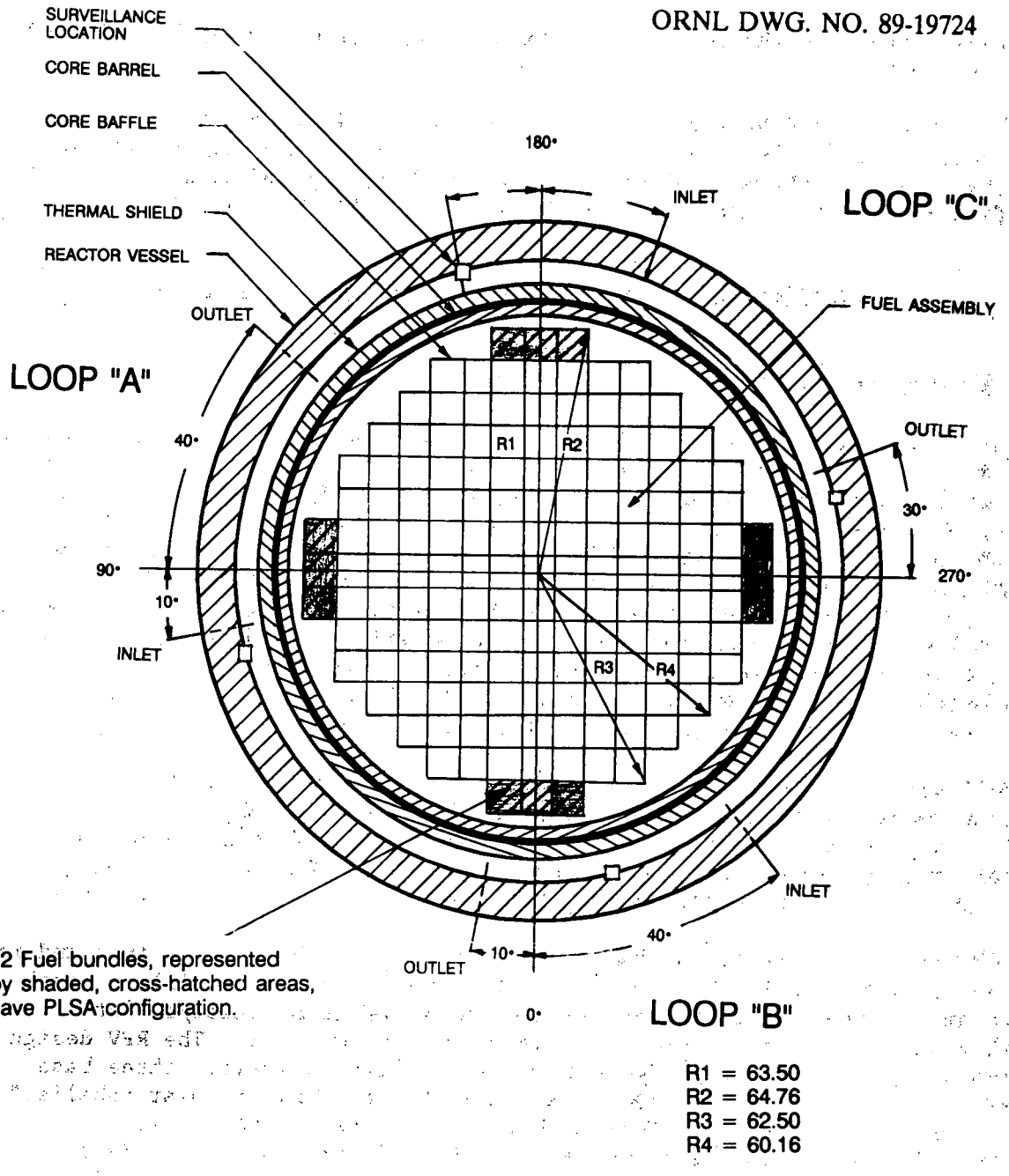

Fig. 2.1. Plan view of H. B. Robinson Unit 2.

ORNL DWG. NO. 89-15898

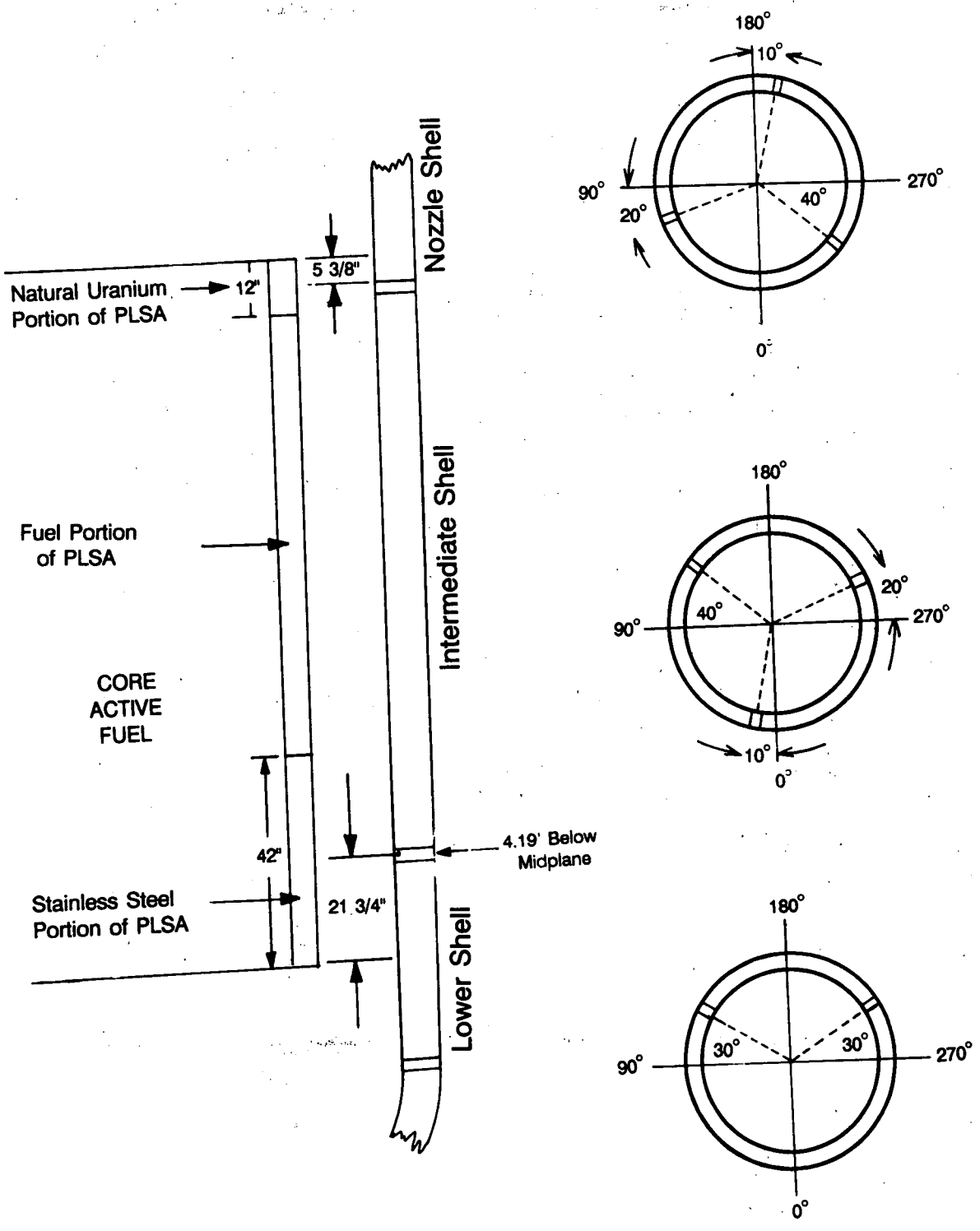

Fig. 2.2. Location of RPV welds.

Table 2.1. Monthly average power level of H. B. Robinson Unit 2 during cycle 10

Month	Operating time	Average power fraction[a]
January 1985	31	0.082
February 1985	28	0.516
March 1985	31	0.914
April 1985	30	0.945
May 1985	31	0.945
June 1985	30	0.988
July 1985	31	0.953
August 1985	31	0.908
September 1985	30	0.877
October 1985	31	0.897
November 1985	30	0.953
December 1985	31	0.954
January 1986	29	0.595

[a]Relative to 2300 MW(t).

Beyond the RPV is the reactor cavity region, lying between the vessel and the concrete reactor shield. The cavity in the HBR plant is relatively narrow, consisting of a 1.27 cm (0.5 in.) air gap, followed by a 7.62 cm (3 in.) insulation section, and another 8.179 cm (3.22 in.) air gap—totaling 17.069 cm (6.72 in.) between the vessel and the concrete shield. However, there are eight large "detector wells" approximately 33 cm wide by 80 cm deep that are inset in the concrete shield at 45° increments, result-ing in a much larger void region outside of the RPV than suggested by the reactor cavity width. The concrete walls surrounding the well indentions are lined with 6.35 mm of steel, and each well contains a 6.35-mm-thick steel cylinder with an outer radius of 9.5 cm. Following the suggestion in Reference 5, the concrete shield is assumed to be composed of ordinary Type 02-b concrete, with a reduced water content of 4.67 wt % and an iron rebar concentration of 0.7% by volume. There is a fair amount of uncertainty in the actual water content of the concrete because this value tends to decrease with time.

2.2 CAVITY DOSIMETER DESCRIPTION

A cavity dosimetry surveillance program was begun at the HBR Unit 2 plant in 1982. The first cavity dosimetry was installed at the beginning of cycle 9 as a cooperative venture between CP&L and the NRC as part of the LWR Pressure Vessel Surveillance Dosimetry Improvement Program to verify the accuracy of cavity measurements in establishing the magnitude of RPV fluence. After insertion of the PLSA elements in the core during the following cycle, the cavity dosimetry program was continued and further emphasized to (a) verify the predicted flux reduction because of PLSA elements, and (b) provide a more frequent monitoring of the vessel fluence than could be obtained from the limited number of in-vessel surveillance capsules. Westinghouse has performed the experimental cavity dosimetry analysis for cycles 9 through 11, and their measured results for cycle 10 are utilized in this study.[3]

The cavity dosimetry for cycle 10 consisted of six multiple foil packets and four stainless steel gradient wires. The gradient wires were all located at a radial distance of 238.02 cm (93.0 in.) from the core center, and were placed azimuthally at 267°, 279°, 297°, and 225°, respectively. Since the core exhibits 45° symmetry, these angular positions will correspond to 3°, 9°, 27°, and 45° in the primary octant. The wires at the first three of these locations each contained two foil packets, at elevations of +271.88 cm (106.0 in.) and -25.30 cm (-10.0 in.) from the core midplane, respectively. The packets at the higher elevation are actually positioned nearly 90 cm (35.0 in.) above the active core height, and were not analyzed in this study. Figures 2.3 and 2.4 show the locations of the cavity dosimeters for cycle 10.

The dosimeter packets consisted of an aluminum capsule that contained bare iron foils (~115 mg) and solid state track recorders (SSTRs) for ^{238}U, ^{237}Np, ^{235}U, and ^{239}Pu. Both bare and cadmium-covered SSTRs were utilized for ^{235}U and ^{239}Pu. A thin coverplate retains the dosimeters within two compartments drilled in the capsule. The holder capsule has a mass of about 60 g of aluminum and is assumed to have a negligible effect on the flux at the dosimeter locations.

In addition to the dosimeter packet results, the activation of the gradient wire itself also provides dosimetry results based on reactions in the iron, nickel, and cobalt isotopes present in the steel. The activity was determined by cutting the wire into 30 cm (1 ft) segments and tabulating the measured activity at the axial location corresponding to the center of each segment.

Table 2.2 summarizes the dosimeter reactions available for the HBR cycle 10 analysis and lists the source of the measured results. Each dosimeter was irradiated according to the power-time history given in Table 2.1. After removal from the reaction in January 1986, there was a 174-day decay time before the dosimeter activation products were counted. More details concerning the cycle 10 experimental program can be found in References 3 and 4.

ORNL DWG. NO. 89-19725

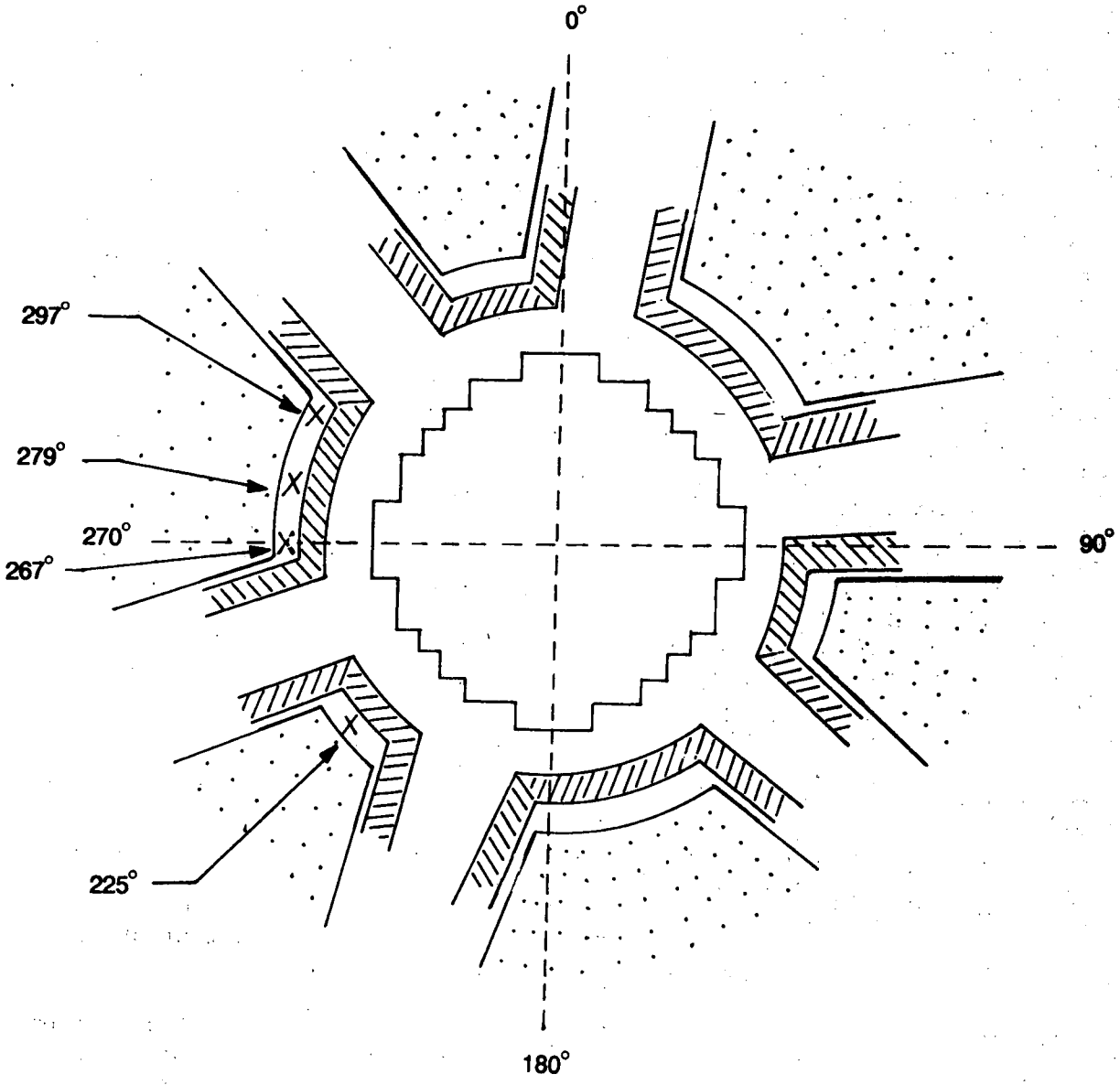

Fig. 2.3. Plan view of cavity dosimetry positions.

ORNL DWG. NO. 89-19726

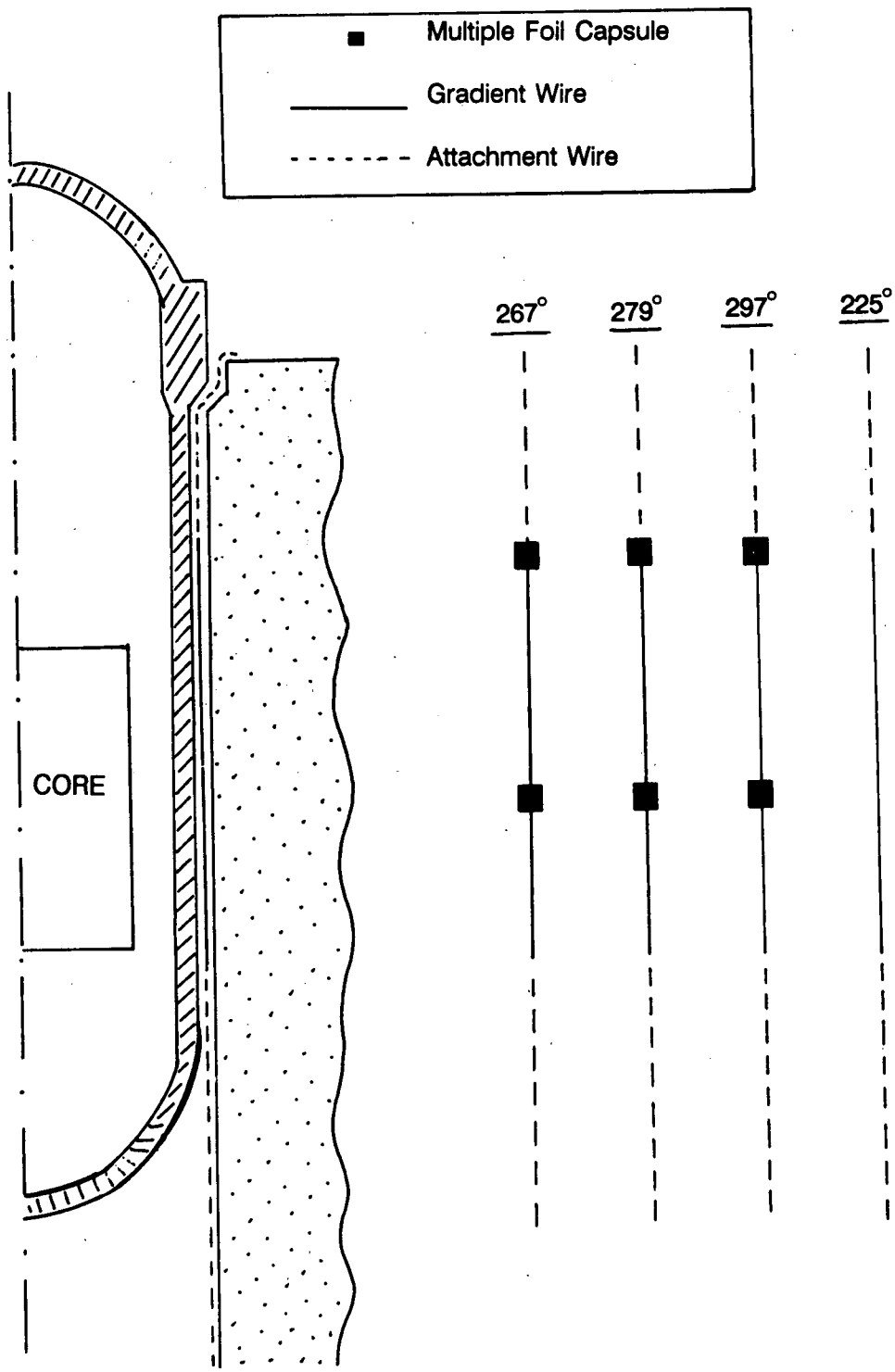

Fig. 2.4. Elevation view of cavity dosimetry.

Table 2.2. H. B. Robinson Unit 2 cycle 10 cavity dosimeter measurements

Dosimeter reaction	Approximate response range (MeV)	Source of measured data
$^{54}Fe(n,p)^{54}Mn$	>2.3	Foil in lower dosimeter packets
$^{54}Fe(n,p)^{54}Mn$	>2.3	Gradient wire
$^{58}Ni(n,p)^{58}Co$	>2.1	Gradient wire
$^{238}U(n,f)$	>1.5	SSTR in lower dosimeter packets
$^{237}Np(n,f)$	>0.2	SSTR in lower dosimeter packets
$^{59}Co(n,\gamma)^{60}Co$	<0.015	Gradient wire
$^{235}U(n,f)$ [bare]	<0.002	SSTR in lower dosimeter packets
$^{235}U(n,f)$ [Cd-cover]	$>5.5 \times 10^{-7}$	SSTR in lower dosimeter packets
$^{239}Pu(n,f)$ [bare]	$<5.0 \times 10^{-4}$	Not used[a]
$^{239}Pu(n,f)$ [Cd-cover]	$>5.5 \times 10^{-7}$	Not used[a]

[a]The measured plutonium results are inconsistent and not considered reliable.

3. TRANSPORT CALCULATION METHODOLOGY

3.1 FLUX SYNTHESIS METHODOLOGY

The flux distribution within the RPV varies in all three coordinate dimensions because of the three-dimensional (3-D) nature of the source and the irregular geometry of the HBR core. A 3-D cylindrical coordinate system (RθZ) has been used to represent the reactor configuration. Unfortunately, a 3-D transport calculation was not considered to be practical for a problem of this size and complexity; therefore, a 3-D flux synthesis technique, based on combining results from lower dimensional transport calculations, has been utilized in the analysis.

The synthesis method has been extensively used and verified in numerous RPV fluence calculations and has become the standard method for representing the 3-D flux distribution in pressure vessel studies.[7,8] However, a variation of the standard procedure is required here to account for the presence of the PLSA elements, which introduce a significant asymmetry in the axial and azimuthal distribution of the flux incident on the vessel. Whereas a "single channel" synthesis approximation will suffice for most reactor analysis, a "multi-channel" (e.g., two-channel) approximation must be used for the HBR cycle 10 calculations to account for the significantly different azimuthal distributions of the flux at elevations corresponding to the shield and fuel portions of the PLSA, respectively. A two-channel synthesis approximation was first applied to RPV fluence calculations in the earlier HBR analysis that supported the initial design of the PLSA assemblies and projected their effectiveness for fluence reduction. The accuracy of the two-channel synthesis methodology was recently validated by Maerker in the VENUS-3 benchmark experiment,[9] and it has also been employed by Westinghouse in their calculations of the HBR cycle 10 and cycle 11 dosimetry experiments.

The two-channel synthesis expression is given by the following:

$$\phi(R,\theta,Z) = \phi^{U}_{R\theta}(R,\theta)\,\frac{\phi^{U}_{RZ}(R,Z)}{\phi^{U}_{R}(R)} + \phi^{L}_{R\theta}(R,\theta)\,\frac{\phi^{L}_{RZ}(R,Z)}{\phi^{L}_{R}(R)}, \qquad (3.1)$$

where

$\phi^{U}_{R\theta}(R,\theta)$ and $\phi^{L}_{R\theta}(R,\theta)$ = upper and lower Rθ channel fluxes, respectively;

$\phi^{U}_{RZ}(R,Z)$ and $\phi^{L}_{RZ}(R,Z)$ = upper and lower RZ channel fluxes, respectively; and

$\phi^{U}_{R}(R)$ and $\phi^{L}_{R}(R)$ = upper and lower R channel fluxes, respectively.

The upper RΘ channel flux is obtained from a two-dimensional RΘ transport calculation in which the input RΘ source is computed by integrating the 3-D (i.e., RΘZ) core-source distribution axially over the fuel region above the shield portion of the PLSA. This axial interval (i.e., from 76.2 cm (30.0 in.) below the core midplane to the top of the core) will be designated the "upper core" region. Similarly, the RΘ source for the calculation of the lower RΘ channel fluxes is obtained by integrating the 3-D source over the axial region containing the shield portion of the PLSA. This region (i.e., from 76.2 cm below the midplane to the bottom of the core) is designated as the lower core. The two RΘ sources are significantly different near the PLSA elements (i.e., these elements contain a source in the upper region, but no source in the lower), which causes the two respective RΘ channel fluxes to have completely different azimuthal shapes.

The upper RZ channel flux is obtained from a two-dimensional RZ transport calculation in which the input RZ source is approximated by taking the 3-D source along the $\Theta = 0°$ and setting the portion of the source contained in the lower core equal to zero. The lower RZ channel source is also obtained from the $\Theta = 0°$ source distribution, except in this case, the portion of the source in the upper core region is zeroed out. The R channel fluxes are obtained from one-dimensional radial transport calculations in which the respective upper and lower RZ channel sources are integrated over the axial dimension. The ratios of the RZ to the R channel fluxes for the upper and lower regions, respectively, essentially provide the relative weighting of the two different azimuthal shapes represented by the two RΘ channel fluxes. Of course the RZ geometry must assume azimuthal symmetry, and this causes some error to be introduced in the synthesized fluxes, especially for the lower region where shielding material is present in the peripheral assemblies on the flats but not in the elements at other azimuthal positions. The shield material is included in the outer core region of the lower RZ model (since the 0° azimuth was the basis of the model) – this will cause the lower region contribution to the synthesized flux to be under-weighted at azimuths away from the flats. Unfortunately there is no easy method to overcome this shortcoming, other than using a still higher order synthesis approximation, which becomes exceedingly complex.

It is interesting to note that the two-channel synthesis approximation can be viewed as a straightforward superposition of two single channel synthesis calculations. In Eq. (3.1), the two terms on the right-hand side can be defined by

$$\phi^U(R,\Theta,Z) = \frac{\phi^U_{R\Theta}\ \phi^U_{RZ}}{\phi^U_R} \ , \qquad (3.2)$$

$$\phi^L(R,\theta,Z) = \frac{\phi^L_{R\theta}\ \phi^L_{RZ}}{\phi^L_R} \quad . \tag{3.3}$$

The function $\phi^U(R,\theta,Z)$ is just the single channel synthesis approximation for the 3-D flux distribution throughout the system using only the source in the upper portion of the core; and $\phi^L(R,\theta,Z)$ is the synthesized flux throughout the system using only the source in the lower portion of the core. The total flux distribution is the superposition of the two cases:

$$\phi(R,\theta,Z) = \phi^U(R,\theta,Z) + \phi^L(R,\theta,Z) \tag{3.4}$$

Because of the larger magnitude of the upper source, it is anticipated that ϕ^U will be much larger than ϕ^L throughout much of the system, except near the bottom of the core where the shield portion of the PLSA elements have an influence.

3.2 DISCRETE ORDINATES CALCULATIONS

The channel fluxes were computed with the DOT 4.3 discrete ordinates transport code, which required two Rθ, RZ, and R runs, respectively. An S_8 angular quadrature and a P_3 scatter cross-section expansion were used in the calculations, and the energy variation was represented by 47 neutron and 20 gamma groups. Figure 3.1 shows the DOT Rθ model used to compute the upper and lower Rθ channel fluxes.

A one-eighth segment of the core is modeled with reflected boundaries at $\theta = 0°$ and 45°. The DOT Rθ model used in this analysis is identical to that developed in Reference 5 for the cycle 9 calculations, except that the cavity detector well at 45° has been added. The only difference in the geometric models used for the upper and lower Rθ calculations is that the one and one-half assemblies appearing on the core flat contain fuel material for the upper calculations and stainless steel pins for the lower.

Figure 3.2 shows the DOT RZ model. Again, this model is similar to that described in Reference 5. The RZ model corresponds to the reactor geometry at 0°, since this azimuth corresponded to the location of the peak flux on the lower weld prior to insertion of the PLSA elements and was the region of most interest in assessing the effect of the PLSA. The same model is used in the calculations of both the upper and lower RZ channel fluxes (but the sources are different, of course). Each one-dimensional R model corresponds to the zero degree, midplane radial traverse of the pertinent RZ model.

Table 3.1 lists the atom densities of the various nuclides in the compositions appearing in the DOT models.

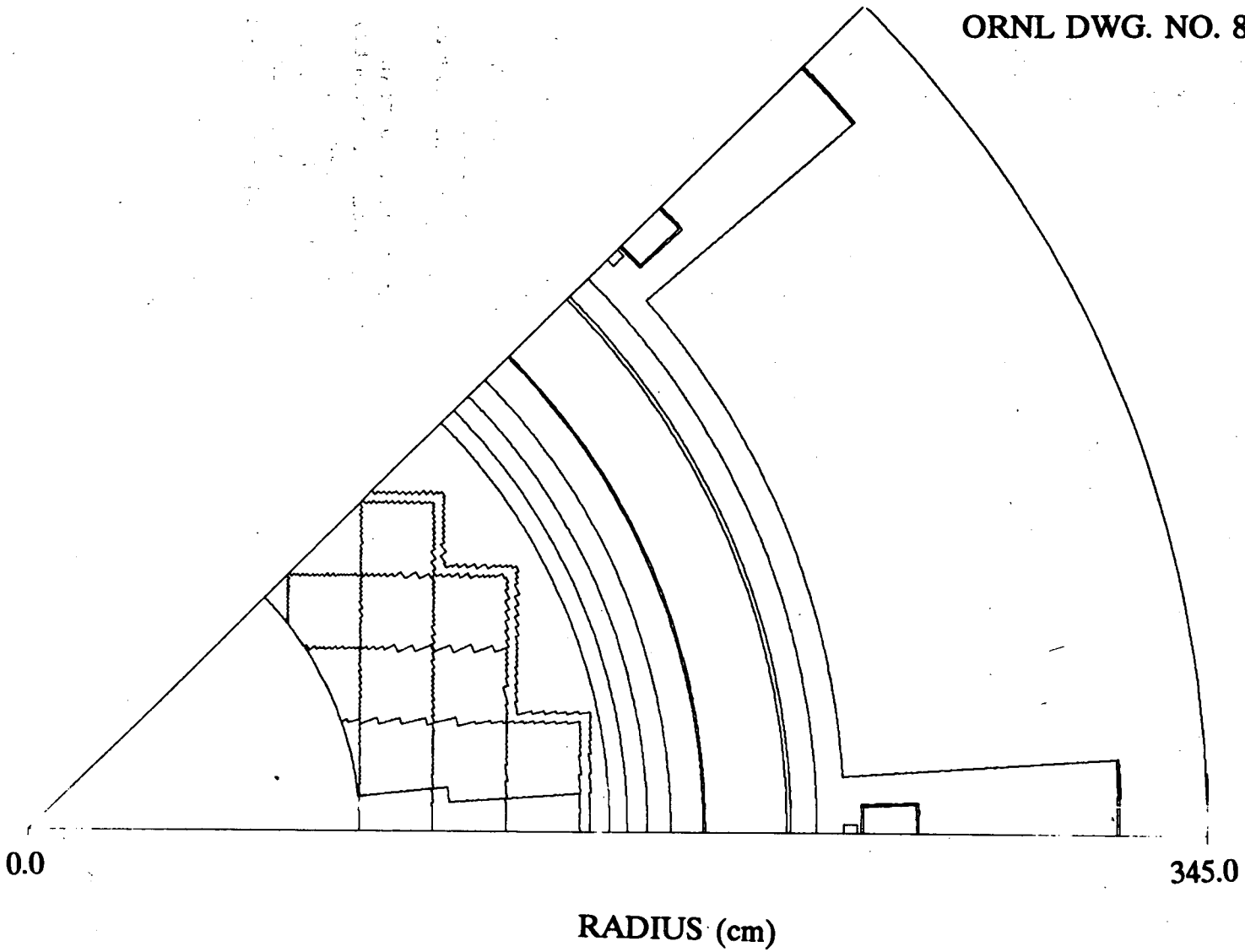

Fig. 3.1. DOT Rθ model of H. B. Robinson Unit 2.

ORNL DWG. NO. 89-19728

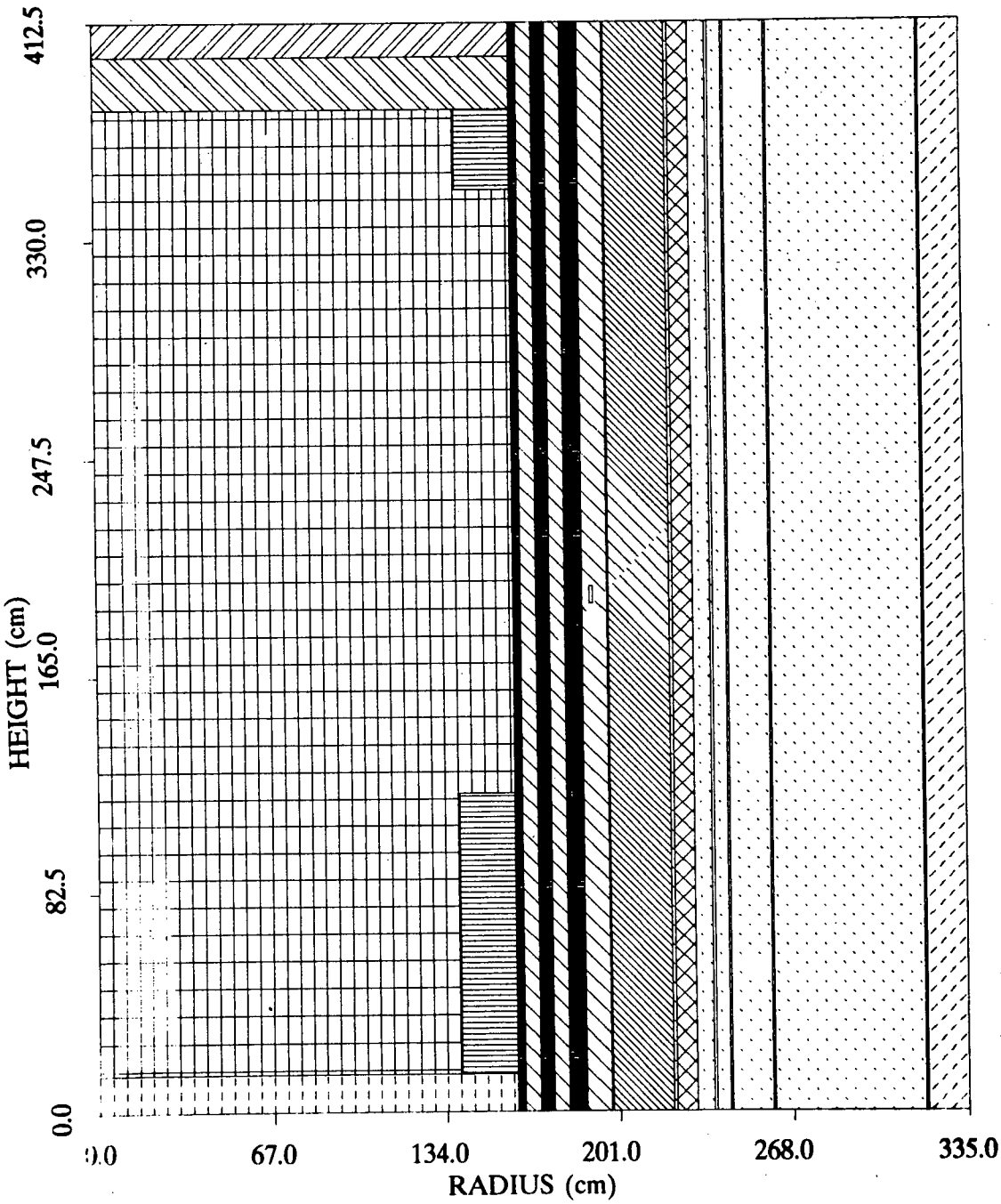

Fig. 3.2. DOT RZ model of H. B. Robinson Unit 2.

Table 3.1. Material compositions appearing in DOT models

Mixture	Component	Atom density (atom/b•cm)
Core	^{235}U	2.256E-4
	^{238}U	6.740E-3
	O	2.811E-2
	H	2.836E-2
	^{10}B	2.550E-6
	Fe	1.069E-4
	Mn	1.976E-6
	Cr	0.162E-5
	Ni	1.291E-4
	Zr	4.348E-3
Stainless steel	Fe	5.978E-2
	Mn	1.761E-3
	Cr	1.768E-2
	Ni	8.242E-3
Coolant	H	5.046E-2
	O	2.523E-2
	^{10}B	4.538E-6
Reactor vessel	C	9.820E-4
	Mn	1.116E-3
	Fe	8.270E-2
	Ni	4.420E-4
Concrete	H	6.874E-3
	C	1.115E-4
	O	4.324E-2
	Na	9.644E-4
	Mg	1.239E-4
	Al	1.742E-3
	Si	1.663E-2
	K	4.608E-4
	Ca	1.503E-3
	Fe	9.380E-4
Partial length shield assembly	O	1.418E-2
	H	2.836E-2
	^{10}B	2.550E-6
	Fe	1.709E-2
	Mn	5.020E-4
	Cr	5.085E-3
	Ni	2.471E-3
	Zr	4.348E-3

3.3 CROSS-SECTION DATA

The multi-group, neutron and gamma cross-section data used in the transport calculations were mostly obtained from the SAILOR cross-section library,[10] with an important modification discussed in the next paragraph. The group structures for the 47 neutron and 20 gamma groups are given in Tables 3.2 and 3.3. The dosimeter activation cross sections in the SAILOR library are known to contain several errors [e.g., $^{63}Cu(n,\alpha)$, $^{59}Co(n,\gamma)$, $^{235}U(n,f)$, etc.], and therefore a different reference has been used for the response functions. A 620-group set of response cross sections based on the ENDF/B-V dosimetry file were collapsed into the 47-group structure using an appropriate weight function, and these data were used to compute the dosimeter reaction rates. A listing of the activation cross sections and the displacements per atom (dpa) response function for iron is given in Table 3.4.

The iron cross section contained in the SAILOR library is based on ENDF/B-IV data, which are known to over-attenuate the fast flux through the RPV. Recently, a new iron evaluation has been performed by C. Y. Fu at ORNL, which will be the basis for the ENDF/B-VI iron data soon to be released. The new iron cross section appears to produce more accurate calculations compared to integral measurements[5] and has been recommended for RPV dosimetry analysis[8]—especially for cavity dosimetry calculations that are strongly affected by the vessel attenuation of the flux. This new iron cross section was recently processed into the SAILOR group structure and has been used in the present transport calculations. Table 3.5 compares the iron group-wise removal cross sections ($\Sigma_{tg} - \Sigma_{gg}$) based on the Fu evaluation with the original SAILOR values for the energy range above 0.111 MeV. It can be seen that the new iron cross section has a lower group removal cross section in the energy range above 3 MeV due to modifications to the inelastic scatter data, resulting in less attenuation of the high-energy flux. This new iron data contains no changes in the inelastic data below 3 MeV, although it is possible that future evaluations could also change this energy range, which has an important impact on the flux above 1 MeV. Some large differences in the removal cross sections are also found in the energy range from 0.111 to about 0.5 MeV. These differences are <u>not</u> caused by the changes to the inelastic data and are presumably caused by processing variations, since the basic data should be similar in this range. For example, a different cut-off value between the fission spectrum and 1/E weight functions used in the multigroup averaging can affect the elastic removal values. Elastic scatter in iron will only reduce the energy of neutron by a small amount per collision and usually the integrated flux above 1 MeV. The group removal cross sections below 0.5 MeV are about an order of magnitude lower than the values above 2 MeV. The cavity flux spectrum as well as the magnitude of the integrated flux above 1 MeV computed using the new iron cross section should be considerably different than the results obtained with the original SAILOR iron cross sections.

Table 3.2. Forty-seven neutron group energy boundaries

Energy group	Upper limit (MeV)	Lower limit (MeV)
1	1.733E+01	1.419E+01
2	1.419E+01	1.221E+01
3	1.221E+01	1.000E+01
4	1.000E+01	8.607E+00
5	8.607E+00	7.408E+00
6	7.408E+00	6.065E+01
7	6.065E+00	4.966E+01
8	4.966E+00	3.679E+01
9	3.679E+00	3.012E+00
10	3.012E+00	2.725E+00
11	2.725E+00	2.466E+00
12	2.466E+00	2.365E+00
13	2.365E+00	2.346E+00
14	2.346E+00	2.231E+00
15	2.231E+00	1.920E+00
16	1.920E+00	1.653E+00
17	1.653E+00	1.353E+00
18	1.353E+00	1.003E+00
19	1.003E+00	8.208E-01
20	8.208E-01	7.427E-01
21	7.427E-01	6.081E-01
22	6.081E-01	4.979E-01
23	4.979E-01	3.688E-01
24	3.688E-01	2.972E-01
25	2.972E-01	1.832E-01
26	1.832E-01	1.111E-01
27	1.111E-01	6.738E-02
28	6.738E-02	4.087E-02
29	4.087E-02	3.183E-02
30	3.183E-02	2.606E-02
31	2.606E-02	2.418E-02
32	2.418E-02	2.188E-02
33	2.188E-02	1.503E-02
34	1.503E-02	7.102E-03
35	7.102E-03	3.355E-03
36	3.355E-03	1.585E-03
37	1.585E-03	4.540E-04
38	4.540E-04	2.144E-04
39	2.144E-04	1.013E-04
40	1.013E-04	3.727E-05
41	3.727E-05	1.068E-05

Table 3.2. (continued)

Energy group	Upper limit (MeV)	Lower limit (MeV)
42	1.068E-05	5.043E-06
43	5.043E-06	1.855E-06
44	1.855E-06	8.764E-07
45	8.764E-07	4.140E-07
46	4.140E-07	1.000E-07
47	1.000E-07	1.000E-11

Table 3.3. Twenty gamma group energy boundaries

Energy group	Upper limit (MeV)	Lower limit (MeV)
1	1.400E+01	1.000E+01
2	1.000E+01	8.000E+00
3	8.000E+00	7.000E+00
4	7.000E+00	6.000E+00
5	6.000E+00	5.000E+00
6	5.000E+00	4.000E+00
7	4.000E+00	3.000E+00
8	3.000E+00	2.000E+00
9	2.000E+00	1.500E+00
10	1.500E+00	1.000E-01
11	1.000E+00	8.000E-01
12	8.000E-01	7.000E-01
13	7.000E-01	6.000E-01
14	6.000E-01	4.000E-01
15	4.000E-01	2.000E-01
16	2.000E-01	1.000E-01
17	1.000E-01	6.000E-02
18	6.000E-02	3.000E-02
19	3.000E-02	2.000E-02
20	2.000E-02	1.000E-02

Table 3.4. Dosimeter activation cross sections[a]

Group	Upper energy[b]	$^{59}Co(n,\gamma)$	$^{237}Np(n,f)$	$^{235}U(n,f)$	$^{238}U(n,f)$	$^{54}Fe(n,p)$	$^{58}Ni(n,p)$	dpa
1	1.733+01[c]	8.013-28	2.498-24	2.084-24	1.211-24	2.840-25	3.263-25	2.922-21
2	1.419+01	8.374-28	2.309-24	1.899-24	1.030-24	4.280-25	5.004-25	2.646-21
3	1.221+01	7.616-28	2.342-24	1.739-24	9.850-25	4.729-25	5.743-25	2.409-21
4	1.000+01	6.970-28	2.325-24	1.768-24	9.935-25	4.770-25	5.973-25	2.219-21
5	8.607+00	9.554-28	2.242-24	1.760-24	9.896-25	4.758-25	5.988-25	2.087-21
6	7.408+00	2.221-27	1.926-24	1.399-24	8.194-25	4.686-25	5.840-25	1.943-21
7	6.065+00	2.456-27	1.516-24	1.061-24	5.577-25	4.256-25	5.129-25	1.784-21
8	4.966+00	2.879-27	1.548-24	1.122-24	5.452-25	3.024-25	3.826-25	1.571-21
9	3.679+00	3.271-27	1.634-24	1.190-24	5.292-25	1.996-25	2.417-25	1.370-21
10	3.012+00	3.527-27	1.681-24	1.233-24	5.283-25	1.363-25	1.668-25	1.271-21
11	2.725+00	3.775-27	1.698-24	1.260-24	5.365-25	8.057-26	1.226-25	1.275-21
12	2.466+00	3.943-27	1.695-24	1.276-24	5.398-25	5.727-26	9.355-26	1.172-21
13	2.365+00	4.013-27	1.694-24	1.282-24	5.404-25	5.094-26	8.203-26	1.096-21
14	2.346+00	4.090-27	1.692-24	1.286-24	5.410-25	4.576-26	7.263-26	1.041-21
15	2.231+00	4.341-27	1.676-24	1.295-24	5.352-25	2.876-26	4.606-26	1.034-21
16	1.920+00	4.954-27	1.646-24	1.285-24	4.776-25	8.322-27	2.428-26	8.133-22
17	1.653+00	6.243-27	1.605-24	1.252-24	3.096-25	2.835-27	1.203-26	8.103-22
18	1.353+00	8.207-27	1.538-24	1.221-24	4.800-26	6.891-28	3.788-27	5.603-22
19	1.003+00	7.460-27	1.391-24	1.178-24	1.287-26	5.337-29	1.365-27	3.665-22
20	8.208-01	6.502-27	1.206-24	1.139-24	3.896-27	4.595-30	1.156-27	5.609-22
21	7.427-01	6.926-27	9.902-25	1.139-24	1.566-27	7.227-31	9.887-28	3.614-22
22	6.081-01	7.595-27	6.485-25	1.155-24	6.232-28	1.118-31	7.955-28	2.943-22
23	4.979-01	9.212-27	2.837-25	1.195-24	2.792-28	7.917-32	5.998-28	3.964-22
24	3.688-01	8.749-27	1.205-25	1.245-24	1.611-28	5.566-32	4.452-28	2.068-22
25	2.972-01	1.084-26	5.263-26	1.327-24	9.818-29	3.256-32	2.931-28	2.005-22
26	1.832-01	1.339-26	3.261-26	1.472-24	7.582-29	1.062-32	1.488-28	1.410-22
27	1.111-01	1.698-26	2.247-26	1.621-24	6.011-29	2.846-34	5.910-29	1.293-22
28	6.738-02	3.004-26	1.360-26	1.804-24	6.175-29	0.000-01	7.826-30	6.477-23
29	4.087-02	3.060-26	1.107-26	1.919-24	6.984-29	0.000-01	0.000-01	8.092-23
30	3.183-02	4.242-26	1.126-26	2.067-24	7.897-29	0.000-01	0.000-01	2.843-22
31	2.606-02	7.333-26	1.134-26	2.119-24	8.353-29	0.000-01	0.000-01	2.016-23
32	2.418-02	3.877-26	1.139-26	2.175-24	8.620-29	0.000-01	0.000-01	4.379-24
33	2.188-02	5.659-26	1.149-26	2.282-24	9.268-29	0.000-01	0.000-01	8.190-24
34	1.503-02	9.672-26	1.166-26	2.825-24	9.678-29	0.000-01	0.000-01	1.876-23
35	7.102-03	1.868-25	1.029-26	4.048-24	3.213-29	0.000-01	0.000-01	8.895-24
36	3.355-03	4.396-26	1.555-26	5.719-24	3.426-33	0.000-01	0.000-01	3.520-24
37	1.585-03	2.460-26	2.630-26	9.926-24	7.814-28	0.000-01	0.000-01	1.682-24
38	4.540-04	2.439-25	3.858-26	1.641-23	1.411-29	0.000-01	0.000-01	9.858-26
39	2.144-04	7.391-23	8.127-26	2.043-23	1.784-29	0.000-01	0.000-01	1.434-25
40	1.013-04	2.790-24	9.021-26	3.490-23	3.457-29	0.000-01	0.000-01	2.231-25
41	3.727-05	1.730-24	2.268-26	5.067-23	1.491-28	0.000-01	0.000-01	3.939-25
42	1.068-05	2.381-24	8.438-27	5.018-23	7.940-29	0.000-01	0.000-01	6.427-25
43	5.043-06	3.533-24	3.853-27	1.656-23	5.488-31	0.000-01	0.000-01	1.000-24
44	1.855-06	5.343-24	9.447-27	4.395-23	6.103-31	0.000-01	0.000-01	1.537-24
45	8.764-07	7.724-24	1.055-26	7.163-23	1.089-30	0.000-01	0.000-01	2.244-24
46	4.140-07	1.343-23	5.687-27	1.875-22	1.901-30	0.000-01	0.000-01	3.918-24
47	1.000-07	3.199-23	1.554-26	4.875-22	4.536-30	0.000-01	0.000-01	9.348-24

[a]Cross section units are cm^2 per atom; dpa is the response function corresponding to atomic displacement rate per atom, for a unit flux.

[b]Upper energy is in units of MeV.

[c]Read as $1.733 \times 10^{+01}$, etc.

Table 3.5. Comparison of iron removal cross sections based on Fu evaluation with original SAILOR values

Group	Upper energy (MeV)	Fu iron (barns)	Original SAILOR iron (barns)	SAILOR / Fu
1	1.733E+01	1.36701	1.47405	1.078
2	1.419E+01	1.34232	1.43910	1.072
3	1.221E+01	1.42680	1.52700	1.070
4	1.000E+01	1.44428	1.57390	1.090
5	8.607E+00	1.46969	1.62050	1.103
6	7.408E+00	1.48475	1.63610	1.102
7	6.065E+00	1.48878	1.67460	1.125
8	4.966E+00	1.38092	1.53340	1.110
9	3.679E+00	1.46893	1.47160	1.002
10	3.012E+00	1.54071	1.52300	0.989
11	2.725E+00	1.47860	1.48640	1.005
12	2.466E+00	1.86280	1.95730	1.051
13	2.365E+00	2.07433	2.13435	1.029
14	2.346E+00	1.65694	1.68670	1.018
15	2.231E+00	1.25529	1.31420	1.047
16	1.920E+00	1.05584	1.08160	1.024
17	1.653E+00	0.95630	0.99850	1.013
18	1.353E+00	0.58600	0.62030	1.059
19	1.003E+00	0.52590	0.51970	0.988
20	8.208E-01	1.12842	1.21770	1.079
21	7.427E-01	0.27491	0.29230	1.063
22	6.081E-01	0.38717	0.39280	1.015
23	4.979E-01	0.32585	0.39170	1.202
24	3.688E-01	0.13018	0.20480	1.573
25	2.972E-01	0.18983	0.26230	1.382
26	1.832E-01	0.13061	0.18580	1.423
27	1.111E-01	0.24688	0.27810	1.127

3.4 DETERMINATION OF CORE SOURCE DISTRIBUTION

The source distributions input to the various DOT calculations were based on the cycle 10 burnup distribution that was provided by Westinghouse. Table 3.6 gives the burnup by assembly for cycle 10 – the assembly identification numbers referred to in this table are shown in Fig. 3.3. Note that the burnup values for the assemblies that are not numbered can be obtained by reflection about the 45° plane. The values in the column labeled "Delta burnup" are equal to the amount of burnup in MWd/MTU accumulated by each assembly during cycle 10. The values in the column labeled "Relative burnup" were obtained by dividing the respective delta burnup values by the average delta burnup of all assemblies during cycle 10, which was computed to be 10,744 MWd/MTU. The time-integrated assembly power (i.e., energy production) during cycle 10 is obtained by multiplying the burnup by the mass of uranium in the assembly. The PLSA assemblies contain about 29% less fuel than the other assemblies. These results were used to compute the cycle-averaged, relative assembly-wise power distribution for cycle 10. The absolute assembly-wise power values are obtained by multiplying the relative powers by the average power per assembly, which at full power is equal to:

$$P_{average} = \frac{2300 \text{ MW(t)}}{157 \text{ assemblies}} = 14.65 \frac{\text{Mw(t)}}{\text{assembly}} .$$

The axial shape of the cycle-averaged power was obtained from the relative axial burnup data for each 30.48-cm (1-ft) segment of the core height, which was provided by Westinghouse for all assemblies. Rather than considering a different axial power shape for each assembly, three typical distributions were actually used in defining the DOT sources. The three axial shapes are given in Table 3.7 and were obtained as follows:

1. Axial power distribution for all interior elements assumed to be same as for assembly number 7 in Fig. 3.3.

2. Axial power distribution for all peripheral, non-PLSA elements assumed to be same as for assembly number 30.

3. Axial power distribution for all PLSA elements assumed to be the weighted average of the distributions within assembly 16 (weight = 2/3) and assembly 8 (weight = 1/3).

   Within each axial segment the relative power is assumed constant and equal to the average value given in Table 3.7.

Table 3.6. Cycle 10 assembly-wise burnup data

Assembly number	BOC[a] burnup (MWd/MTU)	EOC[a] burnup (MWd/MTU)	Delta[b] burnup (MWd/MTU)	Relative burnup
1	0	14093	14093	1.312
2	13396	25496	12100	1.126
3	23425	33971	10546	0.982
4	0	14366	14366	1.338
5	12077	24514	12437	1.158
6	20915	32199	11284	1.050
7	0	12495	12495	1.164
8	0	4805	4805	0.316
9	13152	25242	12090	1.126
10	12384	24401	12017	1.118
11	11399	23268	11869	1.105
12	24205	34992	10787	1.004
13	10180	22944	12764	1.188
14	7743	20699	12956	1.206
15	0	12174	12174	1.133
16	0	3955	3955	0.261
17	23410	33582	10172	0.946
18	11298	22739	11441	1.065
19	22544	33196	10625	0.989
20	0	14315	14315	1.332
21	20143	31524	11381	0.059
22	19533	30556	11023	1.026
23	0	10155	10155	0.945
24	0	13800	13800	1.284
25	23781	33980	10109	0.949
26	0	13745	13745	1.279
27	22195	33253	11058	1.029
28	8599	21446	12847	1.196
29	0	12689	12689	1.181
30	0	7954	7954	0.740
31	11988	24217	12229	1.138
32	10248	22558	12310	1.146
33	20069	31005	10936	1.018
34	8697	21137	12440	1.158
35	0	12346	12346	1.149
36	20025	26076	6051	0.563

[a]BOC = Beginning of cycle; EOC = End of cycle.
[b]Delta burnup = (EOC - BOC) burnup.

Table 3.7. Relative axial burnup distribution[a] for cycle 10

	Axial segment number[b]	Interior assemblies	Peripheral non-PLSA assemblies	PLSA assemblies
(Top of core)	1	0.393	0.434	0.626
	2	0.867	0.844	1.196
	3	1.150	1.087	1.483
	4	1.197	1.122	1.536
	5	1.245	1.161	1.591
	6	1.246	1.150	1.586
	7	1.283	1.174	1.629
	8	1.239	1.152	1.557
	9	1.126	1.156	0.795[c]
	10	0.971	1.117	0.0
	11	0.840	1.009	0.0
	12	0.444	0.553	0.0

[a]Each distribution is normalized to an average value of 1.0.

[b]Each segment is 30.48 cm (1 ft).

[c]This axial segment of the PLSA contains 15.24 cm (6 in.) of fuel and of stainless steel pins; accounting for this difference gives a value of 1.591 in the top half of the segment and 0.0 in the bottom (which averages to 0.795).

As discussed in Section 3.1, the sources input to the DOT RΘ calculations for the upper and low RΘ channel fluxes should be integrated over the appropriate axial intervals: e.g., the source for the upper region should be integrated from the top of the core to 76.2 cm (30.0 in.) below the core midplane; and for the lower region from 76.2 cm (30.0 in.) below the midplane to the bottom of the core. The values for these integrals are obtained from the data in Table 3.7; and, after appropriate normalization, essentially correspond to the fraction of the total assembly powers that are produced in the upper and lower axial regions, respectively, of the core. These axial fractions are given in Table 3.8.

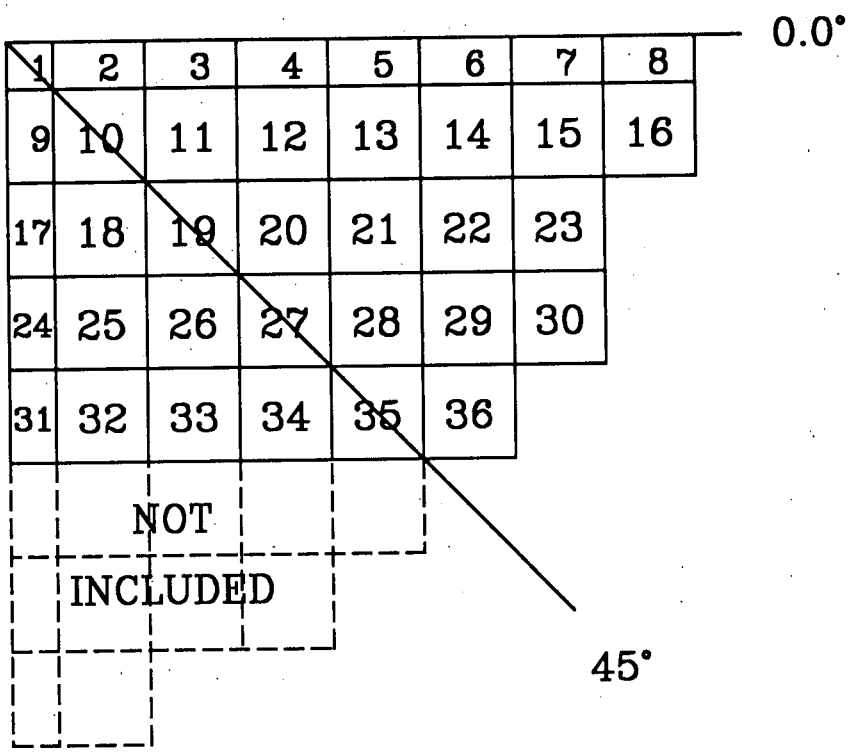

Fig. 3.3. Assembly identification numbers.

Table 3.8. Axial power fractions for the upper and lower core regions

Axial region[a]	Interior assemblies	Peripheral non-PLSA assemblies	PLSA assemblies
Lower	0.235	0.271	0.0
Upper	0.765	0.729	1.0

[a]Upper axial region extends from the top of core to 76.2 cm (30.0 in.) below midplane; lower axial region extends from 76.2 cm (30.0 in.) below midplane to bottom of core.

The final absolute power distribution by assembly is given in Table 3.9. The values in the last two columns were the basis of the absolute source distribution utilized in the upper and lower RΘ calculations. The total powers given in Table 3.9 were distributed among the 225 pin cells within the individual assemblies according to the relative pin power distribution that was provided by Westinghouse, resulting in an absolute power density (MW per cc) for each pin in both the upper and lower axial regions. The power distribution was transformed to a neutron source density (neutrons per cc per second) by multiplying by the factor 7.9×10^{16}, which is the appropriate conversion factor for a fuel burnup of about 7300 MWd/MTU. The final space-dependent RΘ source distributions for the upper and lower regions were transformed from a rectangular mesh, appropriate for describing core fuel pin arrangement, into the DOT RΘ mesh with the computer program DOTSOR.[11]

The axial distributions for the DOT RZ calculations were obtained from Table 3.8; and the radial distribution of the RZ and R variations in power were taken along the 0° direction from Table 3.9. Note that the absolute normalization of the RZ and R sources is arbitrary, as long as the two sources are normalized consistently (i.e., at any radial position, the R source should equal the integral of the RZ source over the axial dimension). The normalization of the synthesized flux depends only on the absolute normalization of the RΘ calculations.

In addition to specifying the spatial variation of the source, it is also necessary to input the energy distribution to the DOT calculations. In cycle 10, most of the fuel assemblies on the core periphery were fresh (see Table 3.6), and the average burnup of all peripheral assemblies at mid-cycle was only about 7300 MWd/MTU (the average mid-cycle burnup of the PLSA assemblies was only 2120 MWd/MTU). As the fuel burns up, plutonium fissions contribute a higher fraction of the neutron source—after about 33,000 MWd/MTU (a typical discharge exposure), approximately half the fission neutrons are produced by plutonium. The ^{239}Pu fission spectrum is somewhat harder than that of ^{235}U, and an appropriately weighted spectrum should be used to represent the energy distribution of the source for high burnup elements. However, in this case, because of the relatively low burnup of the peripheral assemblies in cycle 10, a pure ^{235}U fission spectrum based on the ENDF/B-V Watt expression has been assumed for the source energy distribution in the DOT calculations.

Table 3.9. Absolute assembly power in H. B. Robinson: Cycle 10 average

Assembly number	Total assembly power in 1/4 core[a] [MW(t)]	Upper axial region power in 1/4 core[a] [MW(t)]	Lower axial region power in 1/4 core[a] [MW(t)]
1	4.805	3.676	1.129
2	8.248	6.310	1.938
3	7.193	5.503	1.690
4	9.801	7.498	2.303
5	8.482	6.489	1.993
6	7.691	5.884	1.807
7	8.526	6.522	2.004
8	2.315	2.315	0.000
9	8.248	6.310	1.938
10	16.378	12.529	3.849
11	16.188	12.384	3.804
12	14.708	11.252	3.456
13	17.404	13.314	4.090
14	17.668	13.516	4.152
15	16.598	12.697	3.901
16	3.824	3.824	0.000
17	6.929	5.301	1.628
18	15.602	11.936	3.666
19	14.489	11.084	3.405
20	19.513	14.927	4.586
21	15.514	11.868	3.646
22	15.031	11.499	3.532
23	13.844	10.092	3.752
24	9.405	7.195	2.210
25	13.903	10.636	3.267
26	18.737	14.334	4.403
27	15.075	11.532	3.543
28	17.521	13.404	4.117
29	17.301	13.235	4.066
30	10.841	7.903	2.938
31	8.336	6.377	1.959
32	16.789	12.844	3.945
33	14.913	11.408	3.505
34	16.964	12.977	3.989
35	16.832	12.876	3.956
36	8.248	6.013	2.235

[a]N.B. – The absolute power values reflect the fraction of the assembly contained in the 1/4 core. For example, since only 1/4 of assembly number 1 is contained in each quarter core (see Fig. 3.3), the powers listed for this assembly are only 1/4 of the actual values.

3.5 CALCULATION OF DOSIMETER ACTIVITIES

The output of the various DOT transport calculations are combined in the manner discussed in Sect. 3.1 to obtain synthesized, multi-group fluxes at all locations throughout the system. In particular, this can be used to compute the responses of the various dosimeters located in the cavity. The reaction rates in the dosimeter foils, SSTRs, and gradient wires are calculated by simply summing the product of the appropriate group response function (see Table 3.4) and the group flux at the desired location. The "measured reaction rate" determined from the SSTR dosimeters is based on the total number of tracks counted for the individual track recorders and provides a direct comparison of the cycle-average fission reaction rate measured for the various nuclides with the corresponding calculated values. However, in the case of the dosimeter foils and gradient wires, the measured activity of the dosimeter activation product is used to indirectly infer the reactor rate. If the cycle-average power distribution is a good approximation for the spatial shape of the power during the entire cycle, then the average reaction rate in dosimeter "m" is related to the activation product activity by

$$A^{(m)} = K^{(m)} H^{(m)} R^{(m)} , \tag{3.6}$$

where

$A^{(m)}$ = activity of activation product, in Bq/g;

$K^{(m)}$ = factor to convert from Bq/target nucleus to Bq/g;

$H^{(m)}$ = saturation factor;

$R^{(m)}$ = cycle-average activation reaction rate, per target atom,

$$= \sum_{g=1}^{47} \sigma_g^{(m)} \phi_g .$$

As the dosimeter irradiation time at full power becomes long compared to the half-life of the activation product, the saturation factor approaches unity, and the measured activity reaches the saturated value,

$$A^{(m)}_{sat} = K^{(m)} R^{(m)} \text{ Bq/g}.$$

In general, the saturation factor is calculated from the expression,

$$H^{(m)} = \sum_{j}^{J} F_j \, (1-e^{-\lambda m T_j}) e^{-\lambda m (T-t_j)}, \qquad (3.7)$$

where

F_j = fractional power output during reactor operating period j,

T_j = length of time for reactor operation period j,

t_j = elapsed time from beginning of irradiation to end of interval j,

T = total time from beginning of irradiation to end of irradiation,

λm = decay constant of activation product,

J = number of irradiation periods.

In this case, the values for the irradiation parameters can be obtained from Table 2.1, and there was also a 174-day decay period following irradiation before the samples were counted. The decay period can also be included in Eq. (3.7) by setting $F_j = 0$ for this time interval. Table 3.10 lists the conversion factors and saturation factors for the iron and nickel dosimeters. Equation (3.6) can be used to convert the reaction rates calculated with DOT into the corresponding dosimeter activities or, conversely, the measured activities can be converted to reaction rates.

Table 3.10. Dosimeter activation factors

Dosimeter	Reaction	λ (day^{-1})	K[a]	H[b]
Iron foil	$^{54}Fe(n,p)^{54}Mn$	2.22E-3	6.254E+20	0.330
Iron in wire	$^{54}Fe(n,p)^{54}Mn$	2.22E-3	4.478E+20	0.330
Nickel in wire	$^{58}Ni(n,p)^{58}Co$	9.77E-3	5.855E+20	0.149
Cobalt in wire	$^{59}Co(n,\gamma)^{60}Co$	3.60E-4	1.277E+19	0.101

[a]Conversion factor to convert activity from Bq/g to Bq/target nucleus, taken from Ref. 3.

[b]Saturation factor, calculated from Eq. (3.7).

4. REFERENCE RESULTS

4.1 REFERENCE CALCULATIONS AND MEASUREMENTS

The reference set of transport calculations provides a direct comparison of absolute dosimeter activities and reaction rates based on computed and experimentally measured results. There is no adjustment or normalization whatsoever of the calculations, so the observed discrepancies reflect inaccuracies in the "prior" computational, as well as experimental, analysis.

Sources of calculational inaccuracies include uncertainties in nuclear data, modeling approximations, and simplifications in representing the core power distribution. Inaccuracies in the experimental results arise from basic radiometric counting uncertainties and possible systematic errors in the measurements. Some discussion of the magnitude of the various uncertainties in the calculated and measured results will be given in the following sections. The calculated and experimental sets of results are combined in order to obtain the final adjusted parameters, as discussed in Section 4.4, but in this chapter only the unadjusted reference results are presented.

4.2 REFERENCE DOSIMETER REACTION RATES

Table 4.1 compares the absolute reaction rates from the reference calculations with the corresponding measured values for the cavity surveillance capsules at 3°, 9°, and 27°; and Table 4.2 shows the calculation to experimental (C/E) ratios obtained from the values in Table 4.1. It can be seen that the ^{54}Fe and ^{58}Ni reaction rates obtained from the reference calculations are 10-20% low at the 3° and 9° locations, but are 14-30% high at 29°. The iron and nickel measurements are based on foil and wire activation. However, the agreement between calculation and measurements for the SSTR dosimeters is not as good as for the activation results. The measured values are typically higher—perhaps indicating a systematic bias in the measurements. Due to inconsistencies among the data, Westinghouse has suggested assigning rather larger uncertainties to the ^{235}U SSTR results: a one-sigma value of 25% for the cadmium-covered and 50% for the bare reaction rates is recommended.[3]

The bare ^{235}U value at 9° is obviously an inconsistent measurement compared to the other two locations and should be discarded. Taking into account this degree of uncertainty in the experimental values, the poor agreement with the calculated ^{235}U reaction rates is not surprising.

The original results published by Westinghouse for the ^{238}U SSTR measurements in their cycle 10 analysis have been subsequently revised in their cycle 11 report[4] – the values given in Table 4.1 correspond to the latter values. The original ^{238}U measurements were reduced about a factor of two due to errors discovered in the assumed mass of the fission deposits

Table 4.1. Reference calculations and experimental values for dosimeter reaction rates

Reaction	3°		9°		27°	
	C[a]	E[b]	C	E	C	E
$^{54}Fe(n,p)$	4.180-17[c]	4.800-17 (±10%)	3.982-17	4.990-17 (±10%)	2.943-17	2.580-17 (±14%)
$^{58}Ni(n,p)$	6.256-17	6.870-17 (±15%)	5.980-17	6.850-17 (±13%)	4.374-17	3.380-17 (±19%)
$^{237}Np(n,f)$ [SSTR]	4.999-15	7.690-15	4.904-15	8.660-15	3.421-15	3.150-15
$^{238}U(n,f)$ [SSTR]	2.575-16	3.900-16	2.442-16	4.560-16	1.728-16	2.690-16
$^{235}U(n,f)$ [SSTR]	6.899-13	1.280-12	9.135-13	6.780-13	6.994-13	1.180-12
$^{235}U(n,f)_{cd}$ [SSTR]	1.428-13	3.550-13	1.758-13	3.300-13	1.373-13	1.930-13
$^{59}Co(n,\gamma)$	7.390-14	1.630-13 (±1%)	9.597-14	1.550-13 (±1%)	7.441-14	1.260-13 (±1%)

[a]Calculated value (reaction per atom per second) at full power obtained from reference calculations.

[b]Experimental value (reaction per atom per second) based on measured results (extrapolated to saturation for radiometric dosimetry). The percent statistical uncertainty (two standard deviations) is given in parentheses for activity measurements.

[c]Read as 4.180×10^{-17}.

Table 4.2. C/E values based on reference calculations

Reaction	3°	9°	27°
$^{54}Fe(n,p)^{54}Mn$	0.87	0.80	1.14
$^{58}Ni(n,p)^{58}Co$	0.91	0.87	1.29
$^{237}Np(n,f)$ [SSTR]	0.65	0.57	1.09
$^{238}U(n,f)$ [SSTR]	0.66	0.54	0.64
$^{235}U(n,f)$ [SSTR]	0.54	1.35	0.59
$^{235}U(n,f)_{cd}$ [SSTR]	0.40	0.53	0.71
$^{59}Co(n,\gamma)^{60}Co$	0.45	0.62	0.59

on the SSTRs. However, even after this downward adjustment in the measured reaction rates, the computed ^{238}U values are still 35-50% lower than the experimental values. Since the Westinghouse calculations show similar discrepancies, it is felt that the measured ^{238}U values are still at least 30% too high and this magnitude has been assigned for the uncertainty in the experimental results.

The ^{237}Np results are more puzzling. At the 3° and 9° locations, the C/E values for the ^{237}Np reaction rates are similar to those for ^{238}U values, and therefore it is possible that a similar problem exists in the neptunium SSTR specifications. (The C/E value at 27° appears inconsistent with the other two values, as discussed in the next paragraph.) However, unlike the ^{238}U case, the Westinghouse calculations do not show similar discrepancies as the ORNL calculations do for the ^{237}Np results. Specifically it appears that the Westinghouse calculations produce similar C/E values for the ^{54}Fe, ^{58}Ni and ^{237}Np reaction rates—i.e., all of the calculated reaction rates are about 30% lower than the measurements. On the other hand, the ORNL calculations give C/E values 10-15% lower for ^{54}Fe and ^{58}Ni, while the ^{237}Np value is about 40% lower. Because the ORNL transport calculations employed the newer Fu evaluation for the iron cross sections while Westinghouse used the older iron data contained in the original SAILOR library, it was decided to examine the effect of this cross-section data on the relative C/E values. The flux spectrum in the HBR cavity region was obtained from a one-dimensional transport calculation using the original SAILOR iron cross section, and the reaction rates obtained from the calculation were compared to those obtained from a similar calculation performed with the Fu iron data. The percent difference in the computed reaction parameters is given in Table 4.3. It can be seen that the Fu data tends to increase higher

threshold reaction rates more than the lower threshold reactions in the cavity. The ratio of the neptunium-to-iron reaction rates (which is also equal to the ratio of "spectrum-averaged cross sections") decreases about 20%. Thus the difference in the iron data used in the transport calculations seems to account for the inconsistencies in the C/E values obtained by Westinghouse and ORNL.

In summary, based on these results, it appears that the Fu iron evaluation will eliminate much of the observed discrepancy between calculated and measured cavity reaction rates for ^{54}Fe and ^{58}Ni dosimeters, but the ^{237}Np and ^{238}U computed results will remain low. The ^{238}U discrepancy appears to be caused by a measurement problem. There is also some question about the reliability of the Np measurements, as discussed below; however, the possibility that the new iron cross-section data continues to overestimate the neutron attenuation for the energy range below 3 MeV cannot be ruled out as a cause for the observed discrepancy.

The variation in the C/E values for ^{54}Fe, ^{58}Ni, and ^{237}Np at 3°, 9°, and 27°, respectively, seems to suggest that the azimuthal shape of the reference calculations and the measured results is somewhat different. The relative azimuthal shape of the calculated and measured reaction rates, normalized to a value of 1.0 at 3°, is shown in Table 4.4. This difference could indicate a breakdown of the two-channel synthesis approximation; however, the calculated azimuthal variation of the three dosimeters is very consistent and shows that the maximum reaction rate occurs at 3°. On the other hand, there seems to be some inconsistency in the measured results. The ^{237}Np measurement at 27° clearly is about 20-30°lower compared to the

Table 4.3. Comparison of cavity reaction rates obtained from transport calculations with original SAILOR and Fu iron cross sections

Parameter	Percent difference[a]
$^{54}Fe(n,p)$	60
$^{58}Ni(n,p)$	54
$^{238}U(n,f)$	38
$^{237}Np(n,f)$	28
Np/Fe	-20
U/Fe	-14

[a]Percent difference = $\left[\frac{\text{Fu - SAILOR}}{\text{SAILOR}}\right]$ x 100.

other two dosimeter measurements at this location. Similarly, the ^{237}Np measurement of 9° appears 10% higher than the other dosimeter measurements. Based on these apparent inconsistencies, a 25% uncertainty in the measured ^{237}Np results was assumed. In addition, the experimental measurements tend to indicate higher activities at the 9° location than the 3° location, while the opposite is seen in the computed results. This could be explained by an inaccuracy in the synthesis approximation. For example, if the contribution of the Rθ flux in the lower region is weighted more, then the peak flux could shift away from the 0° location. Unfortunately, a lack of confidence in the experimental measurements again thwarts the ability to make definitive conclusions on the accuracy of the synthesis approximation.

The C/E values for the $^{59}Co(n,\gamma)$ reaction are all substantially lower—up to a factor of two. Westinghouse recommends an uncertainty of 12% in the measured values for this dosimeter,[3] although the statistical uncertainty is much less. The large discrepancies in these results are not uncommon for thermal reactions, which are more sensitive to local perturbations and modeling approximations. Interestingly, the Westinghouse calculations also show large differences with the measurements, but their results are much higher than the experimental values. The uncertainty in the water content of the concrete reactor shields surrounding the cavity could cause the calculated thermal flux to be substantially in error.

Figures 4.1.a-4.3.c compare the axial variation of the absolute activities in the gradient wires, obtained from measurements and from the reference calculations. The calculated results for the iron and nickel wires at 3° lie essentially within the uncertainty in the measurements, but usually lie in the low end of the uncertainty band. However, the computed results of these dosimeters at 9° definitely tend to be somewhat lower at axial elevations near the midplane. At the 27° location, the iron results generally fall within the uncertainty in the experimental values at all axial locations, but the nickel calculation is too high near the midplane. As noted earlier, the computed cobalt activity is substantially lower than the measurements. The two-channel synthesis approximation appears to give a reasonable representation for the axial variation in the flux, but appears to underestimate the magnitude of the fast flux near the midplane, at least for the 3° and 9° azimuths.

Table 4.4. Relative azimuthal variation of cavity reaction rates

	3°		9°		27°	
Reaction	C	E	C	E	C	E
^{54}Fe	1.0	1.0	0.95	1.04	0.70	0.54
^{58}Ni	1.0	1.0	0.96	1.00	0.70	0.49
^{237}Np	1.0	1.0	0.98	1.13	0.68	0.41

ORNL DWG. NO. 89-19729/R1

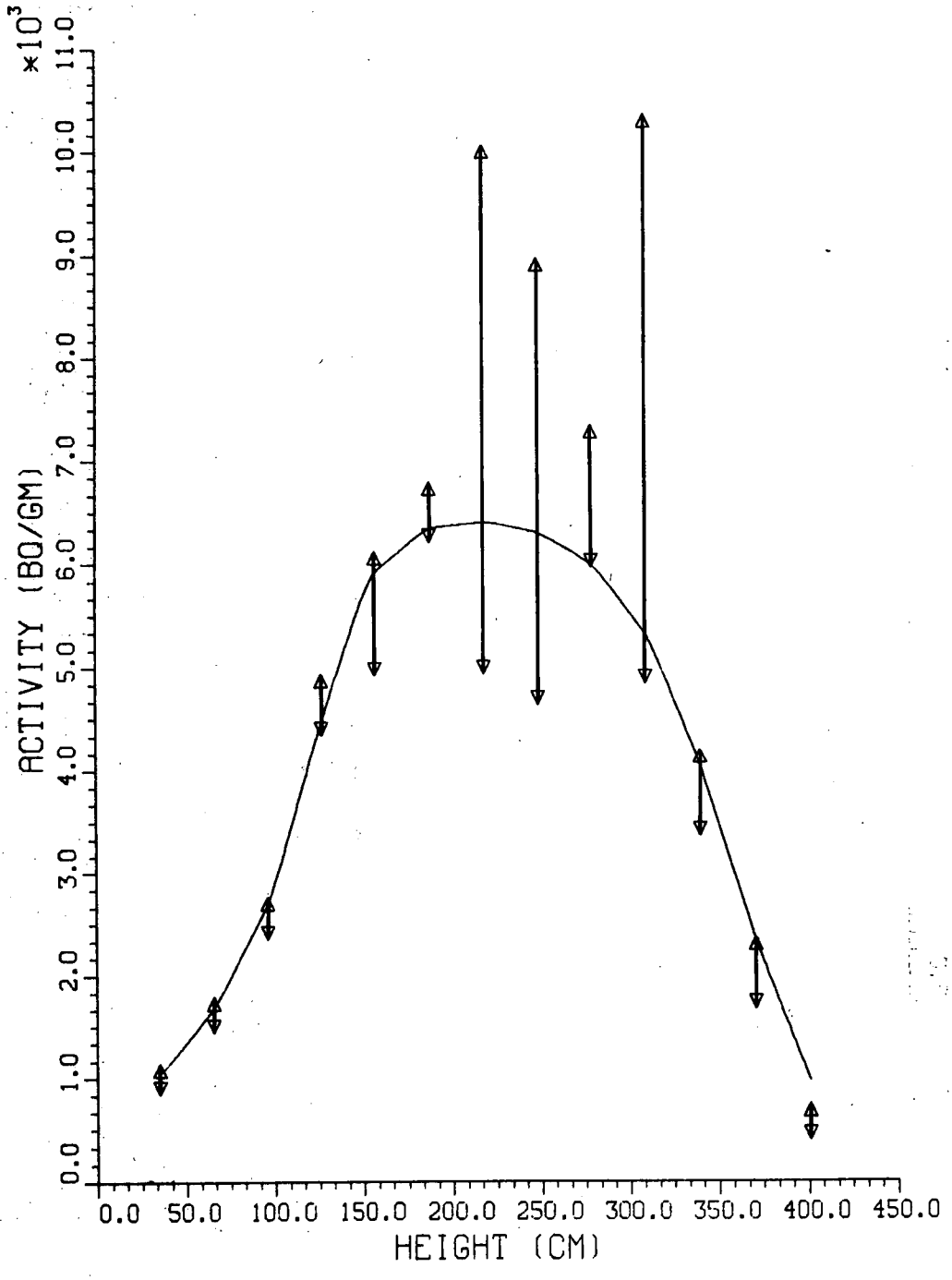

Fig. 4.1.a. Comparison of calculated and measured axial variation of 3° gradient wire activity, "Fe."

ORNL DWG. NO. 89-19730/R1

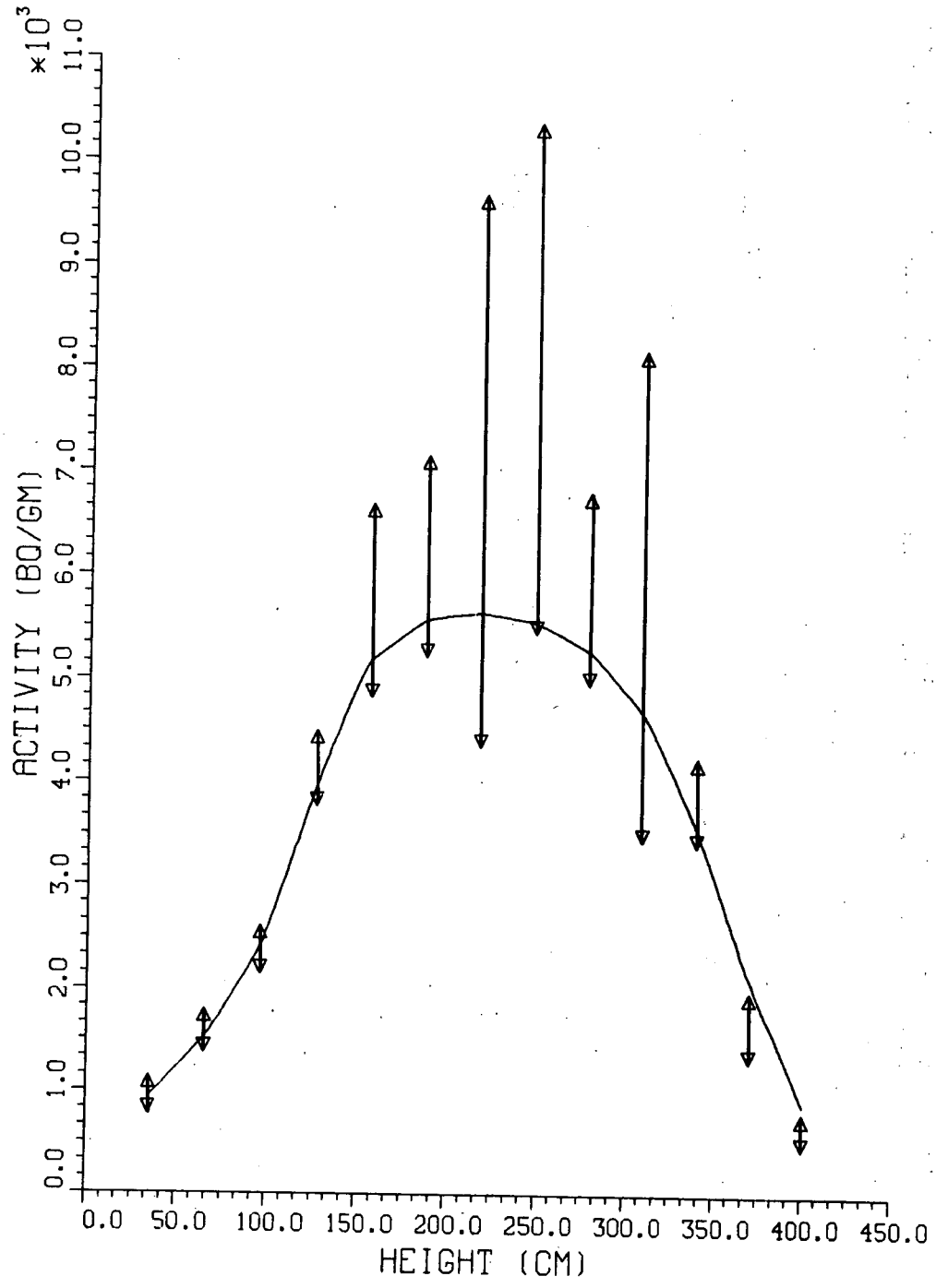

Fig. 4.1.b. Comparison of calculated and measured axial variation of 3° gradient wire activity, "Ni."

ORNL DWG. NO. 89-19731/R1

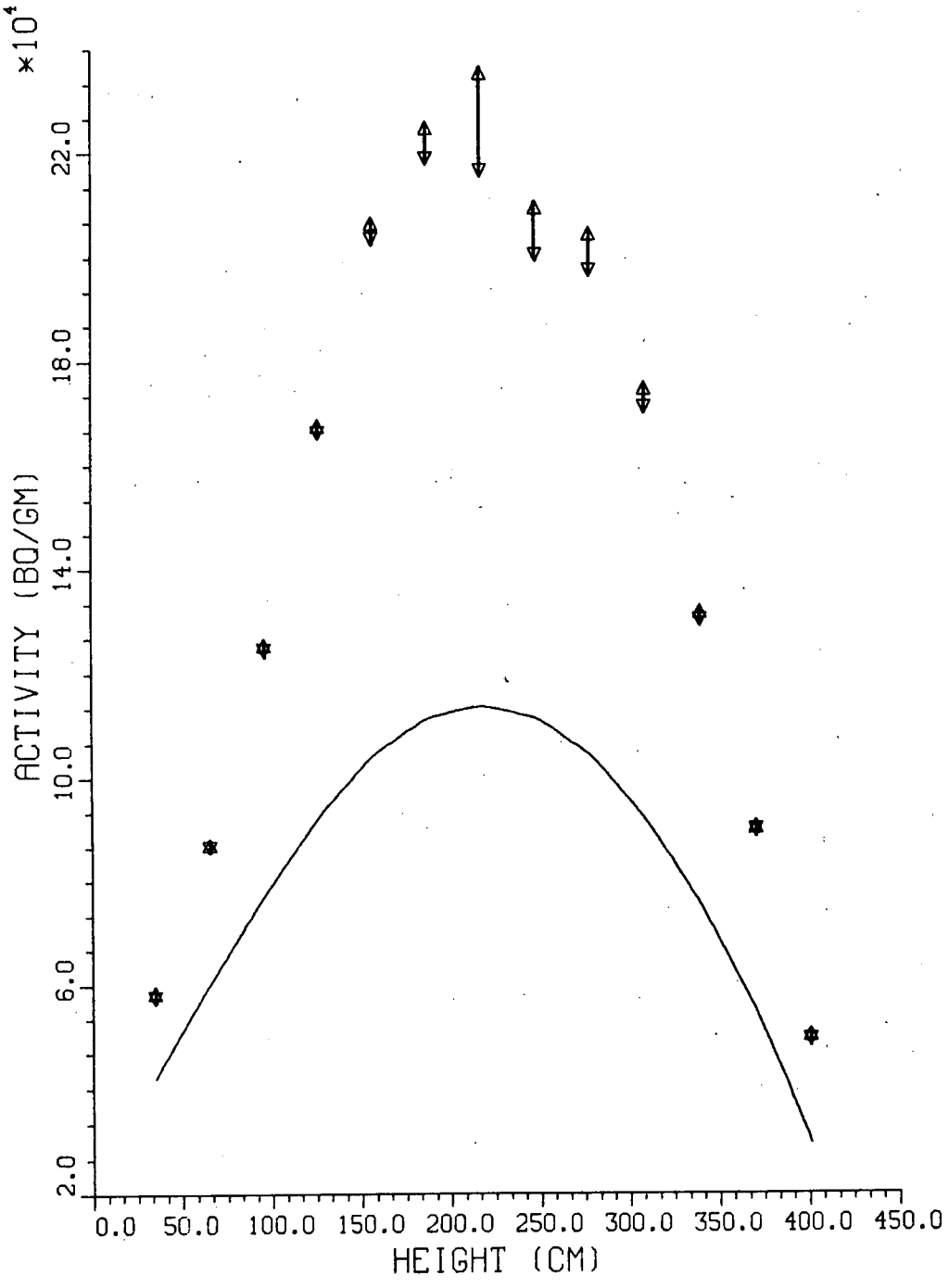

Fig. 4.1.c. Comparison of calculated and measured axial variation of 3° gradient wire activity, "Co."

ORNL DWG. NO. 89-19732/R1

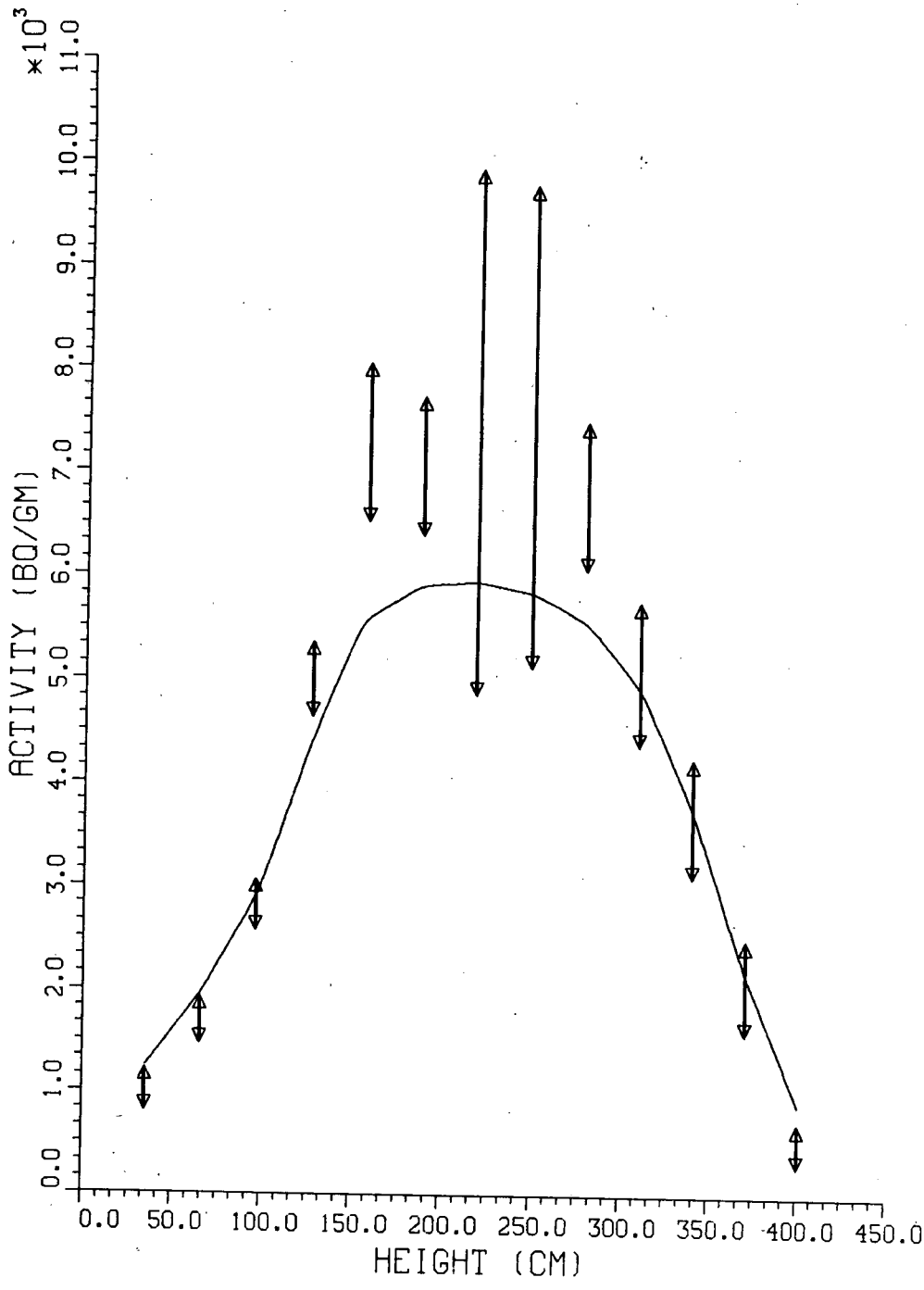

Fig. 4.2.a. Comparison of calculated and measured axial variation of 9° gradient wire activity, "Fe."

ORNL DWG. NO. 89-19733/R1

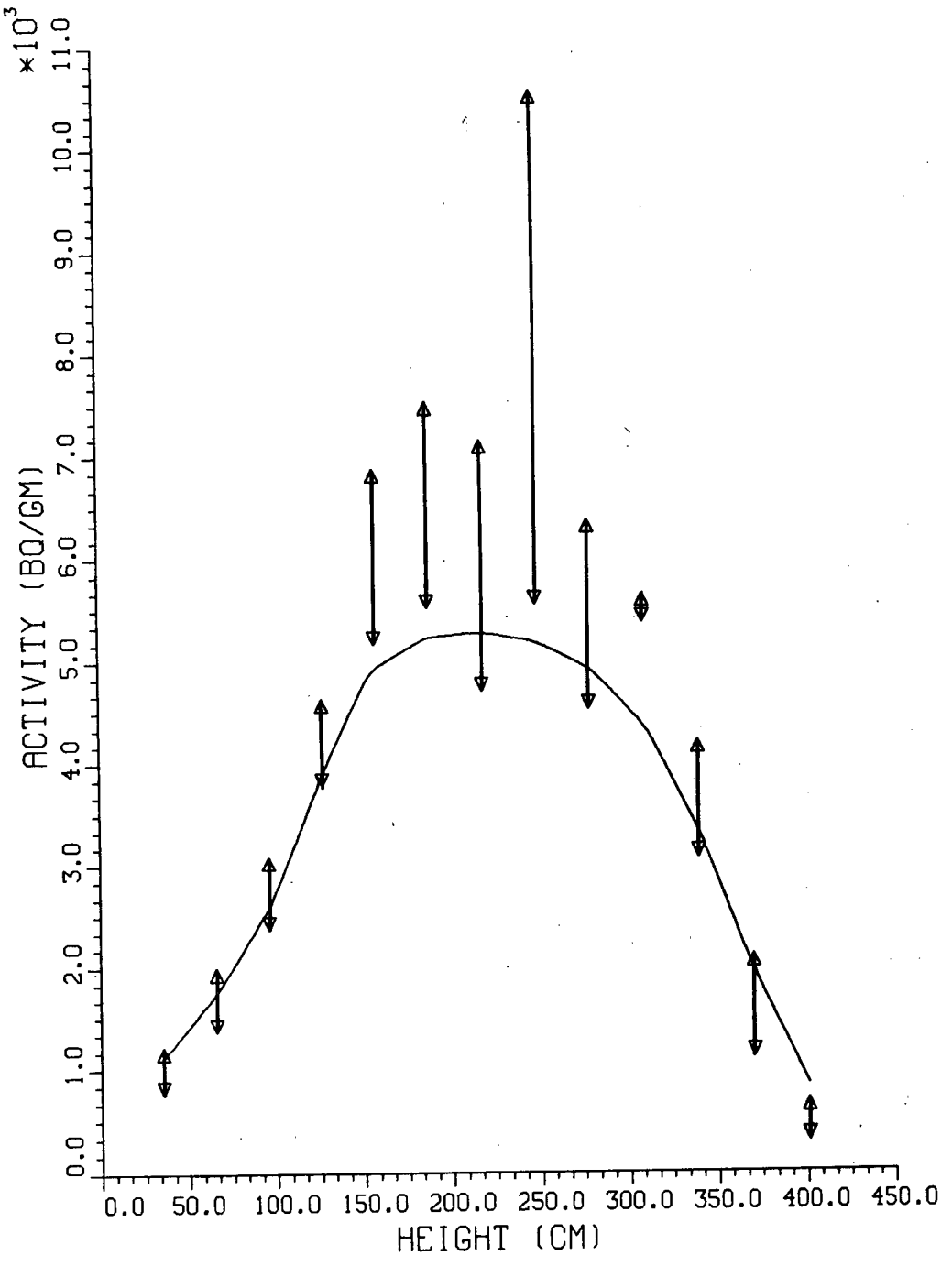

Fig. 4.2.b. Comparison of calculated and measured axial variation of 9° gradient wire activity, "Ni."

ORNL DWG. NO. 89-19734/R1

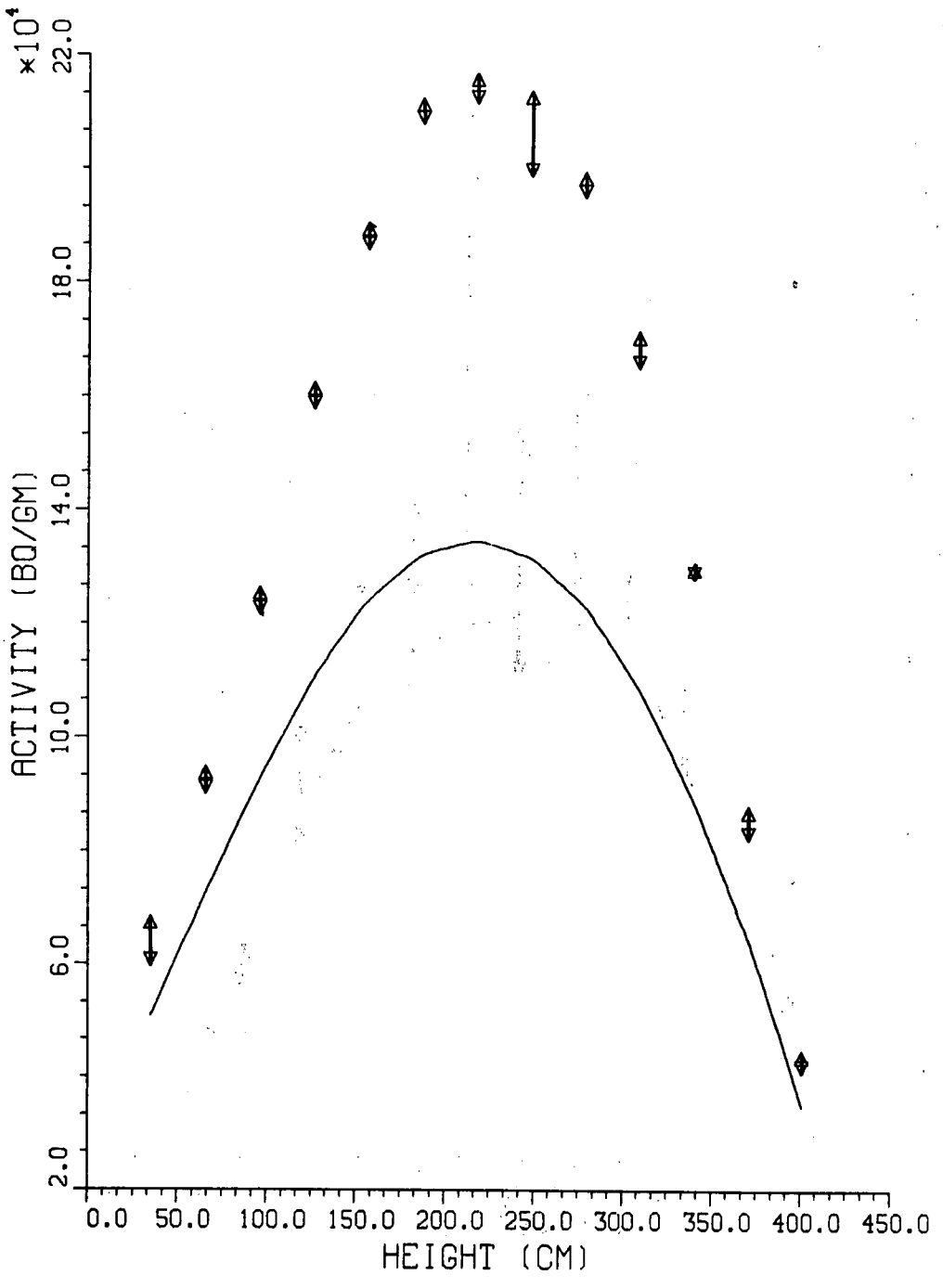

Fig. 4.2.c. Comparison of calculated and measured axial variation of 9° gradient wire activity, "Co."

ORNL DWG. NO. 89-19735/R1

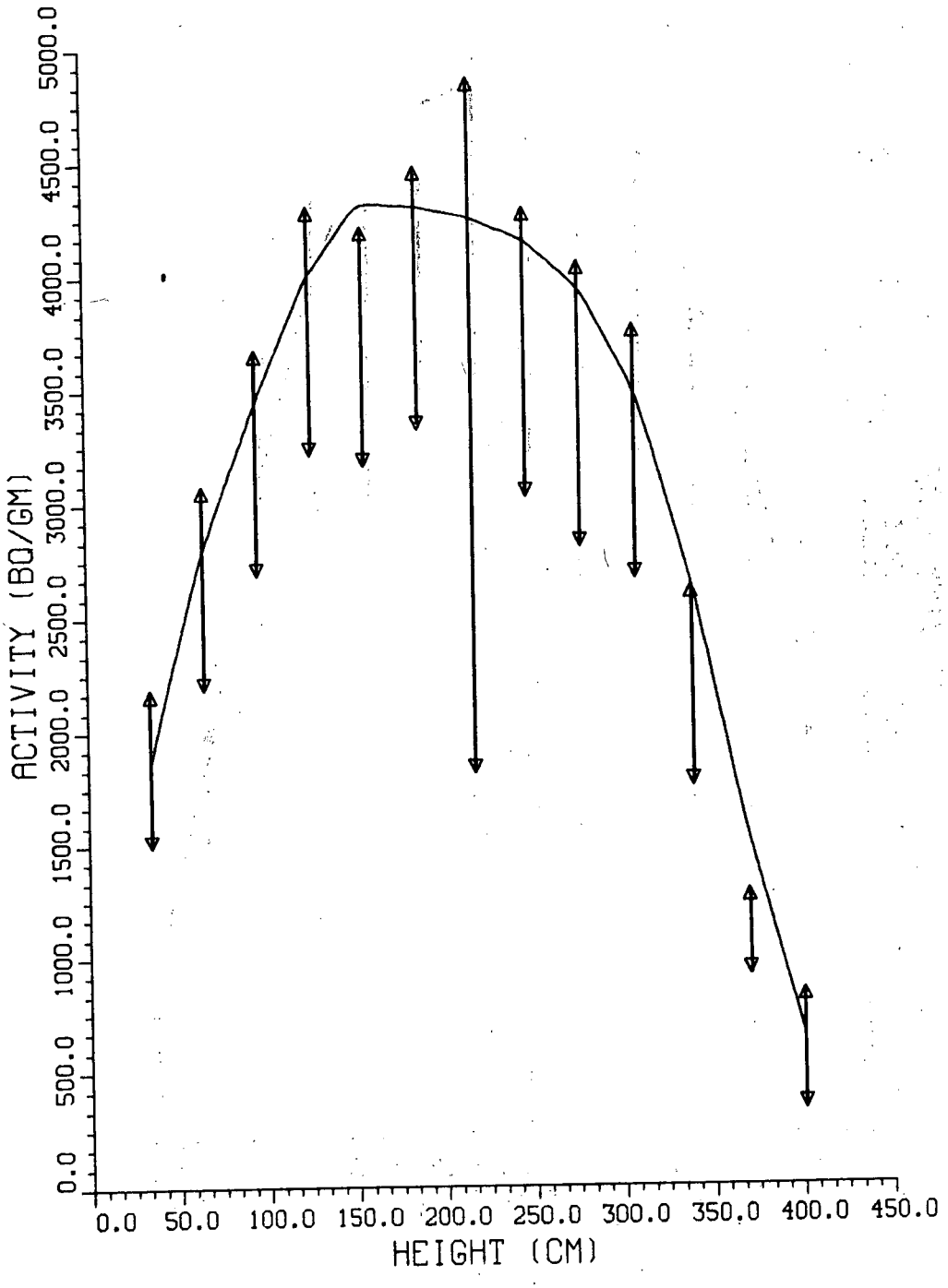

Fig. 4.3.a. Comparison of calculated and measured axial variation of 27° gradient wire activity, "Fe."

ORNL DWG. NO. 89-19736/R1

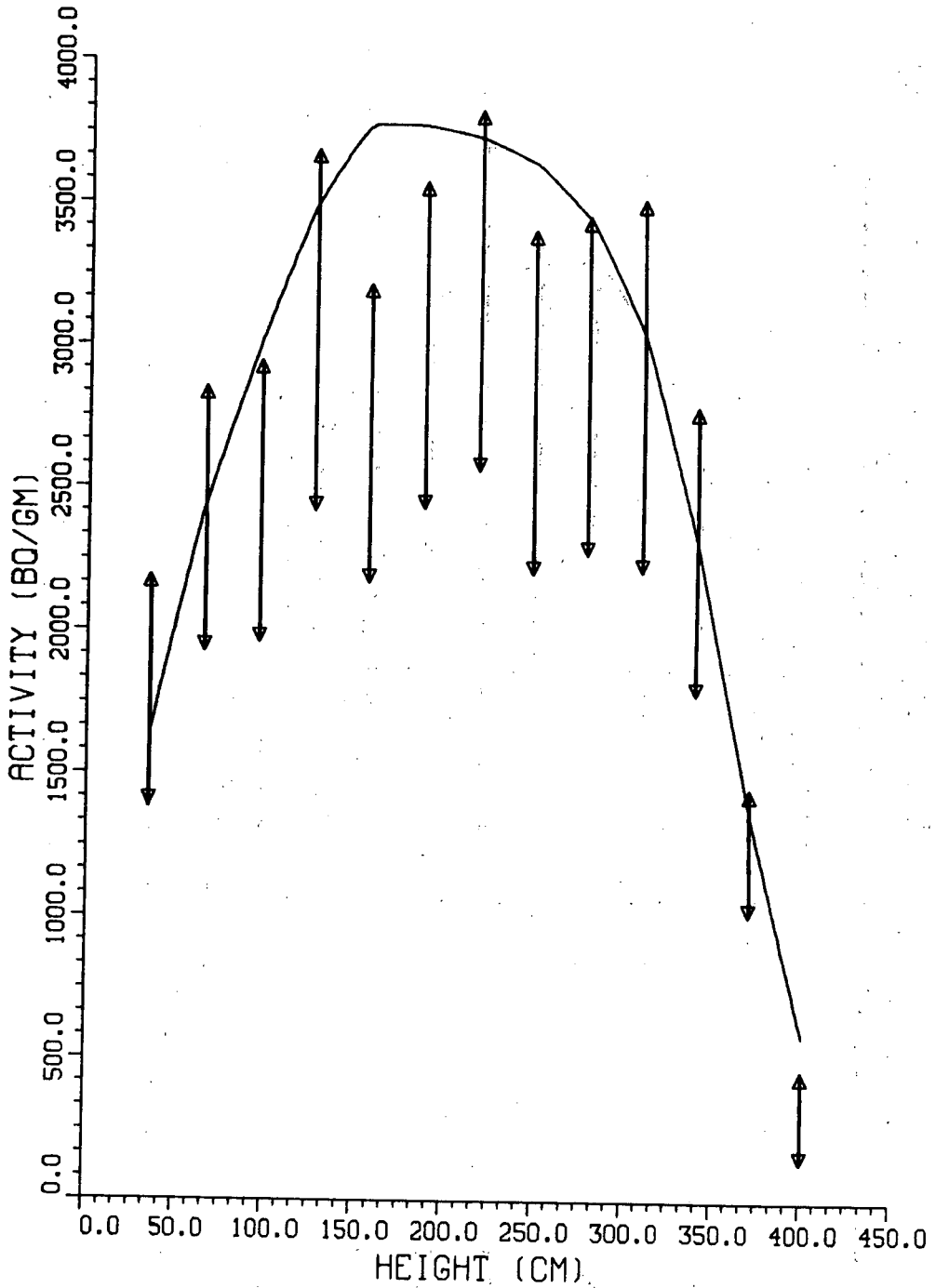

Fig. 4.3.b. Comparison of calculated and measured axial variation of 27° gradient wire activity, "Ni."

ORNL DWG. NO. 89-19737/R1

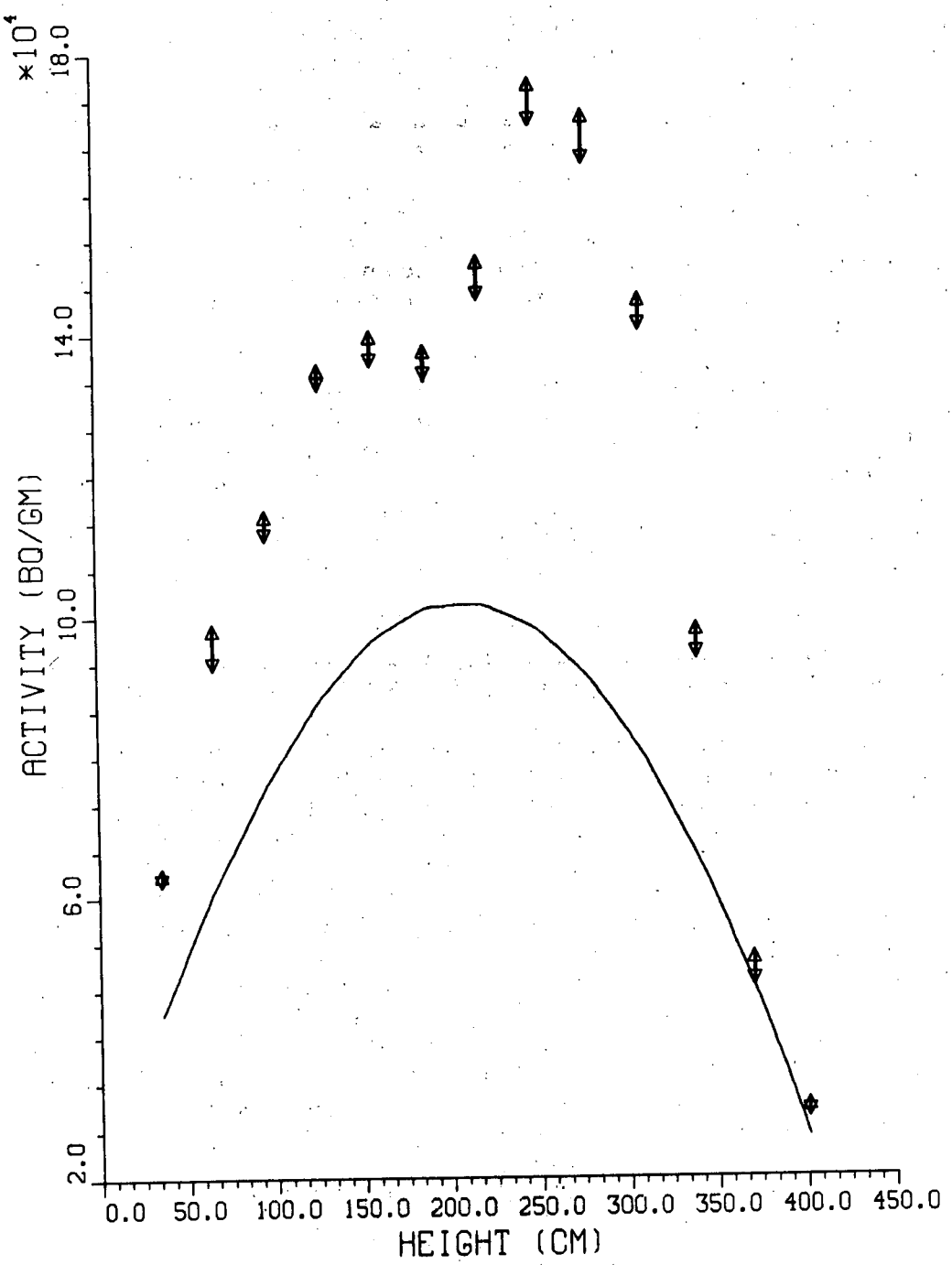

Fig. 4.3.c. Comparison of calculated and measured axial variation of 27° gradient wire activity, "Co."

4.3 REFERENCE FLUX VARIATION AND DPA RESULTS

Figures 4.4 and 4.5 show the calculated azimuthal variation in the absolute flux greater than 1 MeV, at the 0-T (i.e., clad-base metal interface in RPV) and 1/4-T locations, respectively, at the upper weld, midplane, and lower weld axial locations. Figures 4.6 and 4.7 show similar results for the dpa. It can be seen that the flux above 1 MeV and the dpa peak near 0° at the upper weld and the midplane elevations and at about 24° at the lower weld. At any axial level, the azimuthal shape of the flux is a linear combination of the upper and lower RΘ flux distributions. The upper RΘ flux peaks at 0°, while the lower distribution peaks at around 24°. Over most of the core height, the upper distribution dominates, so that the overall flux shape tends to peak near 0°. However, near the bottom of the core, the lower RΘ distribution begins to become significant, and the peak progressively shifts from 0°to 24°.

Table 4.5 lists the relative flux (E > 1 MeV) azimuthal variation at the core midplane and lower weld axial elevations at the 0-T position. The maximum value of the flux incident on the RPV at the midplane is computed in the reference calculations to be 3.79×10^{10} n/cm^2·s and at the bottom weld to be 1.57×10^{10} n/cm^2·s. The maximum dpa was calculated to be 6.18×10^{-11} at the midplane and 2.52×10^{-11} at the lower weld. Table 4.6 shows the relative radial variation of the flux and dpa through the RPV.

Figure 4.8 shows the azimuthal variation in the flux above 1 MeV within the cavity at four axial elevations. The azimuthal shape within the cavity tends to be somewhat less severe than incident on the RPV.

Figures 4.9 and 4.10 show the iso-flux and iso-dpa contours, respectively, throughout the system. It can be seen that the detector wells within the cavity have a very significant effect on the flux distribution outside the vessel, near the azimuthal locations of the wells. However, at other azimuths, the flux does not seem to be affected much by the wells.

Table 4.7 summarizes the values for integral flux and dpa responses at various locations, obtained from the reference transport calculations, with no adjustments. The absolute group-wise and group-accumulated flux and dpa spectra are listed in Tables 4.8 to 4.10, for the 0-T, 1/4-T, and 3/4-T RPV positions, respectively, at the core midplane elevation. Tables 4.11 to 4.13 give similar data at the lower weld elevation (for the peak azimuthal location of 24°), and Tables 4.14 to 4.16 for the upper weld elevation. The spectra at the three cavity dosimeter capsule locations are listed in Tables 4.17 to 4.19. Figures 4.11 to 4.14 show plots of the flux spectra at the locations corresponding to Tables 4.11 to 4.19.

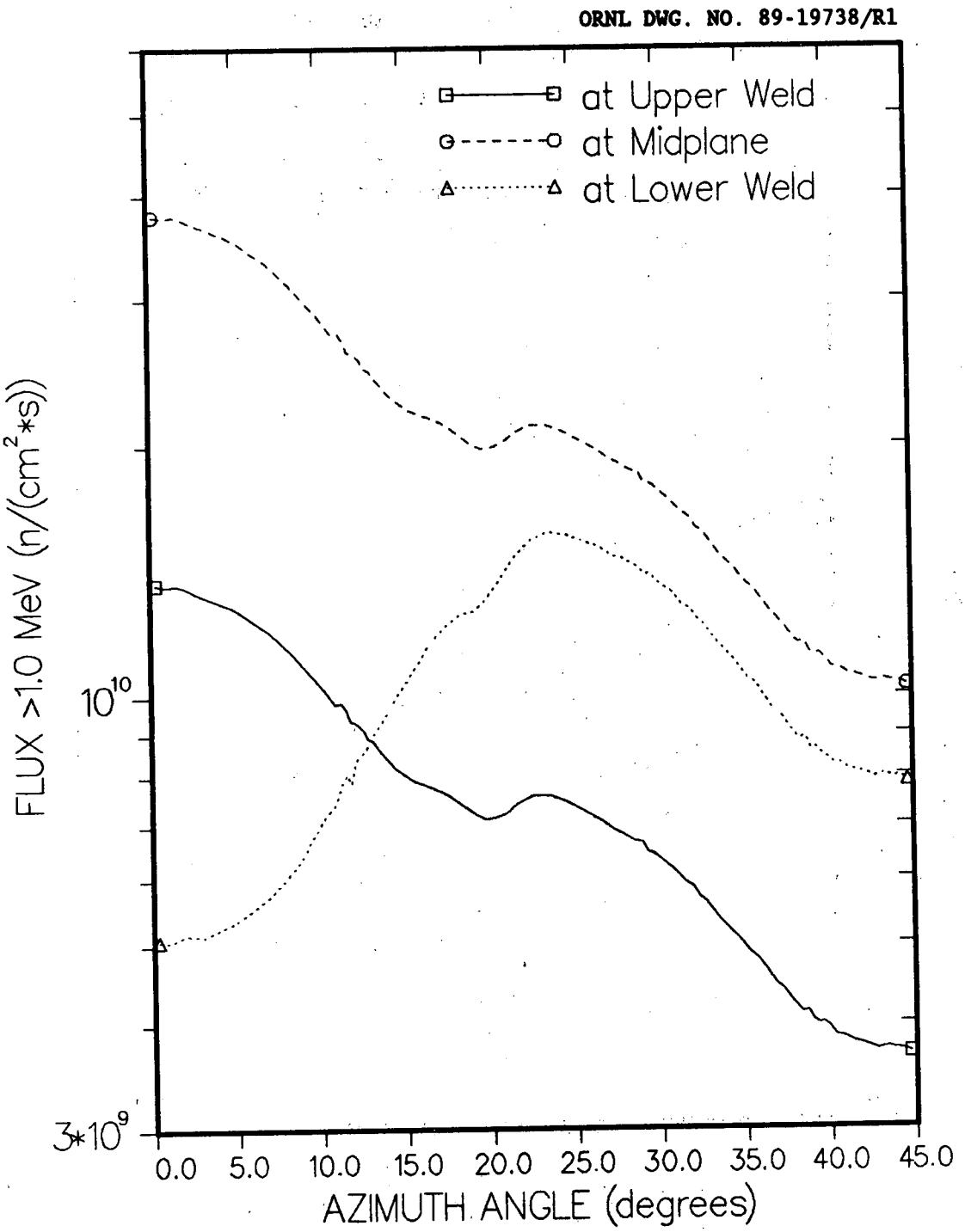

Fig. 4.4. Azimuthal variation in ϕ(>1 MeV) at 0-T location.

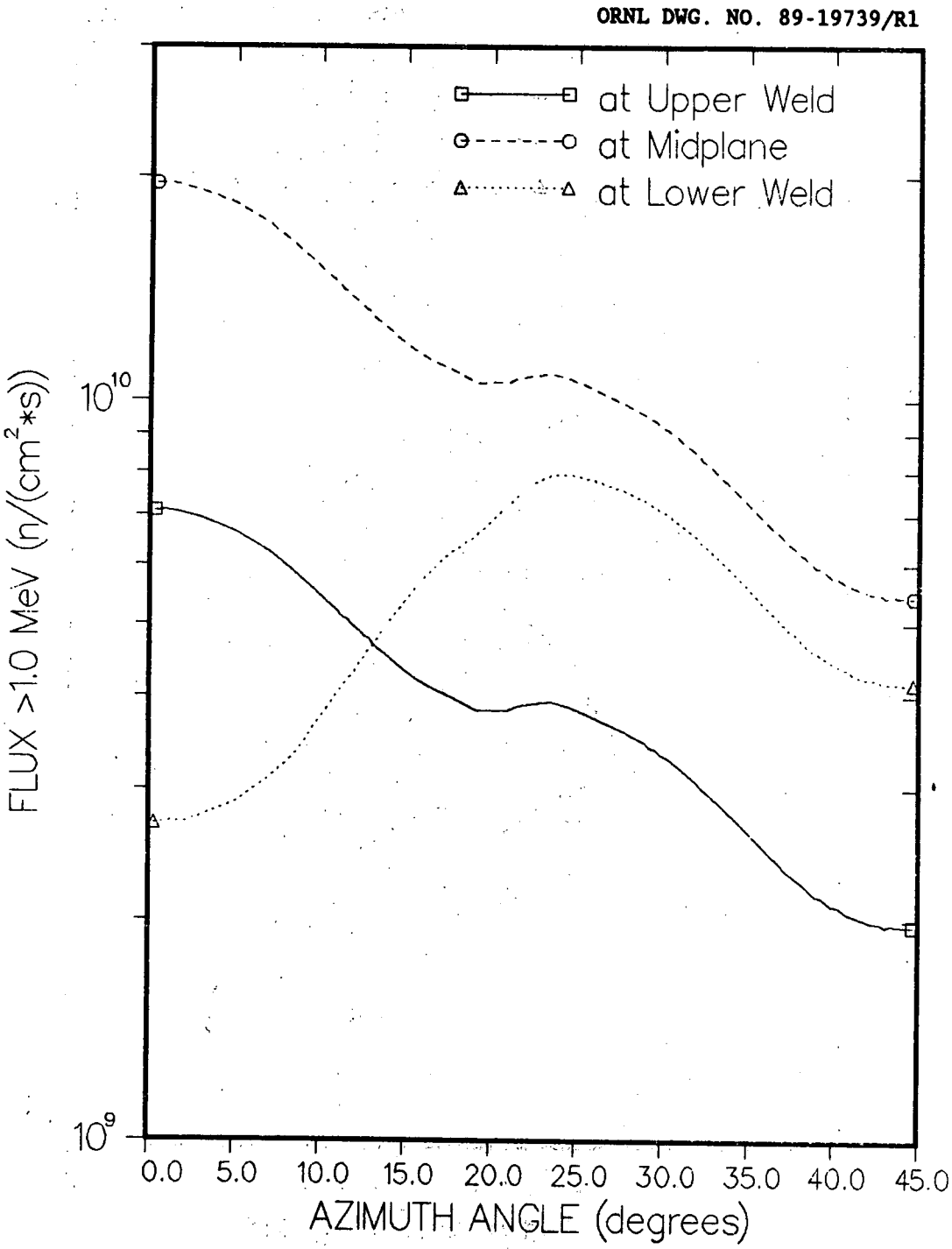

Fig. 4.5. Azimuthal variation in ϕ(>1 MeV) at 1/4-T location.

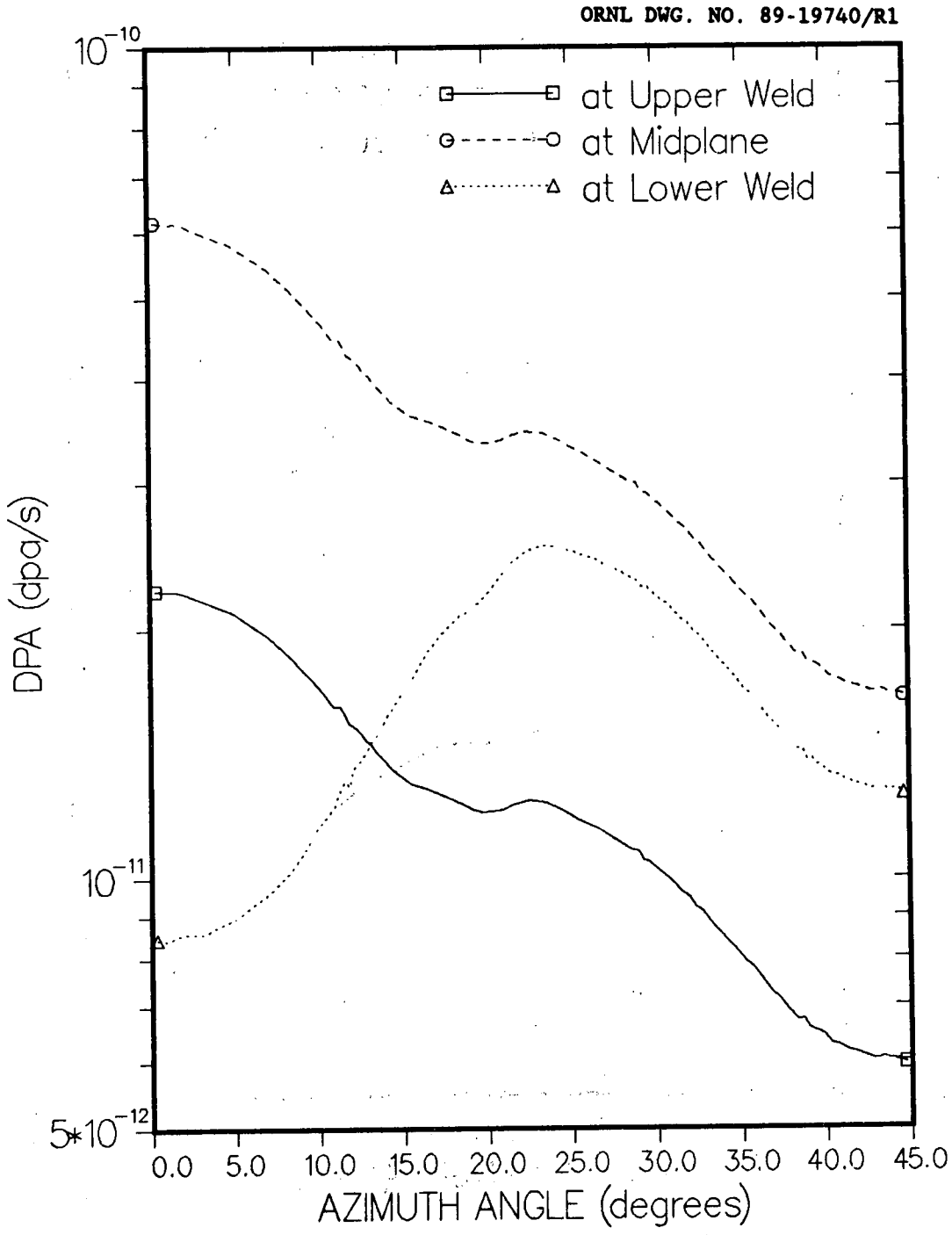

Fig. 4.6. Azimuthal variation in dpa at 0-T location.

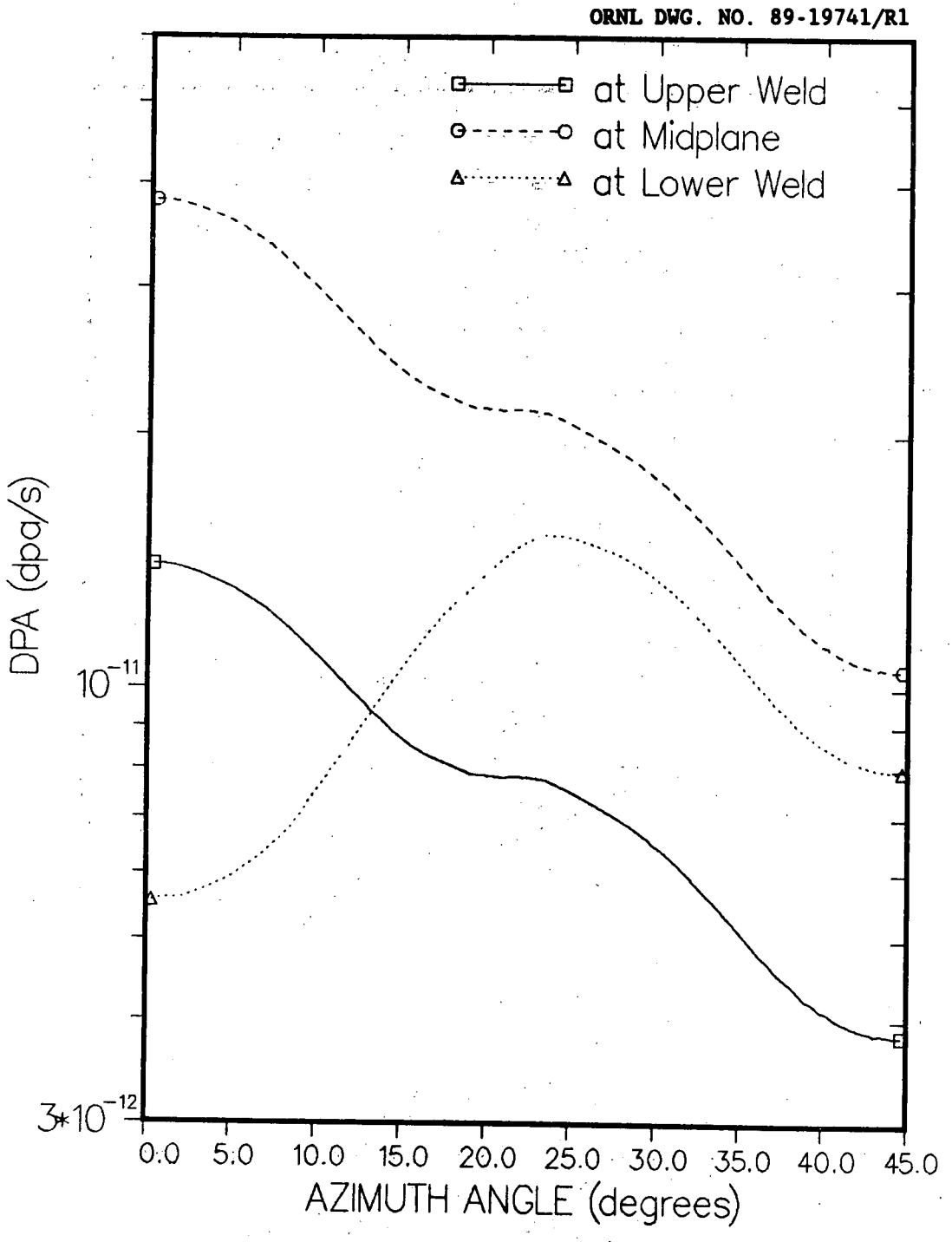

Fig. 4.7. Azimuthal variation in dpa at 1/4-T location.

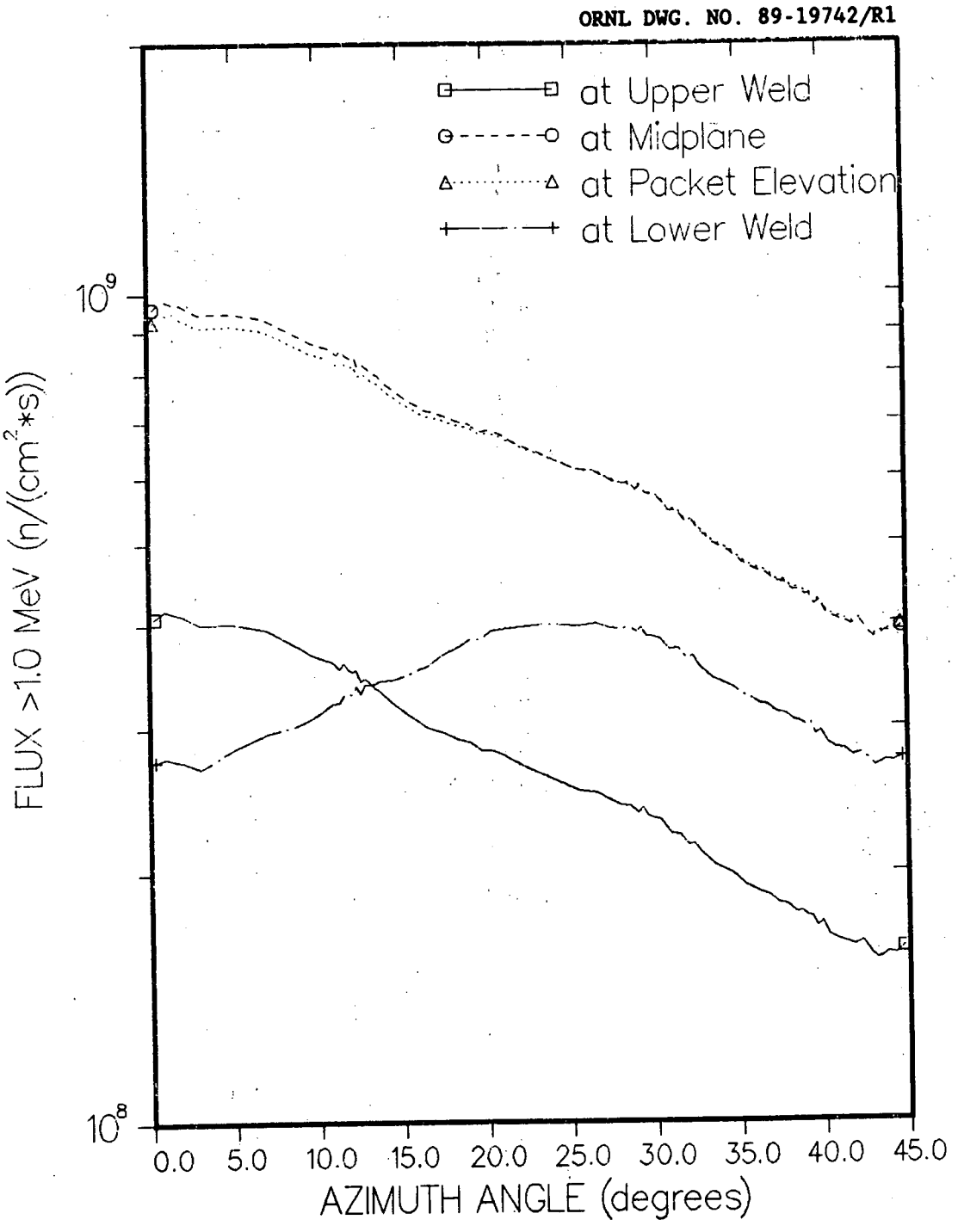

Fig. 4.8. Azimuthal variation in ϕ(>1 MeV) within the cavity.

Table 4.5. Relative azimuthal variation in ϕ(>1 MeV) at 0-T

θ (degree)	$\frac{\phi}{\phi_{max}}$, midplane	$\frac{\phi}{\phi_{max}}$, lower weld
3.1000E-01	1.0000	0.3238
9.0500E-01	0.9965	0.3227
1.5228E+00	0.9979	0.3271
1.9278E+00	0.9947	0.3291
3.0000E+00	0.9719	0.3281
5.0000E+00	0.9372	0.3428
7.0000E+00	0.8778	0.3679
8.4050E+00	0.8254	0.3951
9.0950E+00	0.7954	0.4146
9.6900E+00	0.7726	0.4376
1.0310E+01	0.7463	0.4586
1.0905E+01	0.7188	0.4745
1.1315E+01	0.7197	0.5029
1.1565E+01	0.7061	0.5147
1.1815E+01	0.6847	0.5013
1.2065E+01	0.6817	0.5308
1.2315E+01	0.6765	0.5404
1.2565E+01	0.6682	0.5466
1.2815E+01	0.6527	0.5560
1.3100E+01	0.6489	0.5726
1.3415E+01	0.6352	0.5827
1.3730E+01	0.6249	0.5969
1.4445E+01	0.6015	0.6321
1.5500E+01	0.5806	0.6808
1.6500E+01	0.5711	0.7366
1.7500E+01	0.5592	0.7754
1.8405E+01	0.5429	0.7990
1.9095E+01	0.5294	0.8056
1.9690E+01	0.5224	0.8252
2.0310E+01	0.5249	0.8546
2.0905E+01	0.5302	0.8938
2.1595E+01	0.5450	0.9385
2.2500E+01	0.5566	0.9793
2.3500E+01	0.5575	1.0000
2.4500E+01	0.5472	0.9944
2.5500E+01	0.5333	0.9785
2.6550E+01	0.5195	0.9617
2.7375E+01	0.5056	0.9368
2.7925E+01	0.4990	0.9318
2.8505E+01	0.4902	0.9153
2.8955E+01	0.4891	0.9052

Table 4.5. (continued)

θ (degree)	$\frac{\phi}{\phi_{max}}$, midplane	$\frac{\phi}{\phi_{max}}$, lower weld
2.9240E+01	0.4749	0.8895
2.9535E+01	0.4732	0.8921
2.9845E+01	0.4696	0.8770
3.0310E+01	0.4604	0.8599
3.0905E+01	0.4486	0.8447
3.1440E+01	0.4375	0.8175
3.1940E+01	0.4302	0.8067
3.2315E+01	0.4188	0.7876
3.2720E+01	0.4127	0.7739
3.3500E+01	0.3930	0.7368
3.4500E+01	0.3737	0.7001
3.5250E+01	0.3587	0.6683
3.5750E+01	0.3519	0.6578
3.6250E+01	0.3406	0.6345
3.6750E+01	0.3291	0.6128
3.7250E+01	0.3222	0.6012
3.7750E+01	0.3122	0.5812
3.8250E+01	0.3035	0.5634
3.8655E+01	0.3044	0.5672
3.8955E+01	0.2962	0.5468
3.9240E+01	0.2939	0.5499
3.9535E+01	0.2948	0.5423
3.9845E+01	0.2910	0.5371
4.0250E+01	0.2837	0.5274
4.0750E+01	0.2826	0.5258
Z.1250E+01	0.2788	0.5175
4.1750E+01	0.2771	0.5148
4.2250E+01	0.2751	0.5116
4.2750E+01	0.2727	0.5063
4.3073E+01	0.2735	0.5077
4.3323E+01	0.2743	0.5118
4.3750E+01	0.2731	0.5053
4.4200E+01	0.2723	0.5077
4.4700E+01	0.2700	0.5013

Table 4.6. Relative radial variation in ϕ(>1 MeV) and dpa through RPV at peak location

Radius	$\frac{\phi}{\phi_{max}}$	$\frac{dpa}{dpa_{max}}$
197.490	1.0000	1.0000
198.050 (0-T)	0.9712	0.9754
200.780	0.7484	0.7985
202.600	0.5970	0.6803
203.960 (1/4-T)	0.5012	0.6026
204.420	0.4689	0.5764
206.230	0.3676	0.4893
208.050	0.2864	0.4146
209.900	0.2210	0.3491
211.690	0.1715	0.2949
213.510	0.1320	0.2464
215.330	0.1009	0.2035
215.780 (3/4-T)	0.0985	0.1941
217.140	0.0767	0.1656
218.960	0.0569	0.1296
220.780	0.0403	0.0952
221.690	0.0354	0.0850

Table 4.7. Integral flux and dpa results obtained from reference calculations (no adjustments)

Location	ϕ(E > 1 MeV)	ϕ(E > 0.11 MeV)	dpa
3° dosimetry position	9.12E+8	1.07E+10	3.57E-12
9° dosimetry position	8.59E+8	1.10E+10	3.65E-12
27° dosimetry position	5.97E+8	7.76E+9	2.58E-12
0-T midplane (0°)[a]	3.79E+10	1.04E+11	6.18E-11
1/4-T midplane (0°)[a]	1.96E+10	8.44E+11	3.82E-11
0-T lower weld (24°)[a]	1.57E+10	4.07E+10	2.52E-11
1/4-T lower weld (24°)[a]	7.95E+9	3.27E+10	1.52E-11

[a]At peak azimuthal location.

Table 4.8. Flux and dpa spectra at 0-T of midplane (θ = 0°)

Group	Energy (MeV)	Group flux ($n/cm^2 \cdot s$)	Cumulative flux ($n/cm^2 \cdot s$)	Group dpa rate ($dpa \cdot s^{-1}$)	Cumulative dpa rate ($dpa \cdot s^{-1}$)	dpa fraction
1	1.733E+01	6.890E+06	6.890E+06	2.013E-14	2.013E-14	3.260E-04
2	1.419E+01	3.002E+07	3.691E+07	7.943E-14	9.956E-14	1.612E-03
3	1.221E+01	1.247E+08	1.617E+08	3.005E-13	4.001E-13	6.479E-03
4	1.000E+01	2.604E+08	4.220E+08	5.777E-13	9.778E-13	1.583E-02
5	8.607E+00	4.733E+08	8.953E+08	9.877E-13	1.966E-12	3.183E-02
6	7.408E+00	1.148E+09	2.043E+09	2.230E-12	4.195E-12	6.794E-02
7	6.065E+00	1.684E+09	3.727E+09	3.004E-12	7.199E-12	1.166E-01
8	4.966E+00	3.128E+09	6.855E+09	4.914E-12	1.211E-11	1.962E-01
9	3.679E+00	2.305E+09	9.160E+09	3.158E-12	1.527E-11	2.473E-01
10	3.012E+00	1.743E+09	1.090E+10	2.216E-12	1.749E-11	2.832E-01
11	2.725E+00	2.044E+09	1.295E+10	2.606E-12	2.009E-11	3.254E-01
12	2.466E+00	1.054E+09	1.400E+10	1.235E-12	2.133E-11	3.454E-01
13	2.365E+00	2.886E+08	1.429E+10	3.163E-13	2.164E-11	3.505E-01
14	2.346E+00	1.381E+09	1.567E+10	1.438E-12	2.308E-11	3.738E-01
15	2.231E+00	3.568E+09	1.924E+10	3.690E-12	2.677E-11	4.336E-01
16	1.920E+00	3.934E+09	2.317E+10	3.200E-12	2.997E-11	4.854E-01
17	1.653E+00	5.561E+09	2.873E+10	4.506E-12	3.448E-11	5.583E-01
18	1.353E+00	9.149E+09	3.788E+10	5.126E-12	3.960E-11	6.414E-01
19	1.003E+00	6.067E+09	4.395E+10	2.224E-12	4.183E-11	6.774E-01
20	8.208E-01	3.261E+09	4.721E+10	1.829E-12	4.366E-11	7.070E-01
21	7.427E-01	9.205E+09	5.642E+10	3.327E-12	4.698E-11	7.609E-01
22	6.081E-01	7.583E+09	6.400E+10	2.232E-12	4.922E-11	7.970E-01
23	4.979E-01	8.815E+09	7.282E+10	3.494E-12	5.271E-11	8.536E-01
24	3.688E-01	8.863E+09	8.168E+10	1.832E-12	5.454E-11	8.833E-01
25	2.972E-01	1.150E+10	9.318E+10	2.306E-12	5.685E-11	9.206E-01
26	1.832E-01	1.075E+10	1.039E+11	1.516E-12	5.836E-11	9.452E-01
27	1.111E-01	7.700E+09	1.116E+11	9.956E-13	5.936E-11	9.613E-01
28	6.738E-02	6.580E+09	1.182E+11	4.262E-13	5.979E-11	9.682E-01
29	4.087E-02	2.499E+09	1.207E+11	2.022E-13	5.999E-11	9.715E-01
30	3.183E-02	1.534E+09	1.222E+11	4.361E-13	6.042E-11	9.785E-01
31	2.606E-02	2.957E+09	1.252E+11	5.961E-14	6.048E-11	9.795E-01
32	2.418E-02	1.661E+09	1.269E+11	7.271E-15	6.049E-11	9.796E-01
33	2.188E-02	3.711E+09	1.306E+11	3.039E-14	6.052E-11	9.801E-01
34	1.503E-02	6.969E+09	1.375E+11	1.307E-13	6.065E-11	9.822E-01
35	7.102E-03	7.917E+09	1.455E+11	7.042E-14	6.072E-11	9.833E-01
36	3.355E-03	7.473E+09	1.529E+11	2.631E-14	6.075E-11	9.838E-01
37	1.585E-03	1.294E+10	1.659E+11	2.177E-14	6.077E-11	9.841E-01
38	4.540E-04	7.378E+09	1.733E+11	7.273E-16	6.077E-11	9.841E-01
39	2.144E-04	8.105E+09	1.814E+11	1.162E-15	6.077E-11	9.842E-01
40	1.013E-04	1.108E+10	1.924E+11	2.471E-15	6.077E-11	9.842E-01
41	3.727E-05	1.401E+10	2.064E+11	5.517E-15	6.078E-11	9.843E-01
42	1.068E-05	8.268E+09	2.147E+11	5.314E-15	6.079E-11	9.844E-01
43	5.043E-06	1.067E+10	2.254E+11	1.067E-14	6.080E-11	9.845E-01
44	1.855E-06	7.543E+09	2.329E+11	1.159E-14	6.081E-11	9.847E-01
45	8.764E-07	7.048E+09	2.400E+11	1.582E-14	6.082E-11	9.850E-01
46	4.140E-07	1.899E+10	2.590E+11	7.793E-14	6.090E-11	9.862E-01
47	1.000E-07	8.349E+10	3.425E+11	8.491E-13	6.175E-11	1.000E+00

Table 4.9. Flux and dpa spectra at 1/4-T of midplane (θ = 0°)

Group	Energy (MeV)	Group flux ($n/cm^2 \cdot s$)	Cumulative flux ($n/cm^2 \cdot s$)	Group dpa rate ($dpa \cdot s^{-1}$)	Cumulative dpa rate ($dpa \cdot s^{-1}$)	dpa fraction
1	1.733E+01	2.805E+06	2.805E+06	8.196E-15	8.196E-15	2.147E-04
2	1.419E+01	1.222E+07	1.502E+07	3.232E-14	4.052E-14	1.062E-03
3	1.221E+01	4.865E+07	6.367E+07	1.172E-13	1.577E-13	4.132E-03
4	1.000E+01	1.020E+08	1.657E+08	2.264E-13	3.841E-13	1.006E-02
5	8.607E+00	1.818E+08	3.475E+08	3.795E-13	7.636E-13	2.000E-02
6	7.408E+00	4.239E+08	7.714E+08	8.236E-13	1.587E-12	4.158E-02
7	6.065E+00	6.089E+08	1.380E+09	1.086E-12	2.673E-12	7.003E-02
8	4.966E+00	1.119E+09	2.499E+09	1.757E-12	4.431E-12	1.161E-01
9	3.679E+00	8.469E+08	3.346E+09	1.160E-12	5.591E-12	1.465E-01
10	3.012E+00	6.716E+08	4.017E+09	8.536E-13	6.445E-12	1.688E-01
11	2.725E+00	8.344E+08	4.852E+09	1.064E-12	7.508E-12	1.967E-01
12	2.466E+00	4.409E+08	5.293E+09	5.167E-13	8.025E-12	2.102E-01
13	2.365E+00	1.286E+08	5.421E+09	1.409E-13	8.166E-12	2.139E-01
14	2.346E+00	6.372E+08	6.058E+09	6.633E-13	8.829E-12	2.313E-01
15	2.231E+00	1.733E+09	7.791E+09	1.792E-12	1.062E-11	2.782E-01
16	1.920E+00	2.127E+09	9.918E+09	1.730E-12	1.235E-11	3.236E-01
17	1.653E+00	3.209E+09	1.313E+10	2.600E-12	1.495E-11	3.917E-01
18	1.353E+00	6.438E+09	1.956E+10	3.607E-12	1.856E-11	4.862E-01
19	1.003E+00	4.776E+09	2.434E+10	1.750E-12	2.031E-11	5.320E-01
20	8.208E-01	2.261E+09	2.660E+10	1.268E-12	2.158E-11	5.652E-01
21	7.427E-01	9.092E+09	3.569E+10	3.286E-12	2.486E-11	6.513E-01
22	6.081E-01	7.281E+09	4.297E+10	2.143E-12	2.701E-11	7.075E-01
23	4.979E-01	9.029E+09	5.200E+10	3.579E-12	3.058E-11	8.012E-01
24	3.688E-01	1.062E+10	6.262E+10	2.195E-12	3.278E-11	8.587E-01
25	2.972E-01	1.081E+10	7.343E+10	2.168E-12	3.495E-11	9.155E-01
26	1.832E-01	1.098E+10	8.442E+10	1.548E-12	3.650E-11	9.561E-01
27	1.111E-01	6.543E+09	9.096E+10	8.460E-13	3.734E-11	9.782E-01
28	6.738E-02	5.154E+09	9.611E+10	3.338E-13	3.768E-11	9.870E-01
29	4.087E-02	1.329E+09	9.744E+10	1.075E-13	3.778E-11	9.898E-01
30	3.183E-02	4.625E+08	9.790E+10	1.315E-13	3.791E-11	9.932E-01
31	2.606E-02	3.241E+09	1.011E+11	6.534E-14	3.798E-11	9.949E-01
32	2.418E-02	1.774E+09	1.029E+11	7.770E-15	3.799E-11	9.952E-01
33	2.188E-02	2.881E+09	1.058E+11	2.359E-14	3.801E-11	9.958E-01
34	1.503E-02	3.420E+09	1.092E+11	6.416E-14	3.808E-11	9.974E-01
35	7.102E-03	4.835E+09	1.141E+11	4.300E-14	3.812E-11	9.986E-01
36	3.355E-03	3.618E+09	1.177E+11	1.273E-14	3.813E-11	9.989E-01
37	1.585E-03	6.447E+09	1.241E+11	1.084E-14	3.814E-11	9.992E-01
38	4.540E-04	2.809E+09	1.269E+11	2.770E-16	3.814E-11	9.992E-01
39	2.144E-04	3.524E+09	1.305E+11	5.054E-16	3.814E-11	9.992E-01
40	1.013E-04	5.064E+09	1.355E+11	1.130E-15	3.814E-11	9.992E-01
41	3.727E-05	6.249E+09	1.418E+11	2.461E-15	3.815E-11	9.993E-01
42	1.068E-05	3.321E+09	1.451E+11	2.135E-15	3.815E-11	9.994E-01
43	5.043E-06	3.589E+09	1.487E+11	3.589E-15	3.815E-11	9.995E-01
44	1.855E-06	1.933E+09	1.506E+11	2.971E-15	3.815E-11	9.995E-01
45	8.764E-07	1.281E+09	1.519E+11	2.875E-15	3.816E-11	9.996E-01
46	4.140E-07	9.049E+08	1.528E+11	3.713E-15	3.816E-11	9.997E-01
47	1.000E-07	1.106E+09	1.539E+11	1.124E-14	3.817E-11	1.000E+00

Table 4.10. Flux and dpa spectra at 3/4-T of midplane (θ = 0°)

Group	Energy (MeV)	Group flux ($n/cm^2 \cdot s$)	Cumulative flux ($n/cm^2 \cdot s$)	Group dpa rate ($dpa \cdot s^{-1}$)	Cumulative dpa rate ($dpa \cdot s^{-1}$)	dpa fraction
1	1.733E+01	4.632E+05	4.632E+05	1.354E-15	1.354E-15	1.101E-04
2	1.419E+01	1.949E+06	2.412E+06	5.157E-15	6.511E-15	5.295E-04
3	1.221E+01	7.069E+06	9.482E+06	1.703E-14	2.354E-14	1.915E-03
4	1.000E+01	1.439E+07	2.387E+07	3.193E-14	5.547E-14	4.511E-03
5	8.607E+00	2.399E+07	4.786E+07	5.006E-14	1.055E-13	8.582E-03
6	7.408E+00	5.057E+07	9.843E+07	9.827E-14	2.038E-13	1.657E-02
7	6.065E+00	6.888E+07	1.673E+08	1.229E-13	3.267E-13	2.657E-02
8	4.966E+00	1.224E+08	2.897E+08	1.922E-13	5.189E-13	4.220E-02
9	3.679E+00	9.720E+07	3.869E+08	1.332E-13	6.521E-13	5.303E-02
10	3.012E+00	7.888E+07	4.657E+08	1.003E-13	7.523E-13	6.118E-02
11	2.725E+00	1.028E+08	5.685E+08	1.310E-13	8.833E-13	7.184E-02
12	2.466E+00	5.611E+07	6.246E+08	6.576E-14	9.491E-13	7.719E-02
13	2.365E+00	1.803E+07	6.426E+08	1.976E-14	9.689E-13	7.879E-02
14	2.346E+00	9.254E+07	7.352E+08	9.633E-14	1.065E-12	8.663E-02
15	2.231E+00	2.634E+08	9.986E+08	2.724E-13	1.338E-12	1.088E-01
16	1.920E+00	3.817E+08	1.380E+09	3.105E-13	1.648E-12	1.340E-01
17	1.653E+00	6.266E+08	2.007E+09	5.077E-13	2.156E-12	1.753E-01
18	1.353E+00	1.696E+09	3.703E+09	9.501E-13	3.106E-12	2.526E-01
19	1.003E+00	1.569E+09	5.272E+09	5.750E-13	3.681E-12	2.994E-01
20	8.208E-01	6.774E+08	5.949E+09	3.800E-13	4.061E-12	3.303E-01
21	7.427E-01	3.903E+09	9.852E+09	1.411E-12	5.471E-12	4.450E-01
22	6.081E-01	3.307E+09	1.316E+10	9.732E-13	6.445E-12	5.241E-01
23	4.979E-01	4.312E+09	1.747E+10	1.709E-12	8.154E-12	6.632E-01
24	3.688E-01	6.322E+09	2.379E+10	1.307E-12	9.461E-12	7.694E-01
25	2.972E-01	5.690E+09	2.948E+10	1.141E-12	1.060E-11	8.622E-01
26	1.832E-01	6.288E+09	3.577E+10	8.866E-13	1.149E-11	9.343E-01
27	1.111E-01	3.367E+09	3.914E+10	4.353E-13	1.192E-11	9.697E-01
28	6.738E-02	2.434E+09	4.157E+10	1.576E-13	1.208E-11	9.826E-01
29	4.087E-02	5.986E+08	4.217E+10	4.845E-14	1.213E-11	9.865E-01
30	3.183E-02	2.068E+08	4.238E+10	5.878E-14	1.219E-11	9.913E-01
31	2.606E-02	1.908E+09	4.429E+10	3.847E-14	1.223E-11	9.944E-01
32	2.418E-02	1.143E+09	4.543E+10	5.005E-15	1.223E-11	9.948E-01
33	2.188E-02	1.572E+09	4.700E+10	1.288E-14	1.224E-11	9.959E-01
34	1.503E-02	1.343E+09	4.834E+10	2.519E-14	1.227E-11	9.979E-01
35	7.102E-03	1.720E+09	5.006E+10	1.530E-14	1.229E-11	9.992E-01
36	3.355E-03	1.156E+09	5.122E+10	4.067E-15	1.229E-11	9.995E-01
37	1.585E-03	1.803E+09	5.302E+10	3.032E-15	1.229E-11	9.997E-01
38	4.540E-04	7.361E+08	5.376E+10	7.256E-17	1.229E-11	9.997E-01
39	2.144E-04	8.331E+08	5.459E+10	1.195E-16	1.229E-11	9.997E-01
40	1.013E-04	1.104E+09	5.570E+10	2.462E-16	1.229E-11	9.998E-01
41	3.727E-05	1.272E+09	5.697E+10	5.011E-16	1.229E-11	9.998E-01
42	1.068E-05	6.419E+08	5.761E+10	4.125E-16	1.229E-11	9.998E-01
43	5.043E-06	6.175E+08	5.823E+10	6.175E-16	1.229E-11	9.999E-01
44	1.855E-06	2.905E+08	5.852E+10	4.465E-16	1.229E-11	9.999E-01
45	8.764E-07	1.584E+08	5.868E+10	3.555E-16	1.230E-11	1.000E+00
46	4.140E-07	6.351E+07	5.874E+10	2.606E-16	1.230E-11	1.000E+00
47	1.000E-07	2.742E+07	5.877E+10	2.788E-16	1.230E-11	1.000E+00

Table 4.11. Flux and dpa spectra at 0-T of lower weld (θ = 24°)

Group	Energy (MeV)	Group flux ($n/cm^2 \cdot s$)	Cumulative flux ($n/cm^2 \cdot s$)	Group dpa rate ($dpa \cdot s^{-1}$)	Cumulative dpa rate ($dpa \cdot s^{-1}$)	dpa fraction
1	1.733E+01	3.966E+06	3.966E+06	1.159E-14	1.159E-14	4.599E-04
2	1.419E+01	1.692E+07	2.088E+07	4.477E-14	5.635E-14	2.237E-03
3	1.221E+01	6.750E+07	8.838E+07	1.626E-13	2.190E-13	8.690E-03
4	1.000E+01	1.371E+08	2.255E+08	3.042E-13	5.232E-13	2.076E-02
5	8.607E+00	2.406E+08	4.661E+08	5.022E-13	1.025E-12	4.070E-02
6	7.408E+00	5.663E+08	1.032E+09	1.100E-12	2.126E-12	8.437E-02
7	6.065E+00	7.938E+08	1.826E+09	1.416E-12	3.542E-12	1.406E-01
8	4.966E+00	1.391E+09	3.217E+09	2.186E-12	5.727E-12	2.273E-01
9	3.679E+00	9.797E+08	4.197E+09	1.342E-12	7.070E-12	2.806E-01
10	3.012E+00	7.289E+08	4.926E+09	9.265E-13	7.996E-12	3.174E-01
11	2.725E+00	8.417E+08	5.768E+09	1.073E-12	9.069E-12	3.599E-01
12	2.466E+00	4.308E+08	6.198E+09	5.049E-13	9.574E-12	3.800E-01
13	2.365E+00	1.178E+08	6.316E+09	1.291E-13	9.703E-12	3.851E-01
14	2.346E+00	5.608E+08	6.877E+09	5.838E-13	1.029E-11	4.083E-01
15	2.231E+00	1.442E+09	8.319E+09	1.491E-12	1.178E-11	4.674E-01
16	1.920E+00	1.568E+09	9.886E+09	1.275E-12	1.305E-11	5.180E-01
17	1.653E+00	2.194E+09	1.208E+10	1.778E-12	1.483E-11	5.886E-01
18	1.353E+00	3.576E+09	1.566E+10	2.003E-12	1.683E-11	6.681E-01
19	1.003E+00	2.352E+09	1.801E+10	8.620E-13	1.770E-11	7.023E-01
20	8.208E-01	1.257E+09	1.926E+10	7.050E-13	1.840E-11	7.303E-01
21	7.427E-01	3.511E+09	2.278E+10	1.269E-12	1.967E-11	7.807E-01
22	6.081E-01	2.875E+09	2.565E+10	8.461E-13	2.052E-11	8.142E-01
23	4.979E-01	3.340E+09	2.899E+10	1.324E-12	2.184E-11	8.668E-01
24	3.688E-01	3.341E+09	3.233E+10	6.905E-13	2.253E-11	8.942E-01
25	2.972E-01	4.329E+09	3.666E+10	8.679E-13	2.340E-11	9.286E-01
26	1.832E-01	4.042E+09	4.070E+10	5.699E-13	2.397E-11	9.513E-01
27	1.111E-01	2.883E+09	4.359E+10	3.728E-13	2.434E-11	9.661E-01
28	6.738E-02	2.457E+09	4.604E+10	1.591E-13	2.450E-11	9.724E-01
29	4.087E-02	9.314E+08	4.697E+10	7.538E-14	2.458E-11	9.754E-01
30	3.183E-02	5.716E+08	4.755E+10	1.625E-13	2.474E-11	9.818E-01
31	2.606E-02	1.108E+09	4.865E+10	2.233E-14	2.476E-11	9.827E-01
32	2.418E-02	6.205E+08	4.927E+10	2.717E-15	2.476E-11	9.828E-01
33	2.188E-02	1.386E+09	5.066E+10	1.135E-14	2.477E-11	9.833E-01
34	1.503E-02	2.587E+09	5.325E+10	4.853E-14	2.482E-11	9.852E-01
35	7.102E-03	2.932E+09	5.618E+10	2.608E-14	2.485E-11	9.862E-01
36	3.355E-03	2.755E+09	5.893E+10	9.696E-15	2.486E-11	9.866E-01
37	1.585E-03	4.751E+09	6.368E+10	7.991E-15	2.487E-11	9.869E-01
38	4.540E-04	2.680E+09	6.636E+10	2.642E-16	2.487E-11	9.869E-01
39	2.144E-04	2.950E+09	6.931E+10	4.230E-16	2.487E-11	9.869E-01
40	1.013E-04	4.026E+09	7.334E+10	8.981E-16	2.487E-11	9.870E-01
41	3.727E-05	5.072E+09	7.841E+10	1.998E-15	2.487E-11	9.871E-01
42	1.068E-05	2.993E+09	8.140E+10	1.923E-15	2.487E-11	9.871E-01
43	5.043E-06	3.859E+09	8.526E+10	3.859E-15	2.488E-11	9.873E-01
44	1.855E-06	2.727E+09	8.799E+10	4.191E-15	2.488E-11	9.874E-01
45	8.764E-07	2.547E+09	9.054E+10	5.715E-15	2.489E-11	9.877E-01
46	4.140E-07	6.843E+09	9.738E+10	2.808E-14	2.491E-11	9.888E-01
47	1.000E-07	2.777E+10	1.252E+11	2.824E-13	2.520E-11	1.000E+00

Table 4.12. Flux and dpa spectra at 1/4-T of lower weld (θ = 24°)

Group	Energy (MeV)	Group flux ($n/cm^2 \cdot s$)	Cumulative flux ($n/cm^2 \cdot s$)	Group dpa rate ($dpa \cdot s^{-1}$)	Cumulative dpa rate ($dpa \cdot s^{-1}$)	dpa fraction
1	1.733E+01	1.600E+06	1.600E+06	4.674E-15	4.674E-15	3.073E-04
2	1.419E+01	6.816E+06	8.416E+06	1.803E-14	2.271E-14	1.493E-03
3	1.221E+01	2.606E+07	3.447E+07	6.277E-14	8.548E-14	5.619E-03
4	1.000E+01	5.313E+07	8.760E+07	1.179E-13	2.034E-13	1.337E-02
5	8.607E+00	9.141E+07	1.790E+08	1.908E-13	3.941E-13	2.591E-02
6	7.408E+00	2.066E+08	3.856E+08	4.014E-13	7.955E-13	5.229E-02
7	6.065E+00	2.833E+08	6.689E+08	5.054E-13	1.301E-12	8.552E-02
8	4.966E+00	4.908E+08	1.160E+09	7.711E-13	2.072E-12	1.362E-01
9	3.679E+00	3.574E+08	1.517E+09	4.896E-13	2.562E-12	1.684E-01
10	3.012E+00	2.791E+08	1.796E+09	3.548E-13	2.916E-12	1.917E-01
11	2.725E+00	3.414E+08	2.138E+09	4.352E-13	3.352E-12	2.203E-01
12	2.466E+00	1.791E+08	2.317E+09	2.099E-13	3.562E-12	2.341E-01
13	2.365E+00	5.207E+07	2.369E+09	5.707E-14	3.619E-12	2.379E-01
14	2.346E+00	2.567E+08	2.626E+09	2.672E-13	3.886E-12	2.554E-01
15	2.231E+00	6.963E+08	3.322E+09	7.200E-13	4.606E-12	3.028E-01
16	1.920E+00	8.449E+08	4.167E+09	6.872E-13	5.293E-12	3.479E-01
17	1.653E+00	1.265E+09	5.431E+09	1.025E-12	6.318E-12	4.153E-01
18	1.353E+00	2.517E+09	7.948E+09	1.410E-12	7.728E-12	5.080E-01
19	1.003E+00	1.851E+09	9.799E+09	6.785E-13	8.406E-12	5.526E-01
20	8.208E-01	8.754E+08	1.067E+10	4.910E-13	8.897E-12	5.849E-01
21	7.427E-01	3.474E+09	1.415E+10	1.255E-12	1.015E-11	6.674E-01
22	6.081E-01	2.769E+09	1.692E+10	8.150E-13	1.097E-11	7.210E-01
23	4.979E-01	3.437E+09	2.036E+10	1.363E-12	1.233E-11	8.105E-01
24	3.688E-01	4.014E+09	2.437E+10	8.297E-13	1.316E-11	8.651E-01
25	2.972E-01	4.118E+09	2.849E+10	8.256E-13	1.399E-11	9.193E-01
26	1.832E-01	4.186E+09	3.267E+10	5.902E-13	1.458E-11	9.581E-01
27	1.111E-01	2.494E+09	3.517E+10	3.225E-13	1.490E-11	9.793E-01
28	6.738E-02	1.961E+09	3.713E+10	1.270E-13	1.503E-11	9.877E-01
29	4.087E-02	5.057E+08	3.763E+10	4.093E-14	1.507E-11	9.904E-01
30	3.183E-02	1.761E+08	3.781E+10	5.006E-14	1.512E-11	9.936E-01
31	2.606E-02	1.228E+09	3.904E+10	2.475E-14	1.514E-11	9.953E-01
32	2.418E-02	6.709E+08	3.971E+10	2.938E-15	1.514E-11	9.955E-01
33	2.188E-02	1.097E+09	4.081E+10	8.984E-15	1.515E-11	9.961E-01
34	1.503E-02	1.294E+09	4.210E+10	2.427E-14	1.518E-11	9.976E-01
35	7.102E-03	1.819E+09	4.392E+10	1.618E-14	1.519E-11	9.987E-01
36	3.355E-03	1.357E+09	4.527E+10	4.776E-15	1.520E-11	9.990E-01
37	1.585E-03	2.393E+09	4.767E+10	4.025E-15	1.520E-11	9.993E-01
38	4.540E-04	1.048E+09	4.872E+10	1.033E-16	1.520E-11	9.993E-01
39	2.144E-04	1.301E+09	5.002E+10	1.866E-16	1.520E-11	9.993E-01
40	1.013E-04	1.856E+09	5.187E+10	4.141E-16	1.520E-11	9.993E-01
41	3.727E-05	2.272E+09	5.415E+10	8.951E-16	1.520E-11	9.994E-01
42	1.068E-05	1.208E+09	5.535E+10	7.761E-16	1.520E-11	9.994E-01
43	5.043E-06	1.299E+09	5.665E+10	1.299E-15	1.521E-11	9.995E-01
44	1.855E-06	6.995E+08	5.735E+10	1.075E-15	1.521E-11	9.996E-01
45	8.764E-07	4.640E+08	5.782E+10	1.041E-15	1.521E-11	9.997E-01
46	4.140E-07	3.270E+08	5.814E+10	1.342E-15	1.521E-11	9.998E-01
47	1.000E-07	3.691E+08	5.851E+10	3.753E-15	1.521E-11	1.000E+00

Table 4.13. Flux and dpa spectra at 3/4-T of lower weld (θ = 24°)

Group	Energy (MeV)	Group flux ($n/cm^2 \cdot s$)	Cumulative flux ($n/cm^2 \cdot s$)	Group dpa rate ($dpa \cdot s^{-1}$)	Cumulative dpa rate ($dpa \cdot s^{-1}$)	dpa fraction
1	1.733E+01	2.389E+05	2.389E+05	6.980E-16	6.980E-16	1.430E-04
2	1.419E+01	9.975E+05	1.236E+06	2.639E-15	3.337E-15	6.838E-04
3	1.221E+01	3.490E+06	4.726E+06	8.407E-15	1.174E-14	2.406E-03
4	1.000E+01	6.956E+06	1.168E+07	1.543E-14	2.718E-14	5.569E-03
5	8.607E+00	1.129E+07	2.297E+07	2.355E-14	5.073E-14	1.040E-02
6	7.408E+00	2.316E+07	4.613E+07	4.500E-14	9.573E-14	1.962E-02
7	6.065E+00	3.049E+07	7.661E+07	5.439E-14	1.501E-13	3.076E-02
8	4.966E+00	5.199E+07	1.286E+08	8.167E-14	2.318E-13	4.749E-02
9	3.679E+00	4.036E+07	1.690E+08	5.529E-14	2.871E-13	5.882E-02
10	3.012E+00	3.222E+07	2.012E+08	4.095E-14	3.280E-13	6.721E-02
11	2.725E+00	4.152E+07	2.427E+08	5.294E-14	3.810E-13	7.806E-02
12	2.466E+00	2.246E+07	2.652E+08	2.632E-14	4.073E-13	8.345E-02
13	2.365E+00	7.109E+06	2.723E+08	7.792E-15	4.151E-13	8.505E-02
14	2.346E+00	3.655E+07	3.088E+08	3.805E-14	4.531E-13	9.285E-02
15	2.231E+00	1.045E+08	4.133E+08	1.080E-13	5.612E-13	1.150E-01
16	1.920E+00	1.502E+08	5.635E+08	1.222E-13	6.833E-13	1.400E-01
17	1.653E+00	2.457E+08	8.092E+08	1.991E-13	8.824E-13	1.808E-01
18	1.353E+00	6.596E+08	1.469E+09	3.696E-13	1.252E-12	2.565E-01
19	1.003E+00	6.088E+08	2.078E+09	2.231E-13	1.475E-12	3.023E-01
20	8.208E-01	2.663E+08	2.344E+09	1.494E-13	1.624E-12	3.329E-01
21	7.427E-01	1.499E+09	3.843E+09	5.418E-13	2.166E-12	4.439E-01
22	6.081E-01	1.281E+09	5.123E+09	3.769E-13	2.543E-12	5.211E-01
23	4.979E-01	1.677E+09	6.801E+09	6.648E-13	3.208E-12	6.573E-01
24	3.688E-01	2.443E+09	9.244E+09	5.050E-13	3.713E-12	7.608E-01
25	2.972E-01	2.319E+09	1.156E+10	4.650E-13	4.178E-12	8.561E-01
26	1.832E-01	2.573E+09	1.414E+10	3.627E-13	4.541E-12	9.304E-01
27	1.111E-01	1.406E+09	1.554E+10	1.818E-13	4.722E-12	9.676E-01
28	6.738E-02	1.029E+09	1.657E+10	6.666E-14	4.789E-12	9.813E-01
29	4.087E-02	2.551E+08	1.683E+10	2.064E-14	4.810E-12	9.855E-01
30	3.183E-02	8.813E+07	1.691E+10	2.505E-14	4.835E-12	9.907E-01
31	2.606E-02	7.685E+08	1.768E+10	1.549E-14	4.850E-12	9.938E-01
32	2.418E-02	4.543E+08	1.814E+10	1.989E-15	4.852E-12	9.942E-01
33	2.188E-02	6.670E+08	1.880E+10	5.463E-15	4.858E-12	9.954E-01
34	1.503E-02	5.936E+08	1.940E+10	1.114E-14	4.869E-12	9.976E-01
35	7.102E-03	7.646E+08	2.016E+10	6.801E-15	4.876E-12	9.990E-01
36	3.355E-03	5.197E+08	2.068E+10	1.829E-15	4.877E-12	9.994E-01
37	1.585E-03	8.157E+08	2.150E+10	1.372E-15	4.879E-12	9.997E-01
38	4.540E-04	3.324E+08	2.183E+10	3.277E-17	4.879E-12	9.997E-01
39	2.144E-04	3.787E+08	2.221E+10	5.430E-17	4.879E-12	9.997E-01
40	1.013E-04	4.988E+08	2.271E+10	1.113E-16	4.879E-12	9.997E-01
41	3.727E-05	5.668E+08	2.327E+10	2.233E-16	4.879E-12	9.998E-01
42	1.068E-05	2.844E+08	2.356E+10	1.828E-16	4.879E-12	9.998E-01
43	5.043E-06	2.734E+08	2.383E+10	2.734E-16	4.880E-12	9.999E-01
44	1.855E-06	1.294E+08	2.396E+10	1.989E-16	4.880E-12	9.999E-01
45	8.764E-07	7.176E+07	2.403E+10	1.610E-16	4.880E-12	9.999E-01
46	4.140E-07	3.083E+07	2.406E+10	1.265E-16	4.880E-12	1.000E+00
47	1.000E-07	1.406E+07	2.408E+10	1.430E-16	4.880E-12	1.000E+00

Table 4.14. Flux and dpa spectra at 0-T of upper weld (θ = 0°)

Group	Energy (MeV)	Group flux ($n/cm^2 \cdot s$)	Cumulative flux ($n/cm^2 \cdot s$)	Group dpa rate ($dpa \cdot s^{-1}$)	Cumulative dpa rate ($dpa \cdot s^{-1}$)	dpa fraction
1	1.733E+01	2.457E+06	2.457E+06	7.179E-15	7.179E-15	3.215E-04
2	1.419E+01	1.073E+07	1.318E+07	2.838E-14	3.556E-14	1.593E-03
3	1.221E+01	4.460E+07	5.779E+07	1.074E-13	1.430E-13	6.405E-03
4	1.000E+01	9.316E+07	1.509E+08	2.067E-13	3.497E-13	1.566E-02
5	8.607E+00	1.695E+08	3.205E+08	3.538E-13	7.035E-13	3.151E-02
6	7.408E+00	4.109E+08	7.314E+08	7.984E-13	1.502E-12	6.726E-02
7	6.065E+00	6.025E+08	1.334E+09	1.075E-12	2.577E-12	1.154E-01
8	4.966E+00	1.122E+09	2.456E+09	1.763E-12	4.340E-12	1.944E-01
9	3.679E+00	8.270E+08	3.283E+09	1.133E-12	5.473E-12	2.451E-01
10	3.012E+00	6.262E+08	3.909E+09	7.959E-13	6.269E-12	2.807E-01
11	2.725E+00	7.345E+08	4.644E+09	9.365E-13	7.205E-12	3.227E-01
12	2.466E+00	3.786E+08	5.023E+09	4.437E-13	7.649E-12	3.426E-01
13	2.365E+00	1.036E+08	5.126E+09	1.136E-13	7.763E-12	3.476E-01
14	2.346E+00	4.964E+08	5.622E+09	5.167E-13	8.279E-12	3.708E-01
15	2.231E+00	1.284E+09	6.906E+09	1.328E-12	9.607E-12	4.302E-01
16	1.920E+00	1.415E+09	8.322E+09	1.151E-12	1.076E-11	4.818E-01
17	1.653E+00	2.002E+09	1.032E+10	1.622E-12	1.238E-11	5.545E-01
18	1.353E+00	3.302E+09	1.363E+10	1.850E-12	1.423E-11	6.373E-01
19	1.003E+00	2.195E+09	1.582E+10	8.044E-13	1.503E-11	6.733E-01
20	8.208E-01	1.180E+09	1.700E+10	6.617E-13	1.570E-11	7.030E-01
21	7.427E-01	3.351E+09	2.035E+10	1.211E-12	1.691E-11	7.572E-01
22	6.081E-01	2.765E+09	2.312E+10	8.138E-13	1.772E-11	7.936E-01
23	4.979E-01	3.221E+09	2.634E+10	1.277E-12	1.900E-11	8.508E-01
24	3.688E-01	3.275E+09	2.961E+10	6.770E-13	1.967E-11	8.811E-01
25	2.972E-01	4.232E+09	3.384E+10	8.486E-13	2.052E-11	9.191E-01
26	1.832E-01	3.988E+09	3.783E+10	5.624E-13	2.109E-11	9.443E-01
27	1.111E-01	2.840E+09	4.067E+10	3.672E-13	2.145E-11	9.608E-01
28	6.738E-02	2.421E+09	4.309E+10	1.568E-13	2.161E-11	9.678E-01
29	4.087E-02	9.160E+08	4.401E+10	7.413E-14	2.168E-11	9.711E-01
30	3.183E-02	5.613E+08	4.457E+10	1.596E-13	2.184E-11	9.783E-01
31	2.606E-02	1.112E+09	4.568E+10	2.241E-14	2.187E-11	9.793E-01
32	2.418E-02	6.291E+08	4.631E+10	2.755E-15	2.187E-11	9.794E-01
33	2.188E-02	1.383E+09	4.770E+10	1.133E-14	2.188E-11	9.799E-01
34	1.503E-02	2.564E+09	5.026E+10	4.811E-14	2.193E-11	9.821E-01
35	7.102E-03	2.913E+09	5.317E+10	2.591E-14	2.195E-11	9.832E-01
36	3.355E-03	2.744E+09	5.592E+10	9.658E-15	2.196E-11	9.836E-01
37	1.585E-03	4.746E+09	6.066E+10	7.983E-15	2.197E-11	9.840E-01
38	4.540E-04	2.703E+09	6.337E+10	2.664E-16	2.197E-11	9.840E-01
39	2.144E-04	2.968E+09	6.633E+10	4.256E-16	2.197E-11	9.840E-01
40	1.013E-04	4.055E+09	7.039E+10	9.046E-16	2.197E-11	9.841E-01
41	3.727E-05	5.124E+09	7.551E+10	2.018E-15	2.198E-11	9.842E-01
42	1.068E-05	3.024E+09	7.854E+10	1.943E-15	2.198E-11	9.842E-01
43	5.043E-06	3.900E+09	8.244E+10	3.900E-15	2.198E-11	9.844E-01
44	1.855E-06	2.754E+09	8.519E+10	4.234E-15	2.199E-11	9.846E-01
45	8.764E-07	2.573E+09	8.776E+10	5.774E-15	2.199E-11	9.849E-01
46	4.140E-07	6.927E+09	9.469E+10	2.842E-14	2.202E-11	9.861E-01
47	1.000E-07	3.042E+10	1.251E+11	3.094E-13	2.233E-11	1.000E+00

Table 4.15. Flux and dpa spectra at 1/4-T of upper weld (θ = 0°)

Group	Energy (MeV)	Group flux ($n/cm^2 \cdot s$)	Cumulative flux ($n/cm^2 \cdot s$)	Group dpa rate ($dpa \cdot s^{-1}$)	Cumulative dpa rate ($dpa \cdot s^{-1}$)	dpa fraction
1	1.733E+01	1.005E+06	1.005E+06	2.935E-15	2.935E-15	2.097E-04
2	1.419E+01	4.387E+06	5.391E+06	1.161E-14	1.454E-14	1.039E-03
3	1.221E+01	1.747E+07	2.286E+07	4.208E-14	5.663E-14	4.046E-03
4	1.000E+01	3.667E+07	5.953E+07	8.137E-14	1.380E-13	9.860E-03
5	8.607E+00	6.542E+07	1.250E+08	1.365E-13	2.745E-13	1.962E-02
6	7.408E+00	1.525E+08	2.774E+08	2.963E-13	5.708E-13	4.079E-02
7	6.065E+00	2.194E+08	4.968E+08	3.914E-13	9.622E-13	6.875E-02
8	4.966E+00	4.041E+08	9.009E+08	6.348E-13	1.597E-12	1.141E-01
9	3.679E+00	3.063E+08	1.207E+09	4.197E-13	2.017E-12	1.441E-01
10	3.012E+00	2.428E+08	1.450E+09	3.087E-13	2.325E-12	1.662E-01
11	2.725E+00	3.019E+08	1.752E+09	3.849E-13	2.710E-12	1.937E-01
12	2.466E+00	1.595E+08	1.911E+09	1.870E-13	2.897E-12	2.070E-01
13	2.365E+00	4.646E+07	1.958E+09	5.092E-14	2.948E-12	2.107E-01
14	2.346E+00	2.306E+08	2.189E+09	2.400E-13	3.188E-12	2.278E-01
15	2.231E+00	6.280E+08	2.817E+09	6.494E-13	3.838E-12	2.742E-01
16	1.920E+00	7.717E+08	3.588E+09	6.276E-13	4.465E-12	3.190E-01
17	1.653E+00	1.165E+09	4.753E+09	9.441E-13	5.409E-12	3.865E-01
18	1.353E+00	2.343E+09	7.097E+09	1.313E-12	6.722E-12	4.803E-01
19	1.003E+00	1.743E+09	8.839E+09	6.388E-13	7.361E-12	5.260E-01
20	8.208E-01	8.243E+08	9.664E+09	4.624E-13	7.823E-12	5.590E-01
21	7.427E-01	3.338E+09	1.300E+10	1.206E-12	9.030E-12	6.452E-01
22	6.081E-01	2.681E+09	1.568E+10	7.891E-13	9.819E-12	7.016E-01
23	4.979E-01	3.334E+09	1.902E+10	1.322E-12	1.114E-11	7.960E-01
24	3.688E-01	3.975E+09	2.299E+10	8.217E-13	1.196E-11	8.547E-01
25	2.972E-01	4.052E+09	2.704E+10	8.125E-13	1.277E-11	9.128E-01
26	1.832E-01	4.163E+09	3.121E+10	5.869E-13	1.336E-11	9.547E-01
27	1.111E-01	2.474E+09	3.368E+10	3.199E-13	1.368E-11	9.776E-01
28	6.738E-02	1.945E+09	3.563E+10	1.259E-13	1.381E-11	9.866E-01
29	4.087E-02	5.005E+08	3.613E+10	4.050E-14	1.385E-11	9.895E-01
30	3.183E-02	1.742E+08	3.630E+10	4.952E-14	1.390E-11	9.930E-01
31	2.606E-02	1.241E+09	3.754E+10	2.503E-14	1.392E-11	9.948E-01
32	2.418E-02	6.868E+08	3.823E+10	3.007E-15	1.393E-11	9.950E-01
33	2.188E-02	1.108E+09	3.934E+10	9.076E-15	1.393E-11	9.957E-01
34	1.503E-02	1.294E+09	4.063E+10	2.427E-14	1.396E-11	9.974E-01
35	7.102E-03	1.822E+09	4.245E+10	1.621E-14	1.397E-11	9.986E-01
36	3.355E-03	1.358E+09	4.381E+10	4.781E-15	1.398E-11	9.989E-01
37	1.585E-03	2.410E+09	4.622E+10	4.053E-15	1.398E-11	9.992E-01
38	4.540E-04	1.048E+09	4.727E+10	1.033E-16	1.398E-11	9.992E-01
39	2.144E-04	1.311E+09	4.858E+10	1.880E-16	1.398E-11	9.992E-01
40	1.013E-04	1.879E+09	5.046E+10	4.193E-16	1.398E-11	9.992E-01
41	3.727E-05	2.314E+09	5.277E+10	9.114E-16	1.399E-11	9.993E-01
42	1.068E-05	1.228E+09	5.400E+10	7.892E-16	1.399E-11	9.994E-01
43	5.043E-06	1.324E+09	5.532E+10	1.324E-15	1.399E-11	9.995E-01
44	1.855E-06	7.115E+08	5.604E+10	1.094E-15	1.399E-11	9.995E-01
45	8.764E-07	4.707E+08	5.651E+10	1.056E-15	1.399E-11	9.996E-01
46	4.140E-07	3.311E+08	5.684E+10	1.359E-15	1.399E-11	9.997E-01
47	1.000E-07	4.036E+08	5.724E+10	4.104E-15	1.400E-11	1.000E+00

Table 4.16. Flux and dpa spectra at 3/4-T of upper weld (θ = 0°)

Group	Energy (MeV)	Group flux ($n/cm^2 \cdot s$)	Cumulative flux ($n/cm^2 \cdot s$)	Group dpa rate ($dpa \cdot s^{-1}$)	Cumulative dpa rate ($dpa \cdot s^{-1}$)	dpa fraction
1	1.733E+01	1.671E+05	1.671E+05	4.883E-16	4.883E-16	1.035E-04
2	1.419E+01	7.043E+05	8.714E+05	1.864E-15	2.352E-15	4.985E-04
3	1.221E+01	2.554E+06	3.425E+06	6.152E-15	8.504E-15	1.802E-03
4	1.000E+01	5.205E+06	8.630E+06	1.155E-14	2.005E-14	4.250E-03
5	8.607E+00	8.690E+06	1.732E+07	1.814E-14	3.819E-14	8.094E-03
6	7.408E+00	1.831E+07	3.563E+07	3.557E-14	7.376E-14	1.563E-02
7	6.065E+00	2.495E+07	6.058E+07	4.451E-14	1.183E-13	2.507E-02
8	4.966E+00	4.473E+07	1.053E+08	7.027E-14	1.885E-13	3.996E-02
9	3.679E+00	3.560E+07	1.409E+08	4.877E-14	2.373E-13	5.030E-02
10	3.012E+00	2.889E+07	1.698E+08	3.671E-14	2.740E-13	5.808E-02
11	2.725E+00	3.767E+07	2.075E+08	4.803E-14	3.221E-13	6.826E-02
12	2.466E+00	2.056E+07	2.280E+08	2.409E-14	3.462E-13	7.336E-02
13	2.365E+00	6.592E+06	2.346E+08	7.225E-15	3.534E-13	7.489E-02
14	2.346E+00	3.387E+07	2.685E+08	3.525E-14	3.886E-13	8.237E-02
15	2.231E+00	9.650E+07	3.650E+08	9.978E-14	4.884E-13	1.035E-01
16	1.920E+00	1.400E+08	5.050E+08	1.139E-13	6.023E-13	1.277E-01
17	1.653E+00	2.302E+08	7.352E+08	1.865E-13	7.888E-13	1.672E-01
18	1.353E+00	6.261E+08	1.361E+09	3.508E-13	1.140E-12	2.415E-01
19	1.003E+00	5.839E+08	1.945E+09	2.140E-13	1.354E-12	2.869E-01
20	8.208E-01	2.534E+08	2.199E+09	1.421E-13	1.496E-12	3.170E-01
21	7.427E-01	1.475E+09	3.673E+09	5.330E-13	2.029E-12	4.300E-01
22	6.081E-01	1.264E+09	4.938E+09	3.721E-13	2.401E-12	5.088E-01
23	4.979E-01	1.661E+09	6.599E+09	6.585E-13	3.059E-12	6.484E-01
24	3.688E-01	2.470E+09	9.069E+09	5.105E-13	3.570E-12	7.566E-01
25	2.972E-01	2.276E+09	1.134E+10	4.564E-13	4.026E-12	8.533E-01
26	1.832E-01	2.553E+09	1.390E+10	3.599E-13	4.386E-12	9.296E-01
27	1.111E-01	1.380E+09	1.528E+10	1.784E-13	4.564E-12	9.674E-01
28	6.738E-02	1.003E+09	1.628E+10	6.494E-14	4.629E-12	9.812E-01
29	4.087E-02	2.471E+08	1.653E+10	2.000E-14	4.649E-12	9.854E-01
30	3.183E-02	8.533E+07	1.661E+10	2.426E-14	4.674E-12	9.905E-01
31	2.606E-02	7.772E+08	1.739E+10	1.567E-14	4.689E-12	9.939E-01
32	2.418E-02	4.679E+08	1.786E+10	2.049E-15	4.691E-12	9.943E-01
33	2.188E-02	6.595E+08	1.852E+10	5.401E-15	4.697E-12	9.954E-01
34	1.503E-02	5.683E+08	1.908E+10	1.066E-14	4.707E-12	9.977E-01
35	7.102E-03	7.278E+08	1.981E+10	6.473E-15	4.714E-12	9.991E-01
36	3.355E-03	4.895E+08	2.030E+10	1.723E-15	4.716E-12	9.994E-01
37	1.585E-03	7.618E+08	2.106E+10	1.281E-15	4.717E-12	9.997E-01
38	4.540E-04	3.109E+08	2.137E+10	3.065E-17	4.717E-12	9.997E-01
39	2.144E-04	3.510E+08	2.173E+10	5.033E-17	4.717E-12	9.997E-01
40	1.013E-04	4.622E+08	2.219E+10	1.031E-16	4.717E-12	9.997E-01
41	3.727E-05	5.283E+08	2.272E+10	2.081E-16	4.717E-12	9.998E-01
42	1.068E-05	2.654E+08	2.298E+10	1.705E-16	4.718E-12	9.998E-01
43	5.043E-06	2.545E+08	2.324E+10	2.545E-16	4.718E-12	9.999E-01
44	1.855E-06	1.198E+08	2.336E+10	1.842E-16	4.718E-12	9.999E-01
45	8.764E-07	6.566E+07	2.342E+10	1.473E-16	4.718E-12	9.999E-01
46	4.140E-07	2.682E+07	2.345E+10	1.101E-16	4.718E-12	1.000E+00
47	1.000E-07	1.245E+07	2.346E+10	1.267E-16	4.718E-12	1.000E+00

Table 4.17. Flux and dpa spectra for 3° cavity dosimeters

Group	Energy (MeV)	Group flux ($n/cm^2 \cdot s$)	Cumulative flux ($n/cm^2 \cdot s$)	Group dpa rate ($dpa \cdot s^{-1}$)	Cumulative dpa rate ($dpa \cdot s^{-1}$)	dpa fraction
1	1.733E+01	1.412E+05	1.412E+05	4.126E-16	4.126E-16	1.157E-04
2	1.419E+01	5.744E+05	7.157E+05	1.520E-15	1.933E-15	5.418E-04
3	1.221E+01	2.014E+06	2.730E+06	4.852E-15	6.784E-15	1.902E-03
4	1.000E+01	4.002E+06	6.732E+06	8.881E-15	1.566E-14	4.392E-03
5	8.607E+00	6.410E+06	1.314E+07	1.338E-14	2.904E-14	8.142E-03
6	7.408E+00	1.280E+07	2.594E+07	2.487E-14	5.391E-14	1.511E-02
7	6.065E+00	1.676E+07	4.270E+07	2.990E-14	8.381E-14	2.350E-02
8	4.966E+00	2.845E+07	7.115E+07	4.469E-14	1.285E-13	3.603E-02
9	3.679E+00	2.210E+07	9.324E+07	3.027E-14	1.588E-13	4.451E-02
10	3.012E+00	1.781E+07	1.111E+08	2.264E-14	1.814E-13	5.086E-02
11	2.725E+00	2.288E+07	1.339E+08	2.917E-14	2.106E-13	5.904E-02
12	2.466E+00	1.278E+07	1.467E+08	1.498E-14	2.256E-13	6.323E-02
13	2.365E+00	4.453E+06	1.512E+08	4.880E-15	2.304E-13	6.460E-02
14	2.346E+00	2.211E+07	1.733E+08	2.302E-14	2.535E-13	7.106E-02
15	2.231E+00	5.884E+07	2.321E+08	6.084E-14	3.143E-13	8.811E-02
16	1.920E+00	9.154E+07	3.237E+08	7.445E-14	3.887E-13	1.090E-01
17	1.653E+00	1.530E+08	4.766E+08	1.240E-13	5.127E-13	1.437E-01
18	1.353E+00	4.352E+08	9.118E+08	2.438E-13	7.565E-13	2.121E-01
19	1.003E+00	4.422E+08	1.354E+09	1.621E-13	9.186E-13	2.575E-01
20	8.208E-01	1.938E+08	1.548E+09	1.087E-13	1.027E-12	2.880E-01
21	7.427E-01	1.110E+09	2.657E+09	4.010E-13	1.428E-12	4.004E-01
22	6.081E-01	9.817E+08	3.639E+09	2.889E-13	1.717E-12	4.814E-01
23	4.979E-01	1.105E+09	4.744E+09	4.380E-13	2.155E-12	6.042E-01
24	3.688E-01	1.893E+09	6.637E+09	3.913E-13	2.547E-12	7.139E-01
25	2.972E-01	1.950E+09	8.587E+09	3.910E-13	2.938E-12	8.235E-01
26	1.832E-01	2.134E+09	1.072E+10	3.009E-13	3.238E-12	9.079E-01
27	1.111E-01	1.163E+09	1.188E+10	1.503E-13	3.389E-12	9.501E-01
28	6.738E-02	8.340E+08	1.272E+10	5.402E-14	3.443E-12	9.652E-01
29	4.087E-02	2.642E+08	1.298E+10	2.138E-14	3.464E-12	9.712E-01
30	3.183E-02	1.610E+08	1.314E+10	4.577E-14	3.510E-12	9.840E-01
31	2.606E-02	6.762E+08	1.382E+10	1.363E-14	3.524E-12	9.878E-01
32	2.418E-02	4.213E+08	1.424E+10	1.845E-15	3.525E-12	9.884E-01
33	2.188E-02	6.616E+08	1.490E+10	5.419E-15	3.531E-12	9.899E-01
34	1.503E-02	7.161E+08	1.562E+10	1.343E-14	3.544E-12	9.936E-01
35	7.102E-03	6.879E+08	1.631E+10	6.118E-15	3.550E-12	9.954E-01
36	3.355E-03	5.582E+08	1.686E+10	1.965E-15	3.552E-12	9.959E-01
37	1.585E-03	8.323E+08	1.770E+10	1.400E-15	3.554E-12	9.963E-01
38	4.540E-04	4.161E+08	1.811E+10	4.102E-17	3.554E-12	9.963E-01
39	2.144E-04	4.074E+08	1.852E+10	5.843E-17	3.554E-12	9.963E-01
40	1.013E-04	5.016E+08	1.902E+10	1.119E-16	3.554E-12	9.964E-01
41	3.727E-05	5.617E+08	1.958E+10	2.213E-16	3.554E-12	9.964E-01
42	1.068E-05	3.020E+08	1.989E+10	1.941E-16	3.554E-12	9.965E-01
43	5.043E-06	3.456E+08	2.023E+10	3.456E-16	3.555E-12	9.966E-01
44	1.855E-06	2.186E+08	2.045E+10	3.360E-16	3.555E-12	9.967E-01
45	8.764E-07	1.833E+08	2.063E+10	4.114E-16	3.556E-12	9.968E-01
46	4.140E-07	3.384E+08	2.097E+10	1.389E-15	3.557E-12	9.972E-01
47	1.000E-07	9.922E+08	2.196E+10	1.009E-14	3.567E-12	1.000E+00

Table 4.18. Flux and dpa spectra for 9° cavity dosimeters

Group	Energy (MeV)	Group flux ($n/cm^2 \cdot s$)	Cumulative flux ($n/cm^2 \cdot s$)	Group dpa rate ($dpa \cdot s^{-1}$)	Cumulative dpa rate ($dpa \cdot s^{-1}$)	dpa fraction
1	1.733E+01	1.310E+05	1.310E+05	3.827E-16	3.827E-16	1.048E-04
2	1.419E+01	5.329E+05	6.639E+05	1.410E-15	1.793E-15	4.908E-04
3	1.221E+01	1.855E+06	2.519E+06	4.469E-15	6.262E-15	1.714E-03
4	1.000E+01	3.688E+06	6.207E+06	8.183E-15	1.444E-14	3.954E-03
5	8.607E+00	5.920E+06	1.213E+07	1.235E-14	2.680E-14	7.337E-03
6	7.408E+00	1.198E+07	2.411E+07	2.328E-14	5.008E-14	1.371E-02
7	6.065E+00	1.593E+07	4.003E+07	2.841E-14	7.849E-14	2.149E-02
8	4.966E+00	2.762E+07	6.765E+07	4.338E-14	1.219E-13	3.337E-02
9	3.679E+00	2.165E+07	8.930E+07	2.967E-14	1.515E-13	4.149E-02
10	3.012E+00	1.731E+07	1.066E+08	2.200E-14	1.735E-13	4.751E-02
11	2.725E+00	2.239E+07	1.290E+08	2.855E-14	2.021E-13	5.533E-02
12	2.466E+00	1.248E+07	1.415E+08	1.463E-14	2.167E-13	5.933E-02
13	2.365E+00	4.182E+06	1.457E+08	4.584E-15	2.213E-13	6.059E-02
14	2.346E+00	2.072E+07	1.664E+08	2.157E-14	2.429E-13	6.649E-02
15	2.231E+00	5.445E+07	2.208E+08	5.630E-14	2.992E-13	8.191E-02
16	1.920E+00	8.503E+07	3.059E+08	6.915E-14	3.683E-13	1.008E-01
17	1.653E+00	1.466E+08	4.524E+08	1.188E-13	4.871E-13	1.334E-01
18	1.353E+00	4.066E+08	8.591E+08	2.278E-13	7.149E-13	1.957E-01
19	1.003E+00	4.162E+08	1.275E+09	1.525E-13	8.675E-13	2.375E-01
20	8.208E-01	2.165E+08	1.492E+09	1.214E-13	9.889E-13	2.707E-01
21	7.427E-01	1.031E+09	2.523E+09	3.727E-13	1.362E-12	3.728E-01
22	6.081E-01	9.949E+08	3.518E+09	2.928E-13	1.654E-12	4.529E-01
23	4.979E-01	1.098E+09	4.616E+09	4.351E-13	2.089E-12	5.720E-01
24	3.688E-01	1.801E+09	6.416E+09	3.722E-13	2.462E-12	6.739E-01
25	2.972E-01	2.251E+09	8.667E+09	4.514E-13	2.913E-12	7.975E-01
26	1.832E-01	2.369E+09	1.104E+10	3.340E-13	3.247E-12	8.890E-01
27	1.111E-01	1.379E+09	1.242E+10	1.783E-13	3.425E-12	9.378E-01
28	6.738E-02	1.008E+09	1.342E+10	6.526E-14	3.491E-12	9.556E-01
29	4.087E-02	3.487E+08	1.377E+10	2.822E-14	3.519E-12	9.634E-01
30	3.183E-02	2.322E+08	1.400E+10	6.601E-14	3.585E-12	9.814E-01
31	2.606E-02	5.817E+08	1.459E+10	1.173E-14	3.597E-12	9.846E-01
32	2.418E-02	4.272E+08	1.501E+10	1.871E-15	3.598E-12	9.852E-01
33	2.188E-02	8.267E+08	1.584E+10	6.771E-15	3.605E-12	9.870E-01
34	1.503E-02	9.493E+08	1.679E+10	1.781E-14	3.623E-12	9.919E-01
35	7.102E-03	8.626E+08	1.765E+10	7.672E-15	3.631E-12	9.940E-01
36	3.355E-03	7.236E+08	1.837E+10	2.547E-15	3.633E-12	9.947E-01
37	1.585E-03	1.055E+09	1.943E+10	1.775E-15	3.635E-12	9.952E-01
38	4.540E-04	5.344E+08	1.996E+10	5.268E-17	3.635E-12	9.952E-01
39	2.144E-04	5.087E+08	2.047E+10	7.295E-17	3.635E-12	9.952E-01
40	1.013E-04	6.231E+08	2.110E+10	1.390E-16	3.635E-12	9.952E-01
41	3.727E-05	6.956E+08	2.179E+10	2.740E-16	3.636E-12	9.953E-01
42	1.068E-05	3.759E+08	2.217E+10	2.416E-16	3.636E-12	9.954E-01
43	5.043E-06	4.347E+08	2.260E+10	4.347E-16	3.636E-12	9.955E-01
44	1.855E-06	2.800E+08	2.288E+10	4.303E-16	3.637E-12	9.956E-01
45	8.764E-07	2.390E+08	2.312E+10	5.364E-16	3.637E-12	9.958E-01
46	4.140E-07	4.684E+08	2.359E+10	1.922E-15	3.639E-12	9.963E-01
47	1.000E-07	1.333E+09	2.492E+10	1.356E-14	3.653E-12	1.000E+00

Table 4.19. Flux and dpa spectra for 27° cavity dosimeters

Group	Energy (MeV)	Group flux ($n/cm^2 \cdot s$)	Cumulative flux ($n/cm^2 \cdot s$)	Group dpa rate ($dpa \cdot s^{-1}$)	Cumulative dpa rate ($dpa \cdot s^{-1}$)	dpa fraction
1	1.733E+01	1.070E+05	1.070E+05	3.125E-16	3.125E-16	1.212E-04
2	1.419E+01	4.353E+05	5.422E+05	1.152E-15	1.464E-15	5.679E-04
3	1.221E+01	1.470E+06	2.013E+06	3.542E-15	5.006E-15	1.942E-03
4	1.000E+01	2.888E+06	4.900E+06	6.407E-15	1.141E-14	4.427E-03
5	8.607E+00	4.566E+06	9.466E+06	9.530E-15	2.094E-14	8.123E-03
6	7.408E+00	9.104E+06	1.857E+07	1.769E-14	3.863E-14	1.498E-02
7	6.065E+00	1.192E+07	3.049E+07	2.127E-14	5.990E-14	2.323E-02
8	4.966E+00	2.029E+07	5.078E+07	3.187E-14	9.178E-14	3.559E-02
9	3.679E+00	1.566E+07	6.644E+07	2.145E-14	1.132E-13	4.391E-02
10	3.012E+00	1.239E+07	7.882E+07	1.574E-14	1.290E-13	5.002E-02
11	2.725E+00	1.604E+07	9.486E+07	2.045E-14	1.494E-13	5.795E-02
12	2.466E+00	8.849E+06	1.037E+08	1.037E-14	1.598E-13	6.197E-02
13	2.365E+00	2.882E+06	1.066E+08	3.159E-15	1.629E-13	6.320E-02
14	2.346E+00	1.438E+07	1.210E+08	1.497E-14	1.779E-13	6.901E-02
15	2.231E+00	3.805E+07	1.590E+08	3.935E-14	2.173E-13	8.427E-02
16	1.920E+00	5.859E+07	2.176E+08	4.765E-14	2.649E-13	1.027E-01
17	1.653E+00	1.013E+08	3.189E+08	8.205E-14	3.470E-13	1.346E-01
18	1.353E+00	2.782E+08	5.970E+08	1.559E-13	5.028E-13	1.950E-01
19	1.003E+00	2.843E+08	8.813E+08	1.042E-13	6.070E-13	2.354E-01
20	8.208E-01	1.519E+08	1.033E+09	8.520E-14	6.922E-13	2.685E-01
21	7.427E-01	7.066E+08	1.740E+09	2.554E-13	9.476E-13	3.675E-01
22	6.081E-01	6.879E+08	2.428E+09	2.024E-13	1.150E-12	4.460E-01
23	4.979E-01	7.681E+08	3.196E+09	3.045E-13	1.454E-12	5.641E-01
24	3.688E-01	1.248E+09	4.443E+09	2.579E-13	1.712E-12	6.641E-01
25	2.972E-01	1.610E+09	6.054E+09	3.229E-13	2.035E-12	7.894E-01
26	1.832E-01	1.707E+09	7.761E+09	2.407E-13	2.276E-12	8.827E-01
27	1.111E-01	1.013E+09	8.774E+09	1.310E-13	2.407E-12	9.336E-01
28	6.738E-02	7.503E+08	9.525E+09	4.860E-14	2.456E-12	9.524E-01
29	4.087E-02	2.633E+08	9.788E+09	2.131E-14	2.477E-12	9.607E-01
30	3.183E-02	1.770E+08	9.965E+09	5.032E-14	2.527E-12	9.802E-01
31	2.606E-02	4.192E+08	1.038E+10	8.451E-15	2.536E-12	9.835E-01
32	2.418E-02	3.057E+08	1.069E+10	1.339E-15	2.537E-12	9.840E-01
33	2.188E-02	6.067E+08	1.130E+10	4.969E-15	2.542E-12	9.859E-01
34	1.503E-02	7.224E+08	1.202E+10	1.355E-14	2.556E-12	9.912E-01
35	7.102E-03	6.619E+08	1.268E+10	5.888E-15	2.561E-12	9.934E-01
36	3.355E-03	5.614E+08	1.324E+10	1.976E-15	2.563E-12	9.942E-01
37	1.585E-03	8.241E+08	1.407E+10	1.386E-15	2.565E-12	9.948E-01
38	4.540E-04	4.209E+08	1.449E+10	4.149E-17	2.565E-12	9.948E-01
39	2.144E-04	4.008E+08	1.489E+10	5.748E-17	2.565E-12	9.948E-01
40	1.013E-04	4.921E+08	1.538E+10	1.098E-16	2.565E-12	9.948E-01
41	3.727E-05	5.508E+08	1.593E+10	2.170E-16	2.565E-12	9.949E-01
42	1.068E-05	2.985E+08	1.623E+10	1.918E-16	2.565E-12	9.950E-01
43	5.043E-06	3.461E+08	1.658E+10	3.461E-16	2.566E-12	9.951E-01
44	1.855E-06	2.232E+08	1.680E+10	3.431E-16	2.566E-12	9.953E-01
45	8.764E-07	1.909E+08	1.699E+10	4.284E-16	2.567E-12	9.954E-01
46	4.140E-07	3.723E+08	1.736E+10	1.528E-15	2.568E-12	9.960E-01
47	1.000E-07	1.010E+09	1.837E+10	1.028E-14	2.578E-12	1.000E+00

ORNL DWG. NO. 89-19743/R1

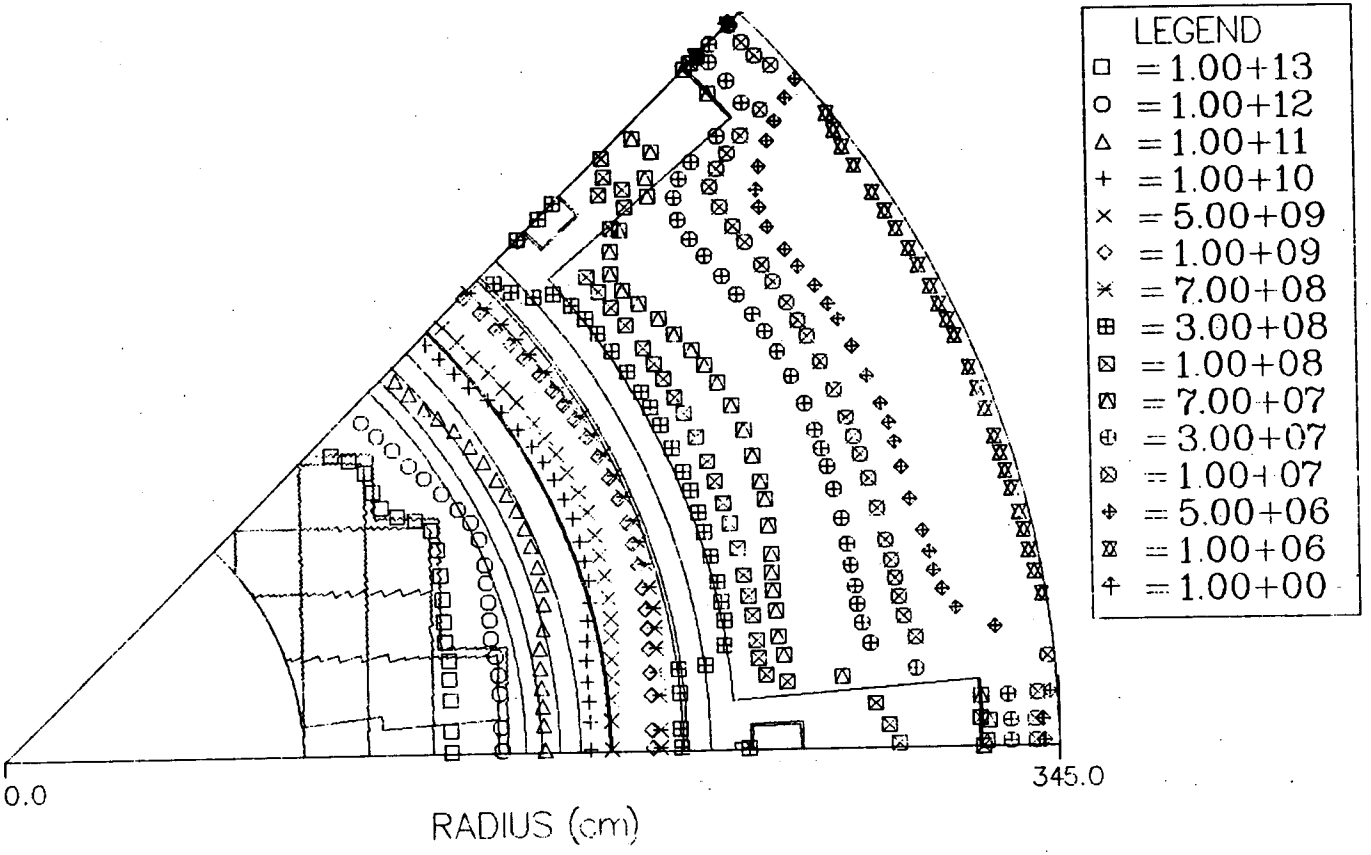

Fig. 4.9. Iso-flux (ϕ > 1 MeV) contour at lower weld location in H. B. Robinson cycle 10.

ORNL DWG. NO. 89-19744/R1

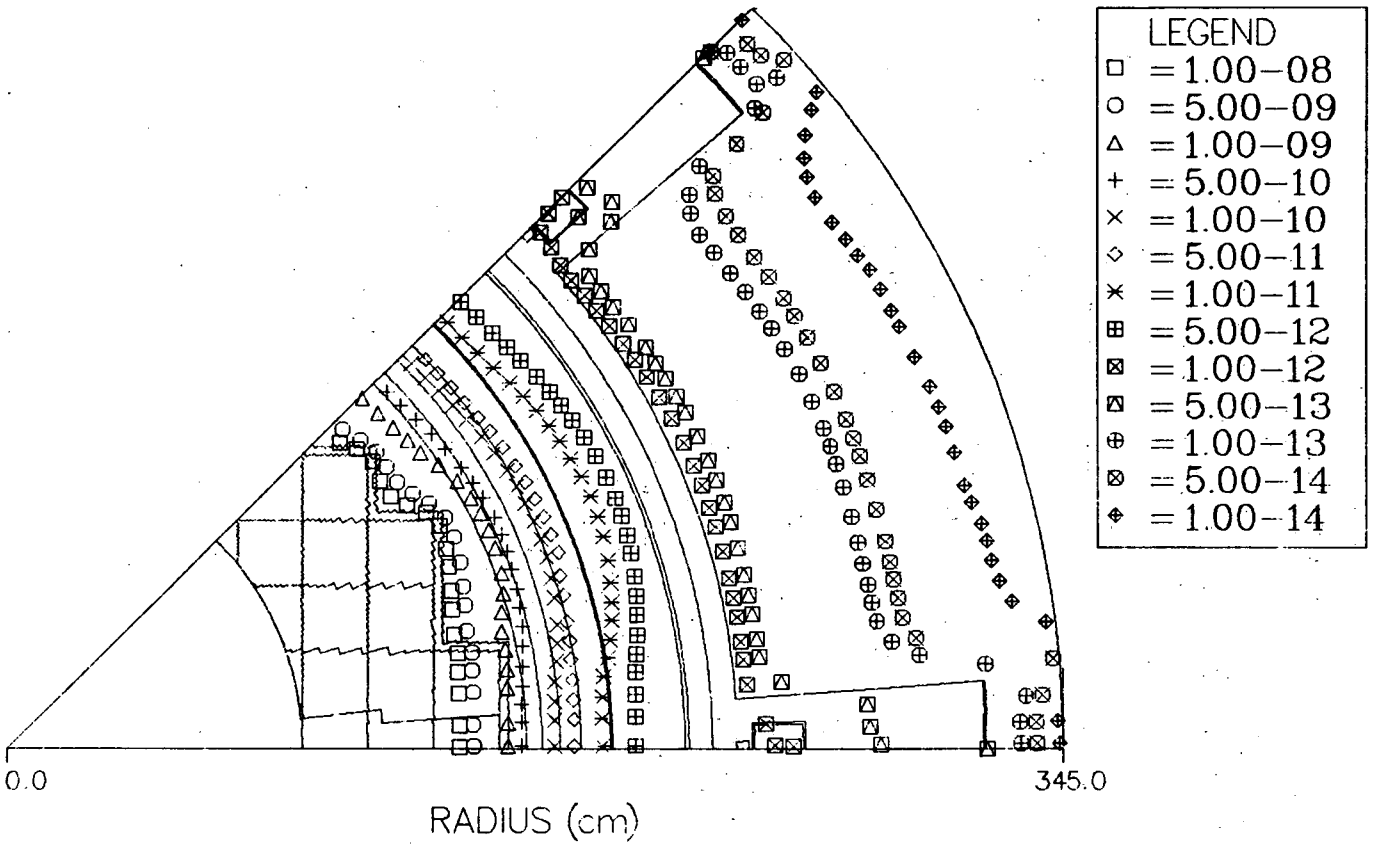

Fig. 4.10. Iso-dpa contours at lower weld location in H. B. Robinson cycle 10.

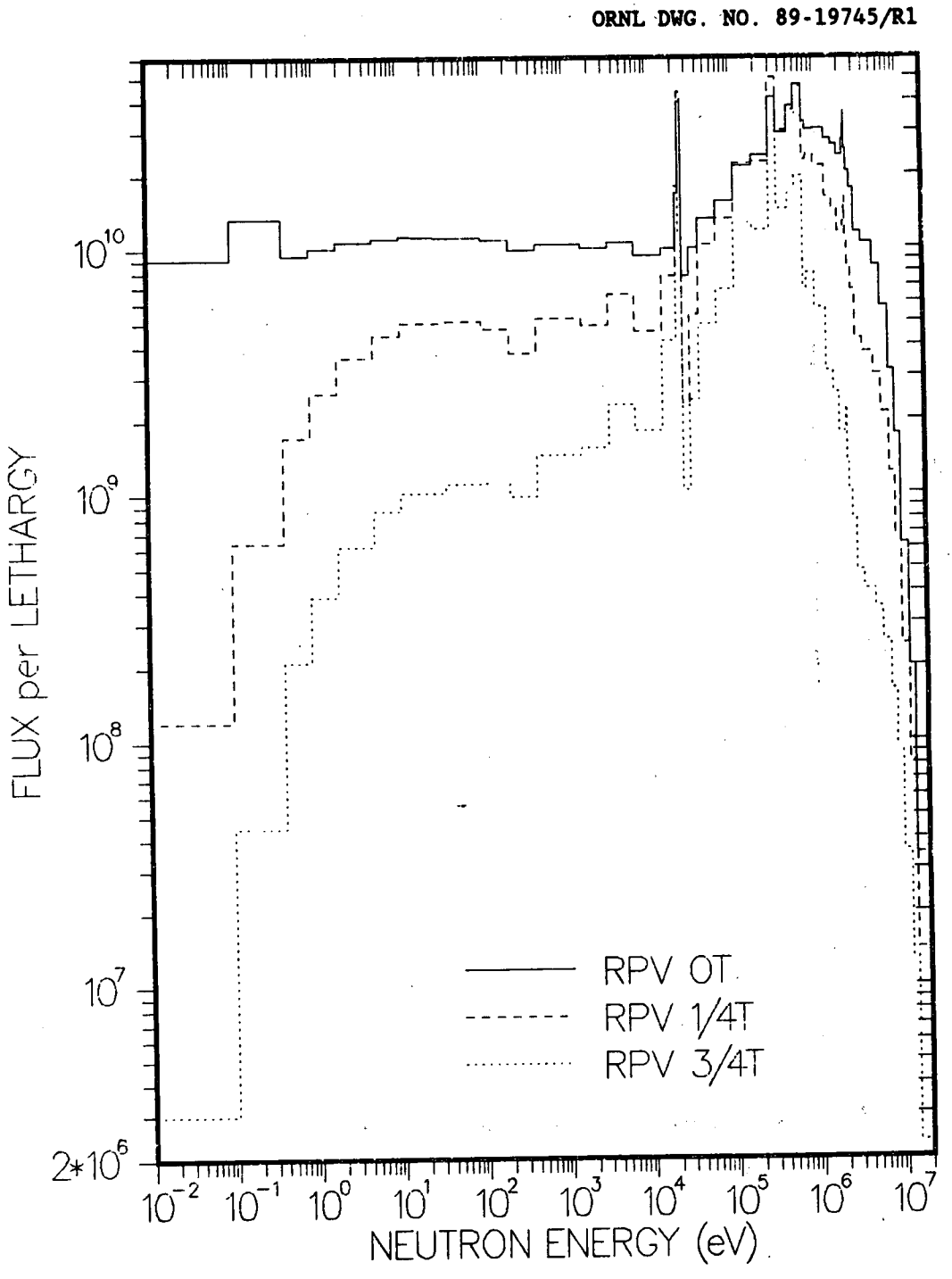

Fig. 4.11. Neutron flux spectrum in RPV at peak midplane location.

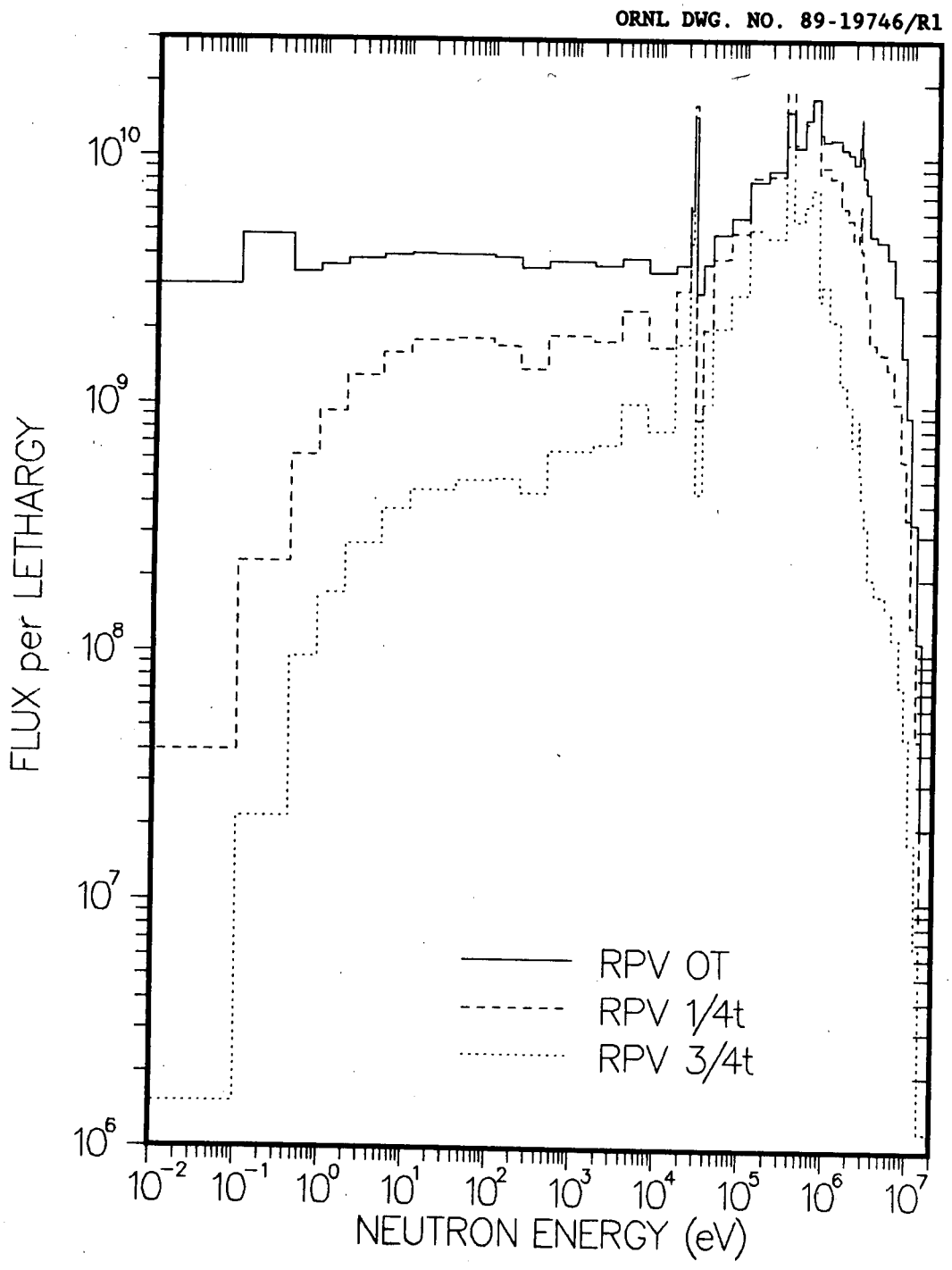

Fig. 4.12. Neutron flux spectrum in RPV at peak lower weld location.

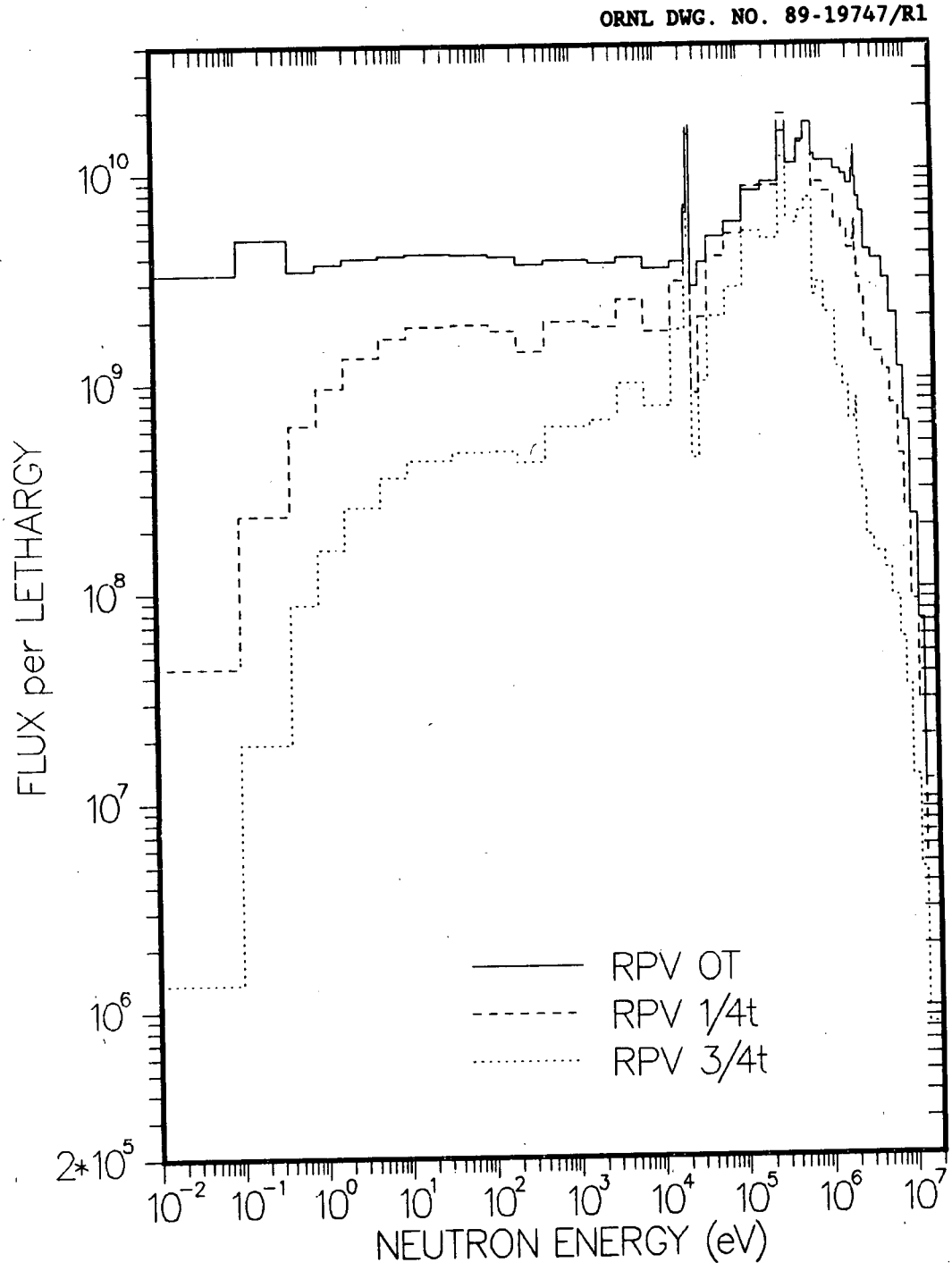

Fig. 4.13. Neutron flux spectrum in RPV at peak upper weld location.

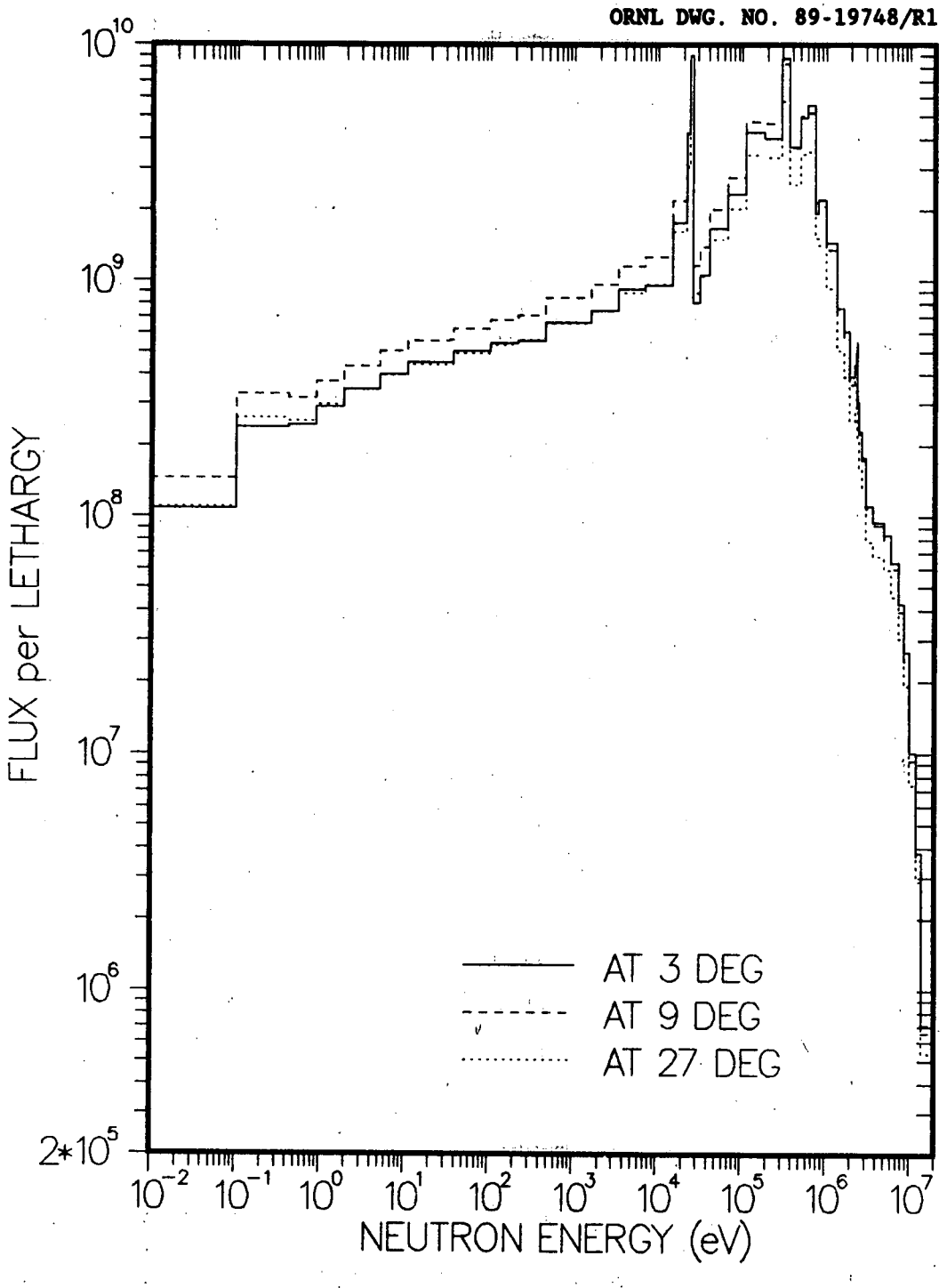

Fig. 4.14. Neutron flux spectrum in cavity at dosimeter locations.

5. LEPRICON ADJUSTMENT CALCULATIONS

Adjustment is often a significant part of determining reactor pressure vessel fluences. For example, the final ORNL result for the fluence at the lower weld for cycle 9 of HBR Unit 2 included a 22% increase in the original calculation of the flux above 1 MeV.[5] This modification was due to a "consolidation" of the measured dosimeter activities and the transport calculations, using the LEPRICON adjustment code.[6] The Westinghouse result for this fluence is about 20% higher than the final ORNL result.[2,4] While the cause of this difference has not been fully investigated, variations in the adjustment procedures are a leading candidate for the difference since similar cross sections and geometric models were used.

The 22% adjustment mentioned above resulted from two main factors. About 6% was from an out-of-roundness correction that inferred a decrease in the downcomer thickness of about 6 mm (0.2 in.) from its nominal value. Most of the rest of the adjustment came from changes to the iron inelastic cross section. The calculation of cycle 9 with updated iron cross sections indicates that the increase in fluence obtained using the newer cross sections is about the same as was inferred from the adjustment of the iron inelastic cross section. This implies that little nuclear data adjustment is needed with the new iron cross sections, at least in the energy range above 3 MeV. If these conclusions are extrapolated to the present cycle 10 calculations, it is expected that the unadjusted results would be fairly accurate at the lower weld, with perhaps a 6 or 7% increase for out-of-roundness.

The LEPRICON adjustment module has been updated to accept calculations made with the updated iron cross sections (Fu evaluation) as well as the older cross sections. Thus, LEPRICON can also be applied to the calculations described in this report. However, the adjustment is not expected to modify the current nuclear data much, since only the iron data above 3 MeV was modified significantly previously, and the new cross sections used in this analysis should remove this adjustment. The LEPRICON adjustment procedure also includes 37 "clean" benchmark experiments as well as the measurements from the reactor being analyzed. These benchmark experiments prevent the nuclear data from being changed significantly no matter what reactor measurements are included, since the benchmark measurements have low uncertainties that tend to severely constrain the modifications to cross sections.

It appears that if the new Fu iron data are utilized in the transport calculations, then in practice the only way that the reactor measurements will significantly affect the LEPRICON adjustment is through the bias factors built into the procedure or by changing the iron data below 3 MeV. It should be pointed out that the benchmark experiments have no effect on the adjustment of the bias factors.

Thus, when LEPRICON is given measurements and calculations that disagree, the bias factors are the main mechanisms available to reconcile the disagreement, unless considerable uncertainty is assumed in the iron cross section data between 1 and 3 MeV.

Although the main purpose of the present study was to obtain a "reference" set of results based on transport calculations, the impact of a possible least-squares adjustment on the analysis has also been examined. The LEPRICON code was utilized, however, the present version of LEPRICON routinely considers only one cavity location at a time. This means that even though measurements were made at four different azimuthal locations, a simultaneous adjustment was not performed. Therefore for cycle 10, only four reactor measurements are available for inclusion in the adjustment. In contrast, 12 measurements were included for cycle 9—six at the downcomer location and six in the cavity.

For cycle 10, the calculations and measurements shown in this report for the iron and nickel dosimeters are in fair agreement, while the ^{238}U and ^{237}Np dosimeters are not. To demonstrate a range of adjustments predicted by LEPRICON, two adjustment calculations were performed for the measurements at an azimuth of 3 degrees. The iron measurement was assigned an uncertainty of 6.16%, the same value used for the cycle 9 analysis. The nickel measurement was a gradient wire instead of a foil with an uncertainty of 12%. Since the ^{238}U measurements were quite questionable, an uncertainty of 50% was used. For the ^{237}Np measurements two uncertainties, 5% and 20%, were assumed. The 5% number covers the possibility that the measured value is accurate and there is something inconsistent with the calculation, while the 20% uncertainty allows the possibility that the measurement is poor. The adjusted dosimeter values for these cases are shown in Table 5.1. For the 20% case, the adjusted values are close to the calculated values for the fission detectors. That is, the discrepancies have been reconciled by moving the experimental values much more than the calculated values. In the 5% case, the adjustment procedure changes the bias factors significantly in order to make the calculation better match the ^{237}Np measurement. The flux adjustments at the inside of the vessel and in the cavity for these two cases are shown in Tables 5.2 and 5.3. The adjustments for the 20% case indicate that the flux greater than 1 MeV increases about 10% at the inside of the vessel. This is about what was expected based on the cycle 9 results. However, the 5% case has large adjustments of about 25%, which significantly affect the flux. Thus the projected fluence is strongly dependent on whether or not the ^{237}Np measurement is believable.

The adjustments in the 5% case were mostly caused by the out-of-roundness bias factor and, to a lesser degree, the water density bias factor. Both of these bias factors reduce the amount of water in the downcomer. The bias factor for uncertainty in the concrete composition also played a major role in the adjustment, but it changes only the fluxes in the cavity and not the fluxes at the inside of the vessel.

Tables 5.4 and 5.5 give the individual contributions to the flux adjustment for group 12 (0.907 to 0.608 MeV). The adjustment assigned to the flux synthesis is perhaps too low since partial length shield assemblies are present. The fact that the iron cross section data in the range of 1-3 MeV was not adjusted indicates that the uncertainties in this group data were small or the sensitivities to this data, which are built into LEPRICON, are low. It is known that the Np reaction rate is sensitive to the flux in this energy range.

If the values in either of these sets of parameters (i.e., the cross section co-variances or sensitivities) are inaccurate, then the adjustment may be missing the actual cause of the discrepancy in the calculation of the Np reaction rate.

The question of whether the ^{237}Np dosimeter is undercalculated when the new iron cross sections are used is still an open one. The fact that LEPRICON changes the amount of water in the downcomer does not mean that this is definitely the problem, but only that of the factors used in the LEPRICON calculations, these changes reconcile the experiments and measurements while minimizing the changes made in a least-squares sense. The only correct way to address the apparent disagreement is to first determine if the disagreement is real, and if it is, find out what is causing the problem. The previous ORNL cycle 9 analysis performed by Maerker has omitted the Np measurement, while Westinghouse has included it. A more accurate set of Np measurements based on foils as well as SSTRs needs to be made in some future HBR cycle so that this issue can be resolved. Only then can a realistic adjustment be made with confidence.

Because some questions still remain concerning the appropriate adjustment procedure for this case, this report has only emphasized the reference (i.e., unadjusted) transport calculations.

Table 5.1. Adjustment of dosimeter values at 3° from LEPRICON for uncertainties in the ^{237}Np measurement of 5% and 20%

Response	Calculated	Experimental	Adjusted (20%)	Adjusted (5%)
$^{54}Fe(n,p)$	4.180-17	4.80-17	4.749-17	5.096-17
$^{58}Ni(n,p)$	6.256-17	6.87-17	7.166-17	7.768-17
$^{238}U(n,f)$	2.575-16	3.90-16	2.877-16	3.238-16
$^{237}Np(n,f)$	4.999-15	7.69-15	5.695-15	6.878-15

Table 5.2. LEPRICON flux adjustments for a ^{237}Np uncertainty of 20%

Group number	High energy (MeV)	Low energy (MeV)	$\frac{A}{C}-1$[a] Vessel surface (%)	$\frac{A}{C}-1$[a] Cavity (%)
1	19.640	11.050	13.5379	10.2482
2	11.050	8.187	7.2046	-2.9866
3	8.187	6.065	8.2081	1.7947
4	6.065	4.066	15.2068	21.2809
5	4.066	3.012	15.0558	20.4389
6	3.012	2.592	14.4639	19.0892
7	2.592	2.123	14.2410	18.5761
8	2.123	1.827	10.9361	10.3268
9	1.827	1.496	10.3393	8.4636
10	1.496	1.225	10.3178	8.2533
11	1.225	0.907	11.2256	10.2841
12	0.907	0.608	14.3131	18.0625
13	0.608	0.369	14.3950	19.5644
14	0.369	0.213	14.3106	19.0289
15	0.213	0.111	14.2696	19.8688

[a]A = transport fluxes after adjustment by LEPRICON; C = original calculated transport fluxes.

Table 5.3. LEPRICON flux adjusted for a ^{237}Np uncertainty of 5%

Group number	High energy (MeV)	Low energy (MeV)	$\frac{A}{C} - 1$[a] Vessel surface (%)	$\frac{A}{C} - 1$[a] Cavity (%)
1	19.640	11.050	24.3011	20.4349
2	11.050	8.187	16.1162	2.3801
3	8.187	6.065	16.0752	4.3814
4	6.065	4.066	25.7919	31.0451
5	4.066	3.012	26.1254	30.0195
6	3.012	2.592	26.0937	28.9884
7	2.592	2.123	26.3439	29.5378
8	2.123	1.827	24.1838	26.1245
9	1.827	1.496	24.2650	25.0384
10	1.496	1.225	24.5168	25.4045
11	1.225	0.907	26.3360	29.9750
12	0.907	0.608	30.8265	40.7285
13	0.608	0.369	30.4421	49.1991
14	0.369	0.213	29.7098	46.1786
15	0.213	0.111	29.5342	51.0801

[a]A = transport fluxes after adjustment by LEPRICON; C = original calculated transport fluxes.

Table 5.4. Contributions to the flux adjustment for Group 12 for a ^{237}Np uncertainty of 20%

Nuclear data or bias factor	Change at vessel surface (%)	Change in the cavity (%)
^{235}U fission spectrum	3.8523	3.8523
Iron inelastic cross section	0.2091	0.5428
Pressure vessel out-of-roundness	6.3907	6.9320
Water density variations	2.3443	2.5459
3-D flux synthesis	1.2857	1.5125
Steel density variations	0.2310	1.3576
Cavity concrete backing		1.3194
Total	14.3131	18.0625

Table 5.5 Contributions to the flux adjustment for Group 12 for a ^{237}Np uncertainty of 5%

Nuclear data or bias factor	Change at vessel surface (%)	Change in the cavity (%)
^{235}U fission spectrum	4.5280	4.5280
Iron inelastic cross section	-0.6542	-1.6984
Pressure vessel out-of-roundness	17.0900	18.2319
Water density variations	6.5841	7.2458
3-D flux synthesis	3.0103	3.5416
Steel density variations	0.2683	1.1561
Cavity concrete backing		7.7235
Total	30.8265	40.7285

6. SUMMARY AND CONCLUSIONS

The transport calculations of HBR cycle 10 were some of the first to use the new iron cross-section data based on the recent Fu evaluation, and it is of interest to determine the accuracy of cavity-dosimetry results obtained from these calculations. Since cavity dosimetry will play an important role in establishing the future HBR RPV fluence, this information is important in assessing the reliability of the projected flux levels obtained by combining measured cavity dosimetry results with transport calculations. It was found that the reference transport calculations (with no adjustments) are able to predict the measured ^{54}Fe and ^{58}Ni cavity dosimeter activities within about 10-20%. The ^{238}U calculated results are about 35 to 50% lower than the measured values, but it is believed that most of this discrepancy is caused by problems with the measurements-most likely a calibration inconsistency with the SSTRs (e.g., an error in the fission deposit masses). The calculated ^{237}Np results are 35 to 40% lower than the measured values at the 3° and 9° azimuths, and again there seems to be some inconsistency in the various ^{237}Np dosimeter measurements at different cavity positions (e.g., the 27°position). However, transport calculations by Westinghouse using ENDF/B-IV iron cross sections (i.e., the data in the SAILOR library) give consistent C/E ratios for ^{54}Fe, ^{58}Ni, and ^{237}Np, which are all about 40% lower than the measured results. On the other hand, the calculations here give C/Es only about 15% lower for ^{54}Fe and ^{58}Ni, but the ^{237}Np results are substantially lower. Thus, it appears that the new Fu iron data will improve the agreement between calculations and measurements of the ^{54}Fe and ^{58}Ni dosimeters in the cavity, but the computed ^{237}Np results will remain too low. Unfortunately at this time it cannot be concluded that these results indicate a further modification is needed in the iron data (e.g., reduction in the cross section in the range 1 to 3 MeV), because of questions about the reliability of the ^{237}Np measurements. This issue certainly needs to be resolved if the ^{237}Np cavity measurements are going to be included in the adjustment of the flux spectrum for HBR. Because of its low threshold, the ^{237}Np has a large effect on the adjusted fast flux and dpa levels.

The calculated ^{235}U dosimetry results are about 45% lower than the measurements, but there is a large uncertainty in the experimental values, so this discrepancy should cause no concern at this time. The ^{59}Co dosimeter calculations are also about 40% lower than the measurements, on the average. Because Westinghouse places a low uncertainty on these measurements and because of the large uncertainties in the calculated thermal flux, the measured ^{59}Co dosimeter activities should be used to establish the thermal flux level in the cavity.

The reference calculation of the axial variation of the ^{54}Fe and ^{58}Ni gradient wire activities in the cavity generally show fairly good agreement with the measured distributions, but there seems to be a tendency to underestimate the fast flux near the midplane at 3° and 9°. This indicates that the two-channel synthesis method is able to reasonably treat the asymmetries introduced by the presence of the PLSA elements.

The values for the fast flux at the three cavity dosimeter capsules were computed to be 9.12E8, 8.52E8, and 5.97E8 n/cm^2•s at the 3°, 9°, and 27° positions, respectively. The corresponding dpa rate values are 3.57E-12, 3.65E-12, and 2.58E-12.

The transport calculations show that the PLSAs cause the flux above 1.0 MeV incident on the lower weld of the RPV to peak at around 24°, while the peak flux at the midplane and upper weld elevations peak near 0° azimuth. The maximum fast fluence rate occurs at the midplane and is computed to be 3.79E10 n/cm^2•s, or 1.20E18 n/cm^2 per year. The peak value at the lower weld is 1.57E10 n/cm^2•s, or 4.97E17 n/cm^2 per year. The peak dpa rates at the midplane and lower weld are 6.18E-11 and 2.52E-11 dpa/s, respectively. The azimuthal variation of the 0-T fast flux is substantially different at the lower weld elevation than at the core midplane, due to the PLSA elements on the core flats. Calculations show that at the lower weld elevation, the ratio of the peak fast flux (at 24°) to the minimum (at ~0°) for 0-T is equal to 3.0. However, at the midplane, the peak flux (at 0°) to minimum flux (at 45°) ratio is 3.7. Thus, the PLSAs have flattened the azimuthal shape by reducing the flux near 0° at the lower weld. The ratio of the peak flux at the lower weld to the peak flux at the midplane is equal to 0.41–this is a much smaller value than seen in earlier cycles because of the addition of the PLSA elements.

The ratio of the fast flux at 1/4-T to that at 0-T is equal to 0.52, while the ratio of the 3/4-T to 0-T value is 0.097. The corresponding dpa values are 0.62 and 0.20. These ratios, which are based on calculations performed using the Fu evaluation for iron, are expected to be different from values obtained with the original SAILOR data, because of the difference in the flux attenuation properties of the different cross section data.

There are some major differences in the results obtained from the transport calculations here and those reported by Westinghouse in Reference 3. In the cavity, the fast flux computed and adjusted by Westinghouse at the 3° and 9° dosimetry positions is about 30-40% higher than the reference (unadjusted) values, and their flux at 27° is about 20% higher. This indicates not only a significant difference in the absolute magnitudes, but also in the relative azimuthal variation. The flux incident on the RPV also is different in the two sets of calculations. The peak flux at the 0-T midplane location (at 0°) is about 25% lower in the ORNL calculation.

At the lower weld elevation, the ORNL flux is about 30% lower at the peak azimuth location, which occurs at 24°. Thus, the reference ORNL transport calculations seem to generally indicate a lower fluence accumulation rate than reported by Westinghouse.

At this time, the causes of the discrepancies in the ORNL and Westinghouse results are still being examined. Certainly, the different iron cross-section data used in the transport calculations will introduce differences. Variations in the DOT models and source representations could also have an impact. However, it appears that the largest discrepancy between the two

sets of results is because of the least-squares adjustment and normalization procedure utilized by Westinghouse, which incorporates the cavity dosimeter measurements directly with their transport calculations to obtain the final estimate for the fluxes. If both organizations use the same SAILOR cross section data, then the basic ORNL and Westinghouse transport calculations appear to agree reasonably well (within ~10%) prior to the adjustment.[12] In particular, it seems that the measured dosimeter activities are pulling up the Westinghouse transport calculations for ϕ(>1 MeV) by about 40% through the adjustment procedure. Since the reference ORNL results used the Fu iron data and are not adjusted, the discrepancy with the Westinghouse results essentially reflects the ORNL C/E values for the Np dosimeters in the cavity, at least at 3° and 9°. That is, the reference (unadjusted) ORNL transport calculations underestimate these Np activities by about 40%, therefore if the reference ORNL transport results are adjusted assuming a small (5%) uncertainty in the Np measurements, the adjusted flux values will then agree closely with the Westinghouse results, due mainly to adjustments made to the spectrum in the energy range of 1-3 MeV. Because of the lack of confidence at this time in the reliability of the cycle 10 Np measurements, this data was not used to adjust the referenced results.

A number of recommendations are suggested based on the results of this work. Among these are the following:

(a) Perhaps most important is the need to obtain highly accurate cavity dosimetry for HBR. It is recommended that both activation foils as well as SSTR data for ^{238}U and ^{237}Np be taken in some future cycle, and that these data be used in conjunction with in-vessel dosimetry to provide a reliable set of experimental results for a "definitive" comparison with transport calculations.

(b) The impact of recent modifications in the iron inelastic cross section above 3 MeV on the cavity dosimetry analysis needs to be examined in more detail. It appears that the Fu evaluation used in this study causes high energy threshold reactions like ^{54}Fe (n,p) and ^{58}Ni (n,p) to increase, while the ^{237}Np (n,f) reaction rate (which has a lower threshold and thus is more similar to the fast flux response) changes only a small amount. This introduces a bias into the various dosimeter results that has not been observed in previous analysis based on ENDF/B IV iron data. The recently released ENDF/B VI iron data should be processed and tested to see if a similar effect occurs. Comparison of calculated and measured energy-spectra in simple benchmark configurations (e.g., one dimensional iron spheres) should be performed to identify the energy ranges where discrepancies occur in the flux.

(c) Sensitivity studies should be performed to estimate the impact of uncertainties in the iron cross sections below 3 MeV on cavity dosimetry calculations. If this data is found to be significant, then a cross section re-evaluation effort should be supported.

(d) It is clear from comparing ORNL and Westinghouse results that variations in adjustment methodologies can cause substantial differences in predicted RPV fluence levels, especially when cavity dosimetry is used in the adjustment. A fundamental and systematic study of adjustment techniques based on cavity dosimetry should be undertaken to establish consistency and to benchmark the various approaches.

(e) The two-channel synthesis approximation seems to give "acceptable" accuracy for this reactor configuration, but it is difficult to quantify the impact on HBR results because of uncertainties in the experimental measurements. There seems to be a tendency for the approximation to underestimate the midplane flux and there are also differences in the azimuthal variation of the computed and measured dosimeter activities within the cavity. It is recommended that at least one full blown, three-dimensional transport calculation be performed for one cycle of HBR in order to provide a benchmark solution.

(f) Although not a major concern in the present work, substantial errors were observed in the calculated and measured thermal reaction rates. The causes of these discrepancies have not been identified.

Many of the above recommendations will impact not only the H. B. Robinson analysis but also other reactors that will utilize cavity dosimetry to project RPV fluence.

7. REFERENCES

1. *H. B. Robinson Fluence Reduction Analysis for the Partial-Length Shield Assembly Concept*, TEC Report R-83-030, Technology for Energy Corporation and Carolina Power and Light Company, Raleigh, NC, 1983.

2. E. P. Lippincott et al., *Evaluation of Surveillance Capsule and Reactor Cavity Dosimetry from H. B. Robinson Unit 2, Cycle 9*, NUREG/CR-4576, WCAP-11104, Westinghouse Corporation, Pittsburgh, PA, February 1987.

3. E. P. Lippincott et al., *Reactor Cavity Neutron Dosimetry Program for H. B. Robinson Cycle 10*, WCAP-11481, Westinghouse Corporation, Pittsburgh, PA, April 1987.

4. S. L. Anderson, *Reactor Cavity Neutron Dosimetry Program for H. B. Robinson Unit 2 Cycle 11 Evaluations*, WCAP-11689, Westinghouse Electric Corporation, Pittsburgh, PA, December 1987.

5. R. E. Maerker, *LEPRICON Analysis of Pressure Vessel Surveillance Dosimetry Inserted into H. B. Robinson-2 during Cycle 9*, NUREG/CR-4439, ORNL/TM-10132, U. S. Nuclear Regulatory Commission, Washington, DC, August 1986.

6. B. L. Broadhead, R. E. Maerker, and J. J. Wagschal, *The LEPRICON Adjustment Module: A Generalized Linear Least Squares Data Analysis Program with Application to PWR Surveillance Dosimetry*, Electric Power Research Institute, Palo Alto, CA.

7. P. Chowdhury, M. L. Williams, and F. B. K. Kam, *Development of a Three-Dimensional Flux Synthesis Program and Comparison with 3-D Transport Theory Results*, NUREG/CR-4984, ORNL/TM-10503, U.S. Nuclear Regulatory Commission, Washington, DC, January 1988.

8. F. B. K. Kam, R. E. Maerker, M. L. Williams, and F. W. Stallmann, *Pressure Vessel Fluence Analysis and Neutron Dosimetry*, NUREG/CR-5049, ORNL/TM-10651, U.S. Nuclear Regulatory Commission, Washington, DC, December 1987.

9. R. E. Maerker, *Analysis of the VENUS-3 Experiments*, NUREG/CR-5338, ORNL/TM-11106, U.S. Nuclear Regulatory Commission, Washington, DC, August 1989.

10. G. L. Simmons and R. Roussin, *RSIC Data Library Collection (DLC-76) - SAILOR - Coupled, Self-shielded, 47 Neutron, 20 Gamma-ray, P_3, Cross Section Library for Light Water Reactors*, Radiation Shielding Information Center, Oak Ridge, TN, 1985.

7. REFERENCES (Continued)

11. M. L. Williams, *DOTSOR: A Module in the LEPRICON Computer Code System for Representing the Neutron Source Distribution in LWR Cores*, Electric Power Research Institute, Palo Alto, CA.

12. Westinghouse transport results provided to M. L. Williams (LSU/ORNL) by P. Lippincott (Westinghouse), December 1989.

NRC FORM 335 (2-84) NRCM 1102, 3201, 3202

U.S. NUCLEAR REGULATORY COMMISSION

BIBLIOGRAPHIC DATA SHEET

SEE INSTRUCTIONS ON THE REVERSE

1. REPORT NUMBER (Assigned by TIDC, add Vol No., if any)

NUREG/CR-5530
ORNL/TM-11476

2. TITLE AND SUBTITLE

Analysis of H. B. Robinson PWR Vessel Fluence for Cycle 10 Utilizing Partial Length Shield Assemblies

3. LEAVE BLANK

4. DATE REPORT COMPLETED

MONTH	YEAR
September	1989

5. AUTHOR(S)

M.L. Williams,* R.L. Childs, M. Asgari*

* Louisiana State University Nuclear Science Center

6. DATE REPORT ISSUED

MONTH	YEAR
September	1990

7. PERFORMING ORGANIZATION NAME AND MAILING ADDRESS (Include Zip Code)

Oak Ridge National Laboratory
Oak Ridge, TN 37831

8. PROJECT/TASK/WORK UNIT NUMBER

9. FIN OR GRANT NUMBER

B0415

10. SPONSORING ORGANIZATION NAME AND MAILING ADDRESS (Include Zip Code)

Division of Engineering
Office of Nuclear Regulatory Research
U.S. Nuclear Regulatory Commission
Washington DC 20555

11a. TYPE OF REPORT

Technical

b. PERIOD COVERED (Inclusive dates)

12. SUPPLEMENTARY NOTES

13. ABSTRACT (200 words or less)

Neutron transport calculations have been performed to determine the pressure vessel fluence and cavity dosimeter responses for cycle 10 of the H. B. Robinson pressurized water reactor. This cycle was the first to utilize "partial length shield assemblies" within the core to reduce the fluence rate at the critical weld location in the vessel. This work is part of the ongoing surveillance of the Robinson plant to insure that the projected fluence rates are reliable.

The flux calculations utilize a "two-channel" synthesis approximation and recently processed iron cross sections based on a new evaluation for the inelastic data above 3 MeV. The methodology used to calculate this highly asymmetrical configuration is discussed in detail, and a comparison of the calculated and measured cavity-dosimetry results is presented. Discrepancies are observed in the computed and measured results for the ^{237}Np dosimeter, and possible explanations are discussed. Calculated absolute neutron flux spectra, as well as radial, azimuthal, and axial variations in the fast flux and dpa within the pressure vessel, are given.

The effect of a least-squares consolidation of the measured and calculated results is studied.

14. DOCUMENT ANALYSIS – a. KEYWORDS/DESCRIPTORS

surveillance dosimetry
reactor vessels
radiation damage
H. B. Robinson

b. IDENTIFIERS/OPEN-ENDED TERMS

15. AVAILABILITY STATEMENT

Unlimited

16. SECURITY CLASSIFICATION

(This page) Unclassified

(This report) Unclassified

17. NUMBER OF PAGES

18. PRICE

NUREG/CR-5530

ANALYSIS OF H. B. ROBINSON PWR VESSEL FLUENCE FOR CYCLE 10 UTILIZING PARTIAL LENGTH SHIELD ASSEMBLIES

SEPTEMBER 1990